

AD-A196 875

SECURITY CLASSIFICATION OF THIS PAGE (When Data Entered)

DTIC FILE COPY 1

REPORT DOCUMENTATION PAGE		READ INSTRUCTIONS BEFORE COMPLETING FORM
1. REPORT NUMBER AFIT/CI/NR 88- 37	2. GOVT ACCESSION NO.	3. RECIPIENT'S CATALOG NUMBER
TITLE (and Subtitle) LOW-LEVEL OUTFLOW POTENTIAL OF NON- TORNADIC THUNDERSTORMS INFERRED FROM SINGLE-DOPPLER RADAR		5. TYPE OF REPORT & PERIOD COVERED PHD THESIS
AUTHOR(s) GARY LEON SICKLER		6. PERFORMING ORG. REPORT NUMBER
PERFORMING ORGANIZATION NAME AND ADDRESS AFIT STUDENT AT: TEXAS A & M UNIVERSITY		8. CONTRACT OR GRANT NUMBER(s)
CONTROLLING OFFICE NAME AND ADDRESS		10. PROGRAM ELEMENT, PROJECT, TASK AREA & WORK UNIT NUMBERS
		12. REPORT DATE 1988
		13. NUMBER OF PAGES 143
14. MONITORING AGENCY NAME & ADDRESS (if different from Controlling Office) AFIT/NR Wright-Patterson AFB OH 45433-6583		15. SECURITY CLASS. (of this report) UNCLASSIFIED
		15a. DECLASSIFICATION/DOWNGRADING SCHEDULE
16. DISTRIBUTION STATEMENT (of this Report) DISTRIBUTED UNLIMITED: APPROVED FOR PUBLIC RELEASE		
17. DISTRIBUTION STATEMENT (of the abstract entered in Block 20, if different from Report) SAME AS REPORT		
18. SUPPLEMENTARY NOTES Approved for Public Release: IAW AFR 190-1 LYNN E. WOLAVER Dean for Research and Professional Development Air Force Institute of Technology Wright-Patterson AFB OH 45433-6583 18 July 88		
19. KEY WORDS (Continue on reverse side if necessary and identify by block number)		
20. ABSTRACT (Continue on reverse side if necessary and identify by block number) ATTACHED		

DD FORM 1 JAN 73 1473

EDITION OF 1 NOV 65 IS OBSOLETE

UNCLASSIFIED

SECURITY CLASSIFICATION OF THIS PAGE (When Data Entered)

A-1

LOW-LEVEL OUTFLOW POTENTIAL OF NON-TORNADIC THUNDERSTORMS
INFERRED FROM SINGLE-DOPPLER RADAR

A Dissertation

by

GARY LEON SICKLER

Approved as to style and content by:

George L. Huebner, Jr.
George L. Huebner, Jr.
(Chair of Committee)

Phanindramohan Das
Phanindramohan Das
(Member)

Walter K. Henry
Walter K. Henry
(Member)

P. F. Dahm
Paul F. Dahm
(Member)

Glen N. Williams
Glen N. Williams
(Member)

James R. Scoggins
James R. Scoggins
(Head of Department)

December 1987

ABSTRACT

Low-Level Outflow Potential of Non-Tornadic Thunderstorms
Inferred from Single-Doppler Radar. (December 1987)

Gary Leon Sickler, B.S., Texas A&M University

M.S., Texas A&M University

Chair of Advisory Committee: Dr. George L. Huebner, Jr.

This research examines non-tornadic storms to improve the predictability of low-level storm outflow and to determine whether or not early signatures exist in the structures of the single-Doppler reflectivity and velocity fields that signal the development of a severe downdraft in a non-tornadic storm. By examining the magnitude and changes of radial divergence, flux, shear, and other storm parameters, inferences are made to conclude storm severity and the potential for strong low-level outflow.

Storm parameters are calculated through a series of steps. After initial screening, single-Doppler data are dealiased prior to performing a running average of the velocity field. Then, a search is made along each radial for intervals over which radial divergence is indicated; this is followed by predetermined shear and flux threshold tests. These intervals are used to calculate the storm parameters. Corresponding storm reflectivity fields are observed to identify fluctuations in growth and decay. Qualitative and quantitative

inferences are drawn concerning the structure of the velocity and reflectivity fields and their relationship with low-level storm outflow.

This investigation examines 24 non-tornadic thunderstorms using a case study approach in order to obtain a qualitative view of storm severity. Statistical methods are then employed in the form of multiple linear regression, which indicates that storms can consistently be classified as severe or non-severe. Results indicate that single-Doppler divergence patterns are detectable, that these patterns can be quantified, and the strength of strong, low-level storm outflow can be inferred using this technique.

DEDICATION

To Toni,
--for daring to dream with me--
and
to Lisa and Eric,
for the joy you bring to my life.

ACKNOWLEDGEMENTS

I take great pleasure in recognizing those of you who have helped me complete this research. There are so many who contributed to the successful completion of this research that my acknowledgements will surely exclude someone. I apologize for the omission.

I wish to express my deepest gratitude to my Committee Chairman, Dr. George Huebner. His unselfish support toward the completion of my program and his constant efforts to encourage me were the primary reason this effort was completed.

I am also very pleased to thank Dr. Phanindramohan Das, Professor Walter K. Henry, Dr. Paul F. Dahm, and Dr. Glen N. Williams for serving as members of my committee and helping me with this research.

Further, I owe a thank you to Dr. James R. Scoggins, Head of the Meteorology Department, for his valuable suggestions during the formulation of my adventure.

I acknowledge the very special support and encouragement received from Mr. Ken Wilk, Director of the Next Generation Weather Radar (NEXRAD) Operational Test Facility, and the folks that served on his very capable staff--Tim O'Bannon, Jeff Fornear, Said Hamidi, Mike Istok, Diane Ziegler, and Dave Zittel. I also wish to thank those people at the National Severe Storms Laboratory that helped me along the way.

I also wish to extend a special thank you to Dave Wolff, who provided invaluable and able assistance in the early programming,

volunteered his time during my period of inactivity, and helped me complete details during the last days of this work. Thanks Dave.

Grateful thanks go to those co-workers and friends at Headquarters Air Weather Service--Chuck Melson, Kay Perry, Art Meade, George Rosser, Jeppie Compton, Leslie Brenton, and others, that were interested, and cared enough to encourage me to finish. In particular, I wish to thank my boss, Jack Hayes, who not only supported and encouraged my efforts, but spent his valuable free time reviewing the first draft and helping me organize this effort. Also, these acknowledgements would be incomplete without extending a thank you to Patti, Phyllis, and Judy--very special secretaries--that make work less impossible.

Special recognition is also due Major David Bonewitz for his work in support of our NOAA grant and his contributions to this research.

This work was under the auspices of the Air Force Institute of Technology. This research was funded in part by NOAA Grant NA83AA-D-00060 and supported the NEXRAD program.

TABLE OF CONTENTS

	Page
ABSTRACT	iii
DEDICATION	v
ACKNOWLEDGMENTS	vi
TABLE OF CONTENTS	viii
LIST OF TABLES	xi
LIST OF FIGURES	xii
CHAPTER	
I INTRODUCTION	1
Overview	1
Review of Thunderstorms	3
Single-Cell and Multi-Cell Storms	5
Supercell Storms	6
Non-Tornadic Storms	7
Thunderstorm Downdraft and Outflow	7
Thunderstorm Research Using Doppler Radar	8
Thunderstorm Summit Investigations	10
Statement of Problem	12
II KINEMATIC DOPPLER PATTERNS AND A NON-TORNADIC STORM MODEL	14
Introduction	14
Kinematic Doppler Patterns	15
Pure Rotation	15
Pure Divergence/Convergence	18
Pure Rotation Combined with Divergent/Convergent Flow	18
Inferences	21
Non-Tornadic Storm Model	22
Background	22
Storm Model	23

III	DATA SELECTION AND PROCESSING	25
	Introduction	25
	Data Selection	25
	Single-Doppler Radar Data	25
	NEXRAD IOTF Color Images	26
	Surface and Upper Air Data	26
	Storm Case Selection	27
	Processing	32
	Storm Divergence Algorithm	32
IV	OBSERVABLE FEATURES IN THE STORM	36
	Introduction	36
	Divergence and Flux	37
	Storm Divergence	37
	Radial Divergence	37
	Flux	40
	Divergence Element Testing	41
	Predictive Variables	42
V	METEOROLOGICAL ANALYSIS	44
	Introduction	44
	Cases	45
	Storm 1	45
	Storm 9	60
	Storm 5	78
VI	STATISTICAL ANALYSIS	95
	Introduction	95
	Variables Selected by Statistical Methods	95
	Variables Selected by Meteorological Reasoning	99
	Low-Level Storm Outflow Predictions	101
VII	CONCLUSIONS AND RECOMMENDATIONS	104
	Conclusions	104
	Recommendations	107

REFERENCES	109
APPENDIX A	115
APPENDIX B	117
APPENDIX C	119
APPENDIX D	121
APPENDIX E	123
APPENDIX F	128
APPENDIX G	141
VITA	143

LIST OF TABLES

Table		Page
1	Some strong wind events detected by SAM sites during the IOTF Spring 1983 Demonstration	29
2	Training data set of 14 storms to develop prediction models	30
3	Five storms for prediction and verification	30
4	Five storms to be classified	31
5	Storm divergence algorithm derived predictors of strong low-level outflow from non-tornadic storms	43
6	Storm 1 surface outflow at the 90-series SAM sites	46
7	Storm 9 surface outflow at the 60-series SAM sites	61
8	Storm 9 surface outflow at the 40-series SAM sites	61
9	Models suggested by Maximum R^2 method	97
10	Models suggested by meteorological reasoning	100
11	Maximum R^2 model success	102
12	Meteorological model success	102
13	Low-level storm outflow predictions using different variable models in Tables 11 and 12	103
14	Planned NSSL Doppler radar operational parameters for 1983 Spring NEXRAD IOTF demonstration	120
15	Horizontal threshold variables	122
16	Storm divergence algorithm predictive variable calculations applied to this study to forecast strong low-level outflow from non-tornadic storms	127

LIST OF FIGURES

Figure		Page
1	A Rankin combined velocity profile	16
2	Vortex flow (heavy streamlines) and corresponding single-Doppler velocity signature (thin lines--inbound windflow dashed and outbound windflow solid)	17
3	Divergent flow (heavy streamlines) and corresponding single-Doppler velocity signature (thin lines)	17
4	Single-Doppler velocity pattern (left) and horizontal wind vectors and streamlines (right) for convergent cyclonic flow	19
5	Single-Doppler velocity pattern and horizontal wind vectors and streamlines for convergent anti-cyclonic flow .	19
6	Single-Doppler velocity pattern and horizontal wind vectors and streamlines for divergent cyclonic flow	20
7	Single-Doppler velocity pattern and horizontal wind vectors and streamlines for divergent anti-cyclonic flow	20
8	SAM site locations with respect to NSSL	28
9	Norman Doppler radar contoured reflectivity plot in dBZ units for 20:19:45 CST at 4.7 deg elevation on 27 June 1983	34
10	Storm divergence algorithm divergence pattern elements for same time and elevation as Fig. 9 depicting the areal pattern of radial divergence	34
11	Norman Doppler radar contoured reflectivity field with the derived areal pattern of positive divergence (cross- hatching) for 20:19:45 CST at 4.7 deg elevation on 27 June 1983	35
12	SAM wind speed plot for 90-series complex for Storm 1 (2100 to 2130 CST)	47
13	Storm 1. Norman Doppler radar contoured reflectivity plot for 21:04:40 CST at 0.6 deg elevation on 13 June 1983	48
14	As in Fig. 13, except for 21:14:22 CST at 0.5 deg elevation	49

15	Storm 1. Composite of reflectivity (contours) and positive radial divergence (cross-hatch) for 21:15:20 CST at 1.4 deg elevation	51
16	As in Fig. 15, except for 21:16:17 CST at 2.3 deg elevation	52
17	As in Fig. 15, except for 21:17:15 CST at 3.5 deg elevation	53
18	As in Fig. 15, except for 21:18:12 CST at 4.7 deg elevation	54
19	As in Fig. 15, except for 21:19:10 CST at 6.2 deg elevation	55
20	Distribution of the area enclosed by the 40 dBZ contour during three successive volume scans (V1, V2, and V3) for Storm 1	56
21	Derived area of radial divergence during three successive volume scans (V1, V2, and V3) for Storm 1	56
22	Calculated divergence from the changes in area of divergence shown in Fig. 21	59
23	SAM wind speed plot for 60-series complex for Storm 9 (1950 to 2020 CST)	62
24	SAM wind speed plot for 40-series complex for Storm 9 (2000 to 2030 CST)	63
25	Storm 9. Norman Doppler radar contoured reflectivity plot for 19:45:42 CST at 0.6 deg elevation on 27 June 1983	65
26	As in Fig. 25, except for 19:56:22 CST	66
27	As in Fig. 25, except for 20:06:04 CST	67
28	As in Fig. 25, except for 20:15:46 CST	68
29	Storm 9. Composite of reflectivity (contours) and positive radial divergence (cross-hatching) for 20:01:11 CST at 6.3 deg elevation	69
30	As in Fig. 29, except for 20:02:08 CST at 8.5 deg elevation	70

31	As in Fig. 29, except for 20:10:53 CST at 6.3 deg elevation	71
32	As in Fig. 29, except for 20:11:51 CST at 8.7 deg elevation	72
33	As in Fig. 29, except for 20:20:36 CST at 6.3 deg elevation	73
34	As in Fig. 29, except for 20:21:34 CST at 8.7 deg elevation	74
35	Distribution of the area enclosed by the 40 dBZ contour during four successive volume scans (V1, V2, V3, and V4) for Storm 9	76
36	Derived area of radial divergence during four successive volume scans (V1, V2, V3, and V4) for Storm 9	76
37	Calculated divergence from the changes in the area of divergence shown in Fig. 36	77
38	Storm 5. Composite of reflectivity (contours) and positive radial divergence (cross-hatch) for 19:59:23 CST at 3.5 deg elevation	80
39	As in Fig. 38, except for 20:00:21 CST at 4.7 deg elevation	81
40	As in Fig. 38, except for 20:01:18 CST at 6.3 deg elevation	82
41	As in Fig. 38, except for 20:02:16 CST at 8.7 deg elevation	83
42	As in Fig. 38, except for 20:09:05 CST at 3.5 deg elevation	84
43	As in Fig. 38, except for 20:10:03 CST at 4.7 deg elevation	85
44	As in Fig. 38, except for 20:11:00 CST at 6.3 deg elevation	86
45	As in Fig. 38, except for 20:11:58 CST at 8.7 deg elevation	87
46	As in Fig. 38, except for 20:18:47 CST at 3.5 deg elevation	88

47	As in Fig. 38, except for 20:19:45 CST at 4.7 deg elevation	89
48	As in Fig. 38, except for 20:20:42 CST at 6.2 deg elevation	90
49	As in Fig. 38, except for 20:21:40 CST at 8.5 deg elevation	91
50	Distribution of the area enclosed by the 40 dBZ contour during four successive volume scans (V1, V2, V3, and V4) for Storm 5	92
51	Derived area of radial divergence during four successive volume scans (V1, V2, V3, and V4) for Storm 5	92
52	Calculated divergence from the changes in the area of divergence shown in Fig. 51	94

CHAPTER 1

INTRODUCTION

Overview

The detection and accurate prediction of severe weather phenomena has become an integral role in management and decision making. Each year, severe thunderstorms with associated lightning, high winds, tornadoes, hail, and intense precipitation, interrupt economic and social activities, cause thousands of injuries and deaths, and result in millions of dollars worth of property damage. For several decades, the conventional weather radar has proven to be the most effective tool for the surveillance and identification of severe local thunderstorms. However, this system displays only the distribution of thunderstorm activity. It does not provide information on the fields of motion accompanying these storms. Doppler weather radar has emerged as the primary tool for research concerning the internal kinematics of convective storms.

The potential of the Doppler radar was acknowledged by the National Weather Service, Federal Aviation Administration, and Air Force Air Weather Service with the Tri-Agency development of the Next Generation Weather Radar (NEXRAD) Program. Each NEXRAD unit, a

The citations on the following pages follow the style of the Journal of the Atmospheric Sciences.

single-Doppler weather radar, will generate multi-spectral base data fields of reflectivity, radial velocity, and spectrum width which will provide vast amounts of data for interpretation. These large data sets and the small time scales of convective phenomena mandate the implementation of automated computer techniques to enable analysis of storm severity and potential. The timely processing of these data fields will enable the derivation of many products to warn of severe thunderstorms and related phenomena, enhance flying safety, and evaluate the potential for flash flooding.

Thus far, most research efforts using Doppler data have been concerned with storms that generate tornadic activity. Many non-tornadic severe weather events occur and are overlooked due to the attention given the more spectacular storms, which have been easiest to detect, interpret, and report. Not until recently have investigators begun to turn their attention to non-tornadic storms (Doswell et al., 1983; Zrnice, 1985; Bonewitz, 1986).

The purpose of this research is to focus on non-tornadic storms and, specifically, the potential of using Doppler radar to warn of strong straight-line surface winds. Doppler weather radar provides the ability to probe inside the storm to observe, interpret, and analyze wind flow. Armed with basic understanding of thunderstorm dynamics and through the application of automated techniques, a reliable method to detect strong outflow from non-tornadic storms using single-Doppler radar is possible.

Review of Thunderstorms

Predicting and pinpointing the location of convective processes leading to severe thunderstorm activity has been a problem that has long defied a solution. Early convective theories such as the bubble theory (Scorer and Ludlum, 1953; Woodard, 1959; Turner, 1964) and the entrainment theory (Stommel, 1947) sought to explain simple convective processes. Prior to 1947, few measurements of the meteorological variables within or near a thunderstorm had been recorded. During the Thunderstorm Project (Byers and Braham, 1949) the first measurements were made that established the basic horizontal and vertical dimensions of these storms. For the first time, previous concepts were supported with measurements of the distribution of updrafts, downdrafts, temperature, and precipitation (Ludlum, 1963).

In general, thunderstorms range in diameter from 5 to 50 km and have lifetimes of 30 minutes to 3 hours. Thunderstorms and associated surface weather conditions evolve through three distinct stages: cumulus, mature, and dissipating. The cumulus stage is one in which all air in the cell is flowing upward due to converging warm moist air at the surface. This continues until precipitation begins. During the mature stage, the warm updraft and cold downdraft exist side by side with precipitation reaching the ground. The falling precipitation and the entrainment of mid-level air into the storm combine to form the storm downrush which strikes the ground and spreads out as a micro-cold front. This is the zone of sharp temperature contrast and strong

winds at the leading edge of the cold downdraft. The dissipating stage is characterized by weakening cold downdrafts throughout the storm. The surface precipitation rate diminishes, or ceases, and the cold dome of air, created by the storm outflow, subsides as the surface winds decrease. Often, unless associated with frontal passage, the surface conditions will return gradually to prestorm conditions.

Each storm is unique, consequently, the likelihood of identical environmental conditions that create any two storms is highly improbable. For this reason, both modelers and forecasters have been marginally successful in understanding and forecasting these phenomena. While forecasting the location and severity of an individual storm has been only partially successful, the meteorological conditions necessary for convective activity are known. Ordinary*, or non-severe thunderstorms are likely to develop in a potentially unstable atmosphere when adequate low-level moisture and a triggering mechanism are present. The conditions necessary for development of a severe thunderstorm are more complex, but mainly consist of an environment that is convectively unstable with abundant low-level moisture over which a dry air intrusion exists in addition to a triggering mechanism, and strong lower and upper level winds (Miller, 1972).

* Ordinary, or non-severe thunderstorms as used in this paper refers to non-tornadic storms with winds less than 25 m s^{-1} and hail less than 2 cm in diameter.

Single-Cell and Multi-Cell Storms

Single-cell thunderstorms are usually 5-10 km in diameter, live less than 1 hour, and change with time evolving through the three stages of a storm. The early growth stage has updrafts of 15 m s^{-1} which last about 10 minutes until reaching the mature stage. Once the updraft is destroyed, presumably due to the falling precipitation from upper levels, dissipation begins. Because of light ambient winds with little vertical shear, single-cell storms tend to retain their horizontal and vertical symmetry throughout their lifetime (Chisholm and Renick, 1972).

Multi-cell storms consist of evolving cells which may go through a life cycle similar to the single-cell storm. Even though Byers and Braham (1949) first noted multi-cellular structure in storms, structural and mechanical details of their evolution continue to be unraveled decades later (Browning and Foote, 1976; Wilk et al., 1978). As weather radar observations became available the structural distribution of thunderstorms became more evident. The horizontal extent of a multi-cell storm is usually 30-50 km, often extending vertically a few km into the stratosphere. New cells generate every 5-10 minutes in preferred locations on the right or right rear storm flank, with two to four cells occurring simultaneously during the life of the storm. The cells rise at speeds of $10\text{-}15 \text{ m s}^{-1}$, are 5-10 km in diameter, and have lifetimes of 30-45 min (Atkinson, 1981). A typical multi-cell storm has 30 or more cells developing and dissipating during its life cycle.

Supercell Storms

The supercell, a term first used by Browning (1962), is a quasi-steady state single cell, characterized by sustained $25\text{--}50\text{ m s}^{-1}$ updrafts coexisting with sustained downdrafts for relatively long periods. They are 20-50 km in diameter, extend several km into the stratosphere to heights sometimes exceeding 20 km, and have lifetimes of 1-6 hours or more. These storms exist in a strongly sheared environment in which the wind generally veers with height (Marwitz, 1972). The reinforcing effect of the updraft-downdraft configuration, allows the updraft to rid itself of water (which would tend to destroy the updraft and hence the storm) through precipitation into the downdraft. This intensifies the downdraft and maintains a strong convergence zone to feed the storm at or just above the gust front. These storms have been found to be consistent tornado producers. Nelson (1976) found that 6 of 10 Oklahoma supercells produced a tornado. Fankhauser (1971), using aircraft measurements made at low- and mid-levels, graphically synthesized a three-dimensional representation of a supercell. His model has a cyclonically rotating updraft which is surrounded by a cyclonically rotating downdraft, both are tilted upshear in an environment where the winds are veering with height. The Lemon and Doswell (1979) model of a supercell incorporates two downdrafts, a rear flanking downdraft and a forward flanking downdraft. The two-downdraft model is supported by a number of other investigators (Charba and Sasaki, 1971; Nelson, 1977; Barnes, 1978; Heymsfield, 1978; Schlesinger, 1978; Klemp et al., 1981).

Non-Tornadic Storms

The non-tornadic storm is usually an ordinary, single-cell thunderstorm that has the capability to grow adequately to generate a storm downdraft capable of producing surface winds equal to or greater than 25 m s^{-1} . The non-tornadic storm is not associated with mesocyclonic phenomena, often a precursor to tornadic activity. The non-tornadic thunderstorm is usually 5-10 km in diameter, but can approach 15 km or slightly larger dimensions. The early growth stage goes through a life cycle about the same as a single-cell storm, lasting approximately 60-90 minutes, with vertical development of the storm rarely exceeding 12-14 km.

Thunderstorm Downdraft and Outflow

Early studies by Byers and Braham (1949) found the thunderstorm downdraft to be accelerated by falling precipitation, colder than the clear air environment, with the strongest outflow in the direction of storm movement. Furthermore, they proposed that dry mid-tropospheric air enters the rear of the storm, entrains small water droplets, and due to negative buoyancy, accelerates the downdraft. This observation was confirmed by Fankhauser (1971). Additional contributions to the problem of thunderstorm downdraft were made by Lemon (1974) and Goff (1975) who discovered multiple cold air surges within storm outflow. Accompanying the strong cold outflow, great horizontal and vertical shears were found in the lower 500 m of Oklahoma thunderstorms (Goff, 1975). Charba (1972) investigated the mechanics of motion of the gust

front and concluded that the propagational speed of the gust front increases as the storm outflow increases. Goff (1976) observed, just as Byers and Braham had earlier, that the speed of the outflow, which develops into the gust front, is indicative of the storm's maturity. Goff found, as had Auer et al. (1969), that the gust front extended an average of 5 km ahead of the leading edge of the surface precipitation. With the advent of Doppler weather radar, researchers began to use the new tool to strengthen and confirm hypotheses on thunderstorm downdraft and outflow.

Thunderstorm Research Using Doppler Radar

Advances of radar meteorology and the pioneering efforts made concerning Doppler radar are available in reviews by Atlas (1964) and Lhermitte (1966). The early promise of Doppler radar in severe storm analysis was reported by Lhermitte and Atlas (1961), Lhermitte (1964), and Donaldson et al. (1969). The mid-1970's saw numerous Doppler radar experiments with detailed four-dimensional flow fields of thunderstorms, confirming hypothesized intrastorm kinematics and breaking new ground concerning the evolution and structure of severe supercell thunderstorms (Brandes, 1977; Kropfli and Miller, 1976). Research clearly demonstrated the possibility of real-time applications of Doppler radar observations during the Joint Doppler Operational Project (JDOP). The JDOP provided the impetus for the NEXRAD Program by demonstrating that Doppler radar surveillance techniques improve the

accuracy and timeliness of severe storm warnings (JDOP Staff, 1979). However, due to the vast amounts of data generated, it became obvious to experienced investigators that only through extensive automated computer techniques would the full potential of a nation-wide Doppler weather radar network be realized.

The National Severe Storms Laboratory (NSSL), the site of the JDOP experiment, has been a major contributor in the field of Doppler radar research on thunderstorms. In 1981, the NEXRAD Interim Operational Test Facility (IOTF) was established at NSSL. Studies by NSSL, the IOTF, the Air Force Geophysics Laboratory, and others have developed fundamental automated techniques needed in the NEXRAD system, particularly, to examine gust fronts and associated low level wind shear.

Attention was given first to single-Doppler radar detection of straight-line cold air outflow from non-tornadic storms by Bonewitz (1978). Other gust front studies using single-Doppler data have been completed by Fujita (1981), Wakimoto (1981), Zrnic and Lee (1983), Klinge (1985), and Uyeda and Zrnic (1986). Koscielny et al. (1982) used single-Doppler radar to map boundary-layer convergence in a prestorm environment. These preliminary investigations demonstrate the superior potential of single-Doppler displays over conventional radar surveillance techniques. The JAWS (Joint Airport Weather Studies) Project (JAWS Staff, 1984) enthusiastically supported the use of Doppler data in the detection of strong storm outflow, specifically the microburst. Using JAWS data, Roberts and Wilson (1984) showed that

convergent flow aloft, coupled with a descending precipitation shaft, is a good indicator of a microburst situation. A signature of this kind on a Doppler display would alert an operational forecaster to the possible downdraft initiation and the potential hazard of a microburst. Consequently, the relationship between the storm top and lower levels of the storm should be examined carefully to gain insights concerning storm growth and its potential to cause intense weather at the surface.

Thunderstorm Summit Investigations

Visual and infrared satellite imagery have clearly depicted thunderstorm anvil expansion rates and the variation of thunderstorm cloud-top temperatures. Severe thunderstorms often show a V-shaped area in the cloud tops. This enhanced-V appears to be due to colder (and higher) clouds surrounding an area of warmer (and generally lower) cloud-top temperatures (McCann, 1983). Studies of cloud-top temperature variations during thunderstorm evolution indicate rapid expansion of cold cloud areas and a decrease of cloud top temperatures in the vicinity of dramatic rainfall events (Sickler, 1979; Sickler and Thompson, 1980) and severe weather events, that is, they are storms that generate large hail, strong surface winds, and tornadic activity (Adler and Fenn, 1979). Further, comparisons of upper level dual-Doppler radar derived velocity fields and coincident satellite imagery indicate a direct relationship between upper level divergence and anvil area growth rates (Mack and Wylie, 1982; Heymsfield, et al.,

1983). While satellite imagery depicts gross modifications of widespread thunderstorm top variations, Doppler radar can directly measure high-resolution internal storm parameters at all levels within a storm in a temporally and spatially relevant fashion. Because convergence in, and just below, the storm summit* signals the possibility of downdrafts, the changes of magnitude of divergence at these levels are thought of as precursors to potential change in storm severity. Lemon and Burgess (1980) conducted single-Doppler investigations of storm-summit outflow. Their findings suggest both severe and non-severe storms be examined to develop NEXRAD threshold divergence signatures that signal the potential for severe weather. These same studies of storm top outflow have been simulated in storm top divergence fields by Wood and Brown (1983, 1986) to illustrate a typical tornadic storm top signature. Accordingly, explorations using storm summit divergence to identify potentially severe storms using single-Doppler radar were continued. Witt and Nelson (1984) used single-Doppler data to study the relationship between the strength of the storm top divergent outflow and hailstorm intensity. While these findings were based on a small sample, they proved to be a reliable predictor for maximum hail size and provided some insight as to the possible damage swath. Zrnic and Gal-Chen (1984) developed an

* Storm summit as used in this paper refers to the highest elevation angle of a volume scan that is able to sample most of the upper-levels of a non-tornadic storm with a single-Doppler weather radar. Consistent with normal radar sampling of the atmosphere, the radar beam propagates along an incline, as it samples the storm, which may miss a small part of the upper-levels of the storm (Appendix F notes this limitation).

algorithm that yielded promising results for automatic divergence recognition and quantification. The algorithm is similar to the mesocyclone algorithm developed by Zrnic et al. (1983) which integrates earlier concepts (Hennington and Burgess, 1981; Zrnic et al., 1982). It enables divergence inferences of the data to process multi-spectral fields into patterns of storm divergence and flux.

Statement of Problem

The divergence algorithm, as it was initially developed, requires additional work prior to operational implementation (Zrnic, 1985). However, adequate validity was demonstrated and the NEXRAD Joint Systems Program Office (JSP0) included it in their algorithm report (NEXRAD JSP0 Staff, 1985). Building on Zrnic's work, Eyster (1985) refined the original algorithm to streamline the methodology and examine the relationship between the vertical structure and magnitude of radial divergence to tornadic activity. His results demonstrate recognition of tornadic phenomena from supercells.

Although this algorithm was conceived for use on supercell storms capable of generating tornadic activity, Sickler et al. (1985b) modified it for use on non-tornadic storms to enable recognition of characteristic divergence patterns and to separate severe, potentially severe, and non-severe storms. The objective of this investigation is to relate the changes of non-tornadic thunderstorm tops to low-level storm outflow and to develop techniques to determine when a

non-tornadic thunderstorm will produce a severe downdraft. It is hypothesized that early signatures exist in the structures of the upper level single-Doppler reflectivity and velocity fields that indicate the development of a severe downdraft in non-tornadic storms. It is believed that subtle differences exist in the upper-levels of a non-tornadic thunderstorm that are important in classifying storm intensity. This hypothesis will be evaluated using a case study approach and statistical methods employing multiple linear regression modeling techniques. It is hoped this research will provide the basis for a reliable single-Doppler radar method of determining the potential and intensity of low-level storm outflow from non-tornadic thunderstorms.

CHAPTER II

KINEMATIC DOPPLER PATTERNS AND A NON-TORNADIC STORM MODEL

Introduction

The single-Doppler radar is limited to measuring the component of the wind in a radial direction from the radar. Therefore, precise measurements of the true wind motions within a storm are not possible. However, just as the conventional radar is used to note severe weather signatures (i.e., bounded weak-echo region, line-echo-wave pattern, hook echo, etc.) from the structures in a reflectivity field, certain Doppler velocity patterns indicate specific internal storm kinematics that enable recognition of a variety of weather features of great significance to operational forecasters. Studies by Donaldson (1967), Burgess (1976), Lemon (1977), Lemon et al. (1977), and others have pointed out the importance of recognition of severe storm signatures and the value of Doppler radar to issue timely weather warnings.

This chapter will review single-Doppler velocity patterns reflecting characteristics of pure rotation and divergence and conclude with a non-tornadic storm model. By familiarization with the single-Doppler velocity pattern characteristics, insights can be gained concerning their application to real-time severe weather situations. Some basic principles of Doppler weather radar are summarized in Appendix B. Readers unfamiliar with Doppler radar may find the background information in that Appendix helpful.

Kinematic Doppler Patterns

Pure Rotation

Using the basic model of a Rankine combined vortex (Donaldson, 1970), Burgess (1976) noted mesocyclone signatures. The Rankine combined velocity profile (Fig. 1) consists of two distinct velocity distributions. The velocity of the inner portion ($r < R_c$) of the profile increases linearly with distance from the center, while the velocity change on the outer portion is inversely proportional to the distance from the center. This pure flow model provides a theoretical basis for recognition and study of mesocyclone patterns using single-Doppler radar.

An idealized horizontal scan across a vortex (heavy concentric lines) rotating about a vertical axis is depicted at Fig. 2. A Doppler radar, detecting such phenomena from the south of the vortex center would produce the single-Doppler velocity pattern depicted by the thinner lines. Because Doppler radar can detect only the component of flow along the beam, the dashed thin line represents the inbound velocities and the solid thin line represents the outbound velocities. The boldly dashed line across the center of the figure is the region where the velocity goes undetected (i.e., zero) because the flow is perpendicular to the beam.

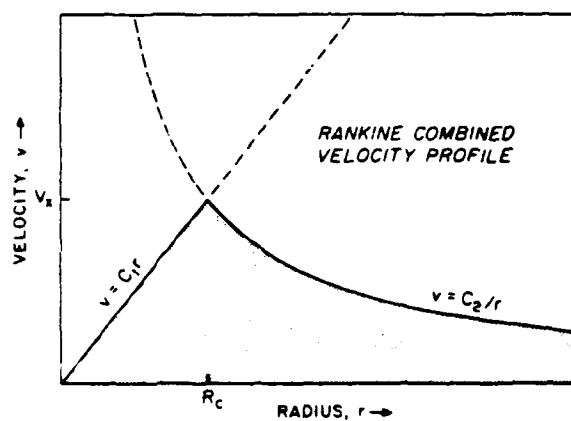


Fig. 1. A Rankine combined velocity profile. Maximum velocity (V_x) occurs at core radius (R_c) (After Wood and Brown, 1983).

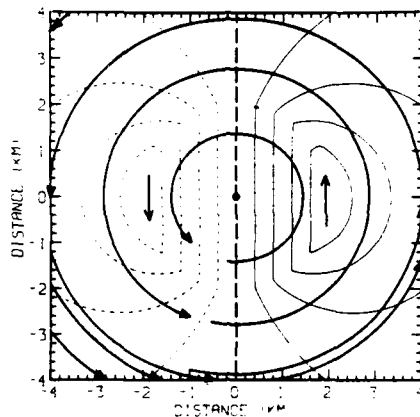


Fig. 2. Vortex flow (heavy streamlines) and corresponding single-Doppler velocity signature (thin lines--inbound windflow dashed and outbound windflow solid). Radar location is considered due south of flow field (After Wood and Brown, 1983).

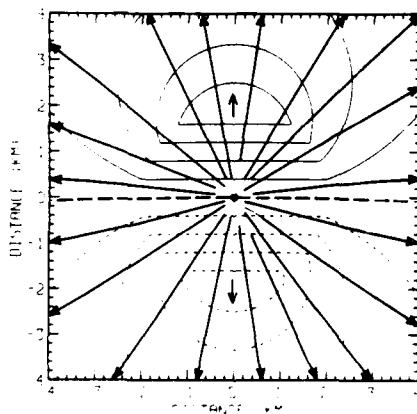


Fig. 3. Divergent flow (heavy streamlines) and corresponding single-Doppler velocity signature (thin lines). Radar location is as in Fig. 2 (After Wood and Brown, 1983).

Pure Divergence/Convergence

In contrast to Fig. 2, which illustrates pure rotation, and approximates a mesocyclone signature, Fig. 3 depicts a pure divergence signature and the idealized single-Doppler velocity return. Notice that the single-Doppler pure divergence pattern is the same as the pure rotation pattern where the couplet of velocity is rotated counterclockwise 90 deg. In this case the zero line (bold dashed line horizontally across the center of the figure) is oriented east to west (right to left across figure) since the radar cannot view the flow perpendicular to the beam axis. The flow is the greatest at the center where it is parallel to the beam axis. Similarly, the thin dashed lines represent inbound flow, while the thin solid lines represent outbound flow. The idealized single-Doppler velocity signature, or couplet of velocity, for convergence (not pictured) is the opposite to Fig. 3, with the inbound flow occurring at the top of the figure and the outbound at the bottom.

Pure Rotation Combined with Divergent/Convergent Flow

Combinations of convergent cyclonic flow, convergent anti-cyclonic flow, divergent cyclonic flow, and divergent anti-cyclonic flow are shown at Figs. 4-7. As in the cases of pure rotation and pure divergence, none of these flow combinations are likely to occur in pure form in nature. However, accurate interpretations of patterns caused by rotating convergent or divergent flow will allow correct inference of a storm's potential severity. When Figs. 4-7 are compared with the single-Doppler velocity patterns in Fig. 2 (pure rotation), the zero

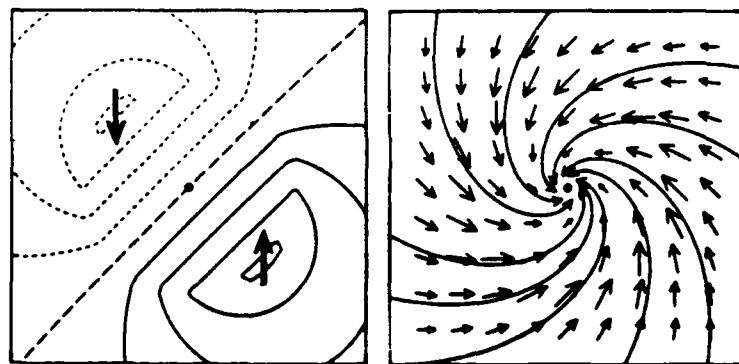


Fig. 4. Single-Doppler velocity pattern (left) and horizontal wind vectors and streamlines (right) for convergent cyclonic flow. Radar location is as in Fig. 2 (After Wood and Brown, 1983).

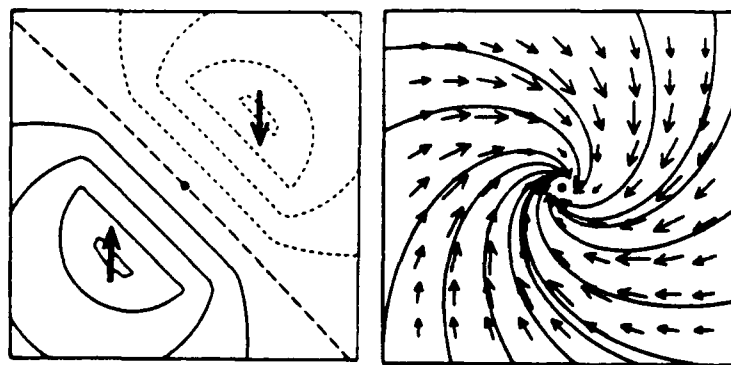


Fig. 5. Single-Doppler velocity pattern and horizontal wind vectors and streamlines for convergent anti-cyclonic flow. Radar location is as in Fig. 2 (After Wood and Brown, 1983).

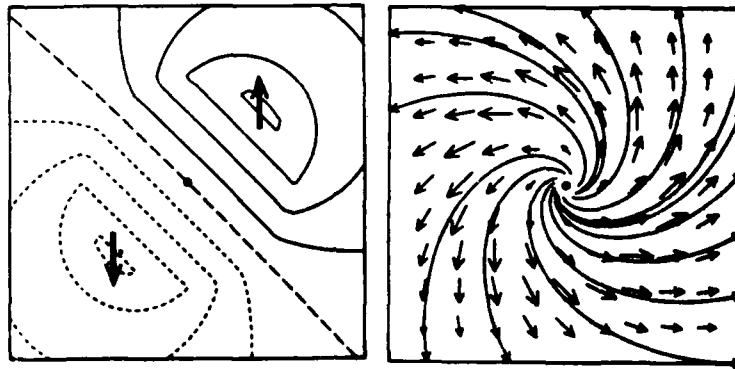


Fig. 6. Single-Doppler velocity pattern and horizontal wind vectors and streamlines for divergent cyclonic flow. Radar location is as in Fig. 2 (After Wood and Brown, 1983).

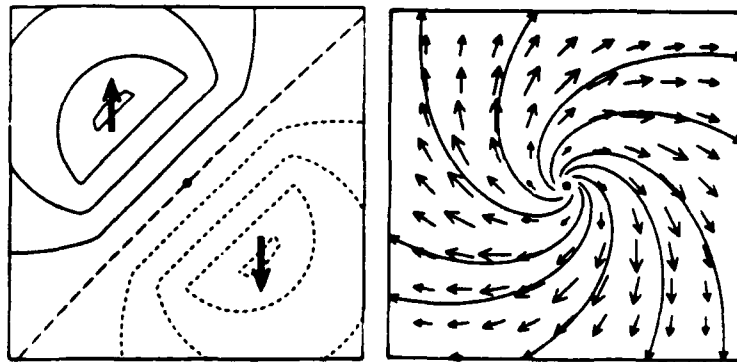


Fig. 7. Single-Doppler velocity pattern and horizontal wind vectors and streamlines for divergent anti-cyclonic flow. Radar location is as in Fig. 2 (After Wood and Brown, 1983).

line is observed to be reoriented in each figure in response to changes in the inbound/outbound flow. In the convergent cyclonic flow pattern (Fig. 4), the zero line is rotated 45 degrees clockwise from the pure rotation mesocyclone case (Fig. 2); whereas, in the convergent anti-cyclonic flow pattern (Fig. 5), the zero line is rotated 135 degrees clockwise with respect to Fig. 2. Similarly, divergent cyclonic flow (Fig. 6) is rotated 45 degrees counterclockwise with respect to the pure rotation case (Fig. 2) and 45 degrees clockwise with respect to divergent flow (Fig. 3). Finally, divergent anti-cyclonic flow (Fig. 7) is rotated 45 degrees counterclockwise to divergent flow (Fig. 3).

Inferences

This discussion indicates that seven basic thunderstorm flow patterns can be inferred from single-Doppler velocity fields. They are: mesocyclone (rotation), divergent flow, convergent flow, convergent cyclonic flow, convergent anti-cyclonic flow, divergent cyclonic flow, and divergent anti-cyclonic flow. An understanding of the single-Doppler signatures of these basic flow patterns will enable quicker recognition of these patterns detectable in nature and may allow positive identification of potentially significant events. These basic forms are used in this research in the data analysis and in the non-tornadic storm model (discussed in the next subsection).

Non-Tornadic Storm Model

In this investigation, a non-tornadic severe storm is defined as a thunderstorm that has the potential to create a storm downdraft capable of producing surface winds equal to, or greater than, 25 m s^{-1} , but does not produce a mesocyclone (often a precursor to tornadic activity). Many studies of single-cell, multi-cell, and supercell storms have used various forms of data analysis and processing (i.e., conventional radar, single- and dual-Doppler radar, surface mesonet measurements, and numerical simulations), in combination or individually, to study the behavior of convective storms, especially internal storm kinematics. This portion of the investigation provides a background and presents the basic non-tornadic storm model considered throughout this study.

Background

The proposed non-tornadic storm model used in this research is a composite model based primarily on supercell models modified for the non-tornadic storm and refined using results of an analysis of over 30 storms. The supercell structure was used because most thunderstorm studies have supercells as their focus (Doswell et al., 1983). Those authors noted earlier (Chapter I, Supercell Storms) describe atmospheric conditions, present detailed analyses of storm development and decay, and propose numerical models that explain the internal storm motions and their evolution. Consequently, basic inferences with

respect to accepted models of a supercell are integrated logically into this model. Likewise, models developed from single- and multi-cell storms were considered, but to a lesser degree.

Storm Model

The non-tornadic storm model proposed by the author in this paper is fed by converging boundary-layer, warm, moist updraft that sustains the growth and longevity of the storm. The updraft is normally slightly tilted, where the amount of tilt depends on the strength of the environmental wind (speed shear) and the degree to which it is veering with height (directional shear). Consistent with basic storm morphology, water vapor rises via the updraft, condenses into water droplets that concentrate in preferred central locations within the storm, and eventually fall as precipitation. Some of this precipitation ultimately falls into a downdraft zone created by entrainment processes due to mid-level dry air entering the rear of the storm. The falling precipitation, that is cooled further by partial evaporation as it enters the cool, dry, downdraft zone, serves to reinforce and accelerate the downdraft. This storm outflow strikes the ground and spreads out as the gust front, which, in turn, tends to reinforce the updraft. The process continues until the falling precipitation dampens the updraft, destroying the energy source, and ultimately causes the storm to dissipate. The updraft-downdraft rotation will normally be cyclonic because, in northern mid-latitudes, the environmental winds veer with height. This generally causes the

storm to move to the right of the mean mid-level wind flow. The upper levels, or storm summit, will be mostly divergent as long as the storm is growing prior to the transition into the heavy precipitation stage.

It was observed in this study that many of the storms pulsate. That is, strong divergence is followed by weaker divergence, or even convergence, followed by stronger divergence. This was observed to occur until the heavy precipitation stage occurred--generally after the storm grows to its greatest potential and begins to collapse with the maximum flux of liquid water downward. These are the key aspects of this model which are important to this research. First, contractions of the storm summit divergence field (i.e., convergence) signal the initiation of the transfer of energy downward. Second, strong contractions in the divergence and areal reflectivity fields indicate potentially strong outflow. These are the two storm-summit signatures used in this investigation.

CHAPTER III

DATA SELECTION AND PROCESSING

Introduction

This investigation employs primarily single-Doppler radar data. Supplemental data sets incorporated into this investigation were color images of Doppler fields, surface-automated-mesonet (SAM) data, conventional surface observations, and upper-air data. Most of the storms evaluated were recorded during the NEXRAD Interim Operational Test Facility (IOTF) spring 1983 demonstration from 4 April to 13 May 1983 and from 13 June to 6 July 1983. A daily meteorological summary of the data collected during the demonstration period was prepared by the IOTF (Ziegler, 1984).

This chapter notes the data selection procedure, how the data were processed, and provides a review of the algorithm used to calculate storm parameters.

Data Selection

Single-Doppler Radar Data

The single-Doppler radar data in this study were recorded by NSSL located in Norman, Oklahoma. The operational characteristics of the NSSL Doppler radar during the periods of data collection are given in

Appendix C. The data were recorded in a continuous, clockwise sweep with pre-set elevation angles. The mean radial velocity and spectrum width estimates which were detected and recorded by the radar system are scaled to units of m s^{-1} , while the Probert-Jones form of the radar equation (Doviak and Sirmans, 1973) is used to calculate equivalent reflectivity. The data were converted into universal tape format (UTF) by the NEXRAD IOTF according to Barnes (1980). Initially, the Doppler data in UTF were catalogued by storm day and incorporated into the Texas A&M University computer tape library. The data were unpacked, edited, and put on disks using a computer program developed by Bonewitz (1984).

NEXRAD IOTF Color Images

Chromatic computer displays were reviewed and hard-copy color prints of single-Doppler fields (i.e., reflectivity, mean radial velocity, and spectrum width) were produced for storm periods of interest. The color images were used to test the validity of the FORTRAN programs to ensure they were handling the Doppler fields correctly, and to enable qualitative and quantitative insights as to the relationships between the three Doppler fields (Sickler et al., 1985a, 1985b).

Surface and Upper Air Data

The surface data were composed of IOTF SAM site data and conventional surface observations. The SAM data were used to determine

the outflow strength of storms passing over or near the sites (see Fig. 8 for locations) and provide surface verification for this research. Each SAM site records a one-minute update of various meteorological parameters. These consist of the average and minimum pressure, rainfall, average u and v wind components, peak one-minute wind speed, and the dry- and wet-bulb temperature. The SAM data format can be reviewed in Bonewitz (1986). The upper-air data included 850, 700, 500, 300 mb National Weather Service analyses as well as rawinsonde data. These were used to determine the environmental wind, flow, and storm motion.

Storm Case Selection

The storm cases were selected after considering several factors. First, cases had to be isolated for which both Doppler and coincident SAM data existed. After reviewing the meteorological parameters recorded at the SAM sites, severe and non-severe outflow cases that met the established criteria (i.e., strong surface winds in excess of 18 ms^{-1}) were tabulated to see if single-Doppler data for similar periods existed. An example of some of the strong winds recorded at the SAM sites are shown in Table 1. Therefore, depending on the condition of the NSSL radar and support equipment, periods of reliable single-Doppler data were selected.

Second, these data periods were reviewed using IOTF resources and methods developed by Istok (1983) to determine the precise periods of single-Doppler data for this study. The final step, after examination

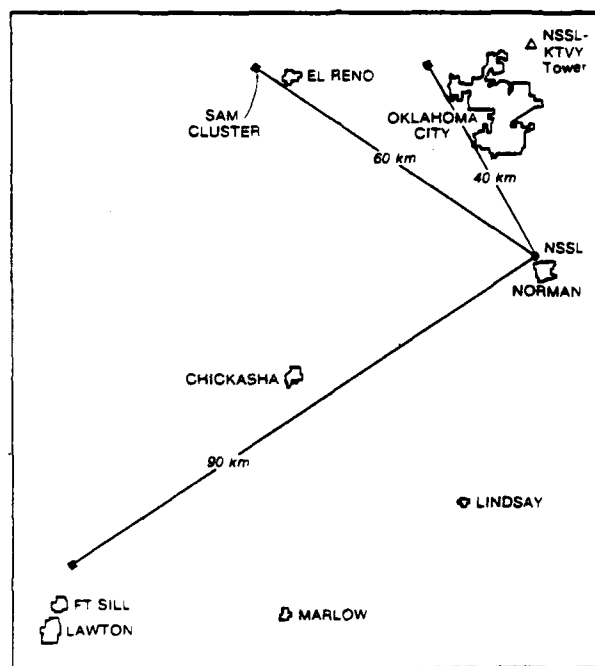


Fig. 8. SAM site locations with respect to NSSL (After Bonewitz, 1986).

Table 1. Some strong wind events detected by SAM sites during the IOTF Spring 1983 Demonstration (time is CST and peak wind speed is in m s^{-1}).

Date	Time	SAM Cluster	Peak Speed	Direction
22 April 83	1922-1943	Fort Reno	26	NE
22 April 83	1944-1954	Wiley Post	19	NE
22 April 83	2011-2023	Fort Sill	26	NW
13 June 83	2120-2121	Fort Sill	27	NW
26 June 83	1736-1740	Fort Sill	25	SE
27 June 83	1853-1902	Fort Sill	36	SW
27 June 83	1956-2007	Fort Reno	32	SW
27 June 83	2015-2017	Wiley Post	26	SW
28 June 83	0001-0002	Wiley Post	24	NW
28 June 83	0011-0018	Fort Sill	25	NW

of the storm days, was to select a number of severe and non-severe storms. In this study a severe non-tornadic storm was defined as one with winds equal to or greater than 25 m s^{-1} . Well over 30 storms met criteria for surface outflow in excess of 18 m s^{-1} ; however, some storms were too embedded within a line of storms to ensure adequate isolation to examine storm summits. Only 19 storms were usable. Of these, 14 storms were selected to provide a training data set (Table 2), and 5 storms were held back for prediction and verification (Table 3). Five additional storms without surface verification were

Table 2. Training data set of 14 storms to develop prediction models (outflow in m s^{-1}).

SEVERE			NON-SEVERE		
STORM	DATE	OUTFLOW	STORM	DATE	OUTFLOW
1	13 JUNE	27	12	28 JUNE	20
2	13 JUNE	28	13	28 JUNE	21
3	27 JUNE	36	15	28 JUNE	21
4	27 JUNE	28	16	28 JUNE	18
9	27 JUNE	32	17	22 APRIL	24
21	13 MAY	29	18	22 APRIL	19
23	13 MAY	27	20	22 APRIL	20

Table 3. Five storms for prediction and verification (outflow in m s^{-1}).

SEVERE			NON-SEVERE		
STORM	DATE	OUTFLOW	STORM	DATE	OUTFLOW
7	27 JUNE	26	10	27 JUNE	23
22	13 MAY	31	14	28 JUNE	19
24	27 JUNE	36			

selected for classification (Table 4). Most of these storms occurred at ranges of 50 to 90 km from the southwest-to-north of NSSL. Ultimately, storms for this investigation were from archived IOTF data collected on 22 April, 13 May, 13 June, 27 June, and 28 June 1983. Storms for 13 April 1981 and 26 April 1984 were also examined, but not used.

Table 4. Five storms to be classified.

STORM	DATE
5	27 JUNE
6	27 JUNE
8	27 JUNE
11	27 JUNE
19	22 APRIL

Processing

A set of computer programs was needed to perform the qualitative and quantitative analyses. Much of the initial programming needed to manipulate the Doppler fields and other data obtained from the IOTF and NSSL was done by Bonewitz (1984, 1986). A comprehensive description of the tape to disk transfer and many of the plotting programs are in Bonewitz (1986). However, a storm divergence algorithm had to be developed by Sickler et al. (1985b) to interrogate storm cases after the NSSL Doppler data were transferred to the Texas A&M University's Amdahl computer disks. For each storm, variables were calculated for all available elevation scans. The calculation procedure is described in Appendix E, while the details of the algorithm can be reviewed in Appendix F.

Storm Divergence Algorithm

The mean radial velocity fields were screened using a reflectivity threshold technique to suppress undesirable or insignificant data. After this, the mean radial velocities were dealiased prior to performing a running average of the velocity field so that the effective range resolution was 1 km; this latter step was needed to approximate the mid-range (60 km) azimuthal resolution. A search was then made along each radial for an objective determination of the range interval over which radial velocities increased and fell within the

predetermined shear and flux thresholds. These positive divergence elements were then saved in order to later form areal patterns and calculate the single-Doppler variables for later examination to determine their relative importance for use in a multiple regression model. Figs. 9 and 10 show the reflectivity field and the storm areal pattern of positive divergence. A composite of the two fields is at Fig. 11.

All corrections for azimuth, elevation angle, and range, as well as other necessary radar calibrations are applied to the data according to Bonewitz (1984), where data processing is selectable for specified azimuth and elevation angles and discrete ranges. Values of reflectivity and velocity were determined along each radial and pulse volume. Velocities located in areas where signal-to-noise ratio was less than 0.0 dB or reflectivity was less than 10 dBZ were deleted to eliminate the unreliable velocities.

The storm divergence algorithm output for each elevation angle within each volume scan for approximately each 10 minute time interval was examined for each storm. In all, over 90 volume scans containing 25 individual variables were tabulated for the storms in this investigation. Appendix E, Table 16 contains the storm parameters used in this study to forecast strong low-level outflow from non-tornadic thunderstorms.

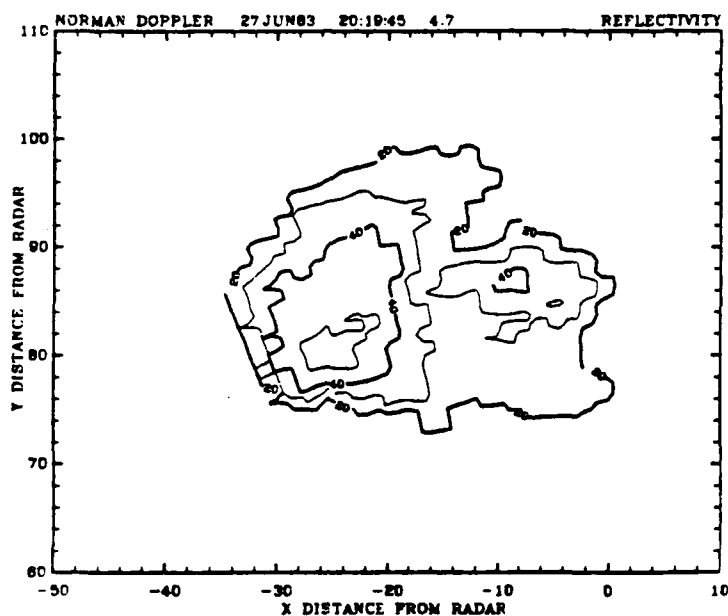


Fig. 9. Norman Doppler radar contoured reflectivity plot in dBZ units for 20:19:45 CST at 4.7 deg elevation on 27 June 1983. Distances from the radar are in km, while reflectivity is contoured in dBZ.

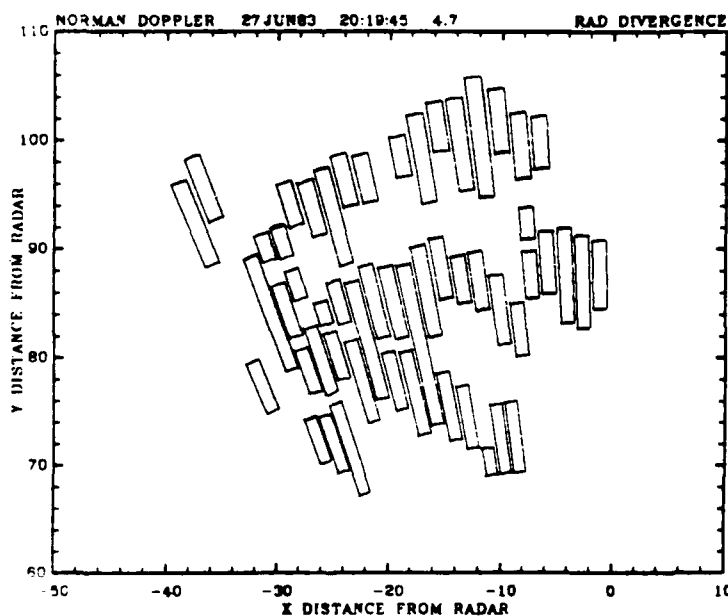


Fig. 10. Storm divergence algorithm divergence pattern elements for same time and elevation as Fig. 9. depicting the areal pattern of radial divergence. Only positive divergence is patterned.

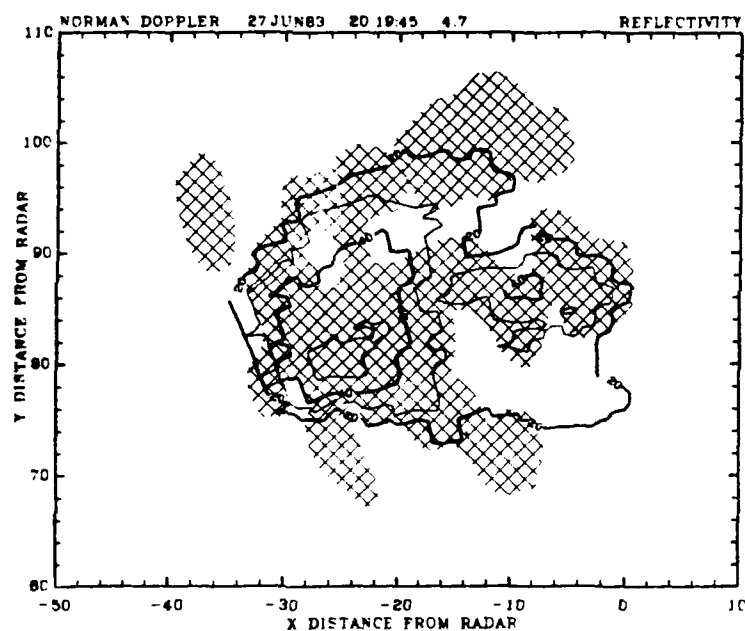


Fig. 11. Norman Doppler radar contoured reflectivity field with the derived areal pattern of positive divergence (cross-hatching) for 20:19:45 CST at 4.7 deg elevation on 27 June 1983. Distances from the radar are in km, while reflectivity is contoured in dBZ.

Divergence and Flux

Storm Divergence

Consider a symmetric thunderstorm with pure divergence flow as depicted in Fig. 3. For a radar sampling the horizontal cross-section of a symmetric thunderstorm, the areal changes at one level over time allows estimations of horizontal divergence. While, the divergence is estimated as horizontal in this investigation, and routinely in other Doppler investigations, the radar beam samples the storm along a slant plane rather than an absolute horizontal plane (except at zero elevation).

Horizontal divergence can be approximated by

$$\text{Div}_2 \approx \frac{1}{A} \frac{\Delta A}{\Delta t} , \quad (4.1)$$

where A is areal extent at times t_1 and t_2 . In this study, the divergence of the areal patterns of radial divergence is estimated by

$$\text{Div}_2 \approx \frac{1}{A(t_1)} \cdot \frac{A(t_2) - A(t_1)}{t_2 - t_1} . \quad (4.2)$$

Radial Divergence

By convention, Doppler radar radial velocities toward the radar are negative and those away from the radar are positive. Symmetric

divergence (Fig. 3) would have a radial velocity pattern with negative (inbound) velocities closest to the radar and equal magnitude, but positive (outbound) velocities further away from the radar. If storm motion is not taken into account, negative or positive velocities may not be observed. For example, if the storm is moving away from the radar (outbound), the radial velocities detected closest to the radar may be positive, but quite small. This occurs because all the velocities are shifted by an amount proportional to the storm motion. However, divergence within the storm will always be indicated by increasing velocities along the radar radial, regardless of the storm motion.

Noteworthy, is that radial divergence, as used in this paper, is along a radar radial and is considered radial stretching by other investigators. That is, it is the rate of stretching of a radial line element. As viewed in this study, the areal pattern formed by the radial divergence elements actually form an area that represents the divergence pattern at that level of the storm. If the storm was symmetric, the divergence would be pure, and the exact divergence pattern would likely be observed. Consequently, this paper uses the term "radial divergence" where others may prefer the term "radial stretching."

Since Doppler radar measures only the radial velocity component, it is only possible to measure the radial component of divergence. Zrnic and Gal Chen (1984) use spherical coordinates to present this component

as

$$\text{Div}_r = \frac{2v}{r} + \frac{\partial v}{\partial r} , \quad (4.3)$$

where v is radial velocity at range r . Because the magnitude of r is tens of kilometers, and the magnitude of the second term is at times an order of magnitude larger than the first, the first term was neglected in the divergence algorithm. Divergence then, over any prescribed distance along a radial, can be approximated by

$$\text{Div}_r \approx \frac{\partial v}{\partial r} \approx \frac{\Delta v}{\Delta r} ; \quad (4.4)$$

and calculated in this study by

$$\text{Div}_r \approx (V_e - V_b)/(R_e - R_b) , \quad (4.5)$$

where V_b and V_e are begin and end velocities and R_b and R_e are begin and end ranges at the same locations along a single radar azimuth.

Computationally, (4.5) also represents radial shear, and is commonly used in this form by Doppler researchers. Therefore, a single-Doppler radar can be used to estimate radial divergence and radial shear over a prescribed range along the radar beam. Determining this interval along the radar beam creates a "divergence element" of radial divergence. Then, adjacent divergence elements can be sorted and combined to form an

area of radial divergence.

Flux

The air mass flux, F_1 , for circularly symmetric outflow in a thunderstorm with diameter D ,

$$F_1 = \pi D h \rho v , \quad (4.6)$$

where h is the vertical depth, ρ is the density, and v is the absolute value of outflow velocity at $D/2$. Therefore, the Doppler radar can be used to estimate the radial air mass flux, F_1 , over the height h . This height is approximately equal to the depth of the resolution volume. Consequently, for consistent outflow over heights larger than range resolution, h may be disregarded. Also, ρ and π are constants for the same relative height because they only change the magnitudes of the computations and don't affect relative comparisons. Therefore, for computational convenience, ρ and π are not included, and $2v = V_e - V_b$ can replace V . Thus, F_1 can be approximated by

$$F_1 \cong D (V_e - V_b) , \quad (4.7)$$

which is proportional to air mass flux per unit height.

In the divergence algorithm (NEXRAD JSPO Staff, 1985), this approach was applied and the flux (F) was approximated by

$$F \approx (R_e - R_b) (V_e - V_b) , \quad (4.8)$$

the product of the velocity difference with distance over which the difference is taken. Therefore, using the divergence element, an objective measurement of (radial) air mass flux within a prescribed range can be calculated. Using the divergence elements as determined by (4.5), and the patterns they create once summed, various estimates of flux of the areal pattern can be made. The next step is to determine if all of the detectable divergence elements belong in an areal pattern. This is accomplished by threshold testing prior to performing final calculations of the predictive variables for analysis.

Divergence Element Testing

After a divergence element has been identified, tests are conducted to see if it should be saved. These tests to determine if all the divergence elements belong to the areal pattern were conducted similar to Zrnic and Gal-Chen (1984) and Eyster (1985). However, this investigation adjusted the thresholds and added others to improve the detection of the divergence elements for application to non-tornadic thunderstorms.

Two values are calculated for each divergence element: radial velocity shear and radial flux. These values are then tested according

to the thresholds listed in Appendix D. If the divergence element meets the predetermined requirements, it is retained and termed a "pattern element." Once summed, the pattern elements (PELs) form an areal pattern as depicted in Fig. 10.

Predictive Variables

The variables generated by the storm divergence algorithm were examined and the variables listed in Table 5 were selected for further study because they were considered to be the ones which might provide the most predictive ability. Chapter V will outline the various variable-models used to predict strong low-level storm outflow. Appendix E reviews the calculation procedures and lists the storm divergence algorithm predictive variables. The reader may wish to refer to that appendix or the algorithm (Appendix F) for a more comprehensive understanding of the sequence in which the variables are computed.

Table 5. Storm divergence algorithm derived predictors of strong low-level outflow from non-tornadic thunderstorms.

Variable	Definition	Units
DIV	= divergence of areal pattern over time	s^{-1}
AREF	= reflectivity element area	km^2
MWF	= flux of areal pattern	$m s^{-1} km$
AFLX	= average flux of areal pattern	$m s^{-1} km^{-1}$
ADIV	= average divergence of areal pattern	$s^{-1} km^{-1}$
AVGF	= average radial flux of a PEL	$m s^{-1} km$
HGT	= beam center areal pattern height	km
AVGD	= average radial divergence of PEL	s^{-1}
AVGV	= average velocity difference of PELs	$m s^{-1}$
TDIV	= total radial divergence of PELs	s^{-1}
TFLX	= total radial flux of PELs	$m s^{-1} km$

CHAPTER V

METEOROLOGICAL ANALYSIS

Introduction

As noted earlier, over 30 non-tornadic thunderstorms met the established criteria for further study, but only 19 storms could be isolated adequately to provide reliable output. Of these 19 storms, 14 were used as a training set, and 5 were withheld for verification. Five additional storms, without surface verification data, were selected for classification (see Tables 2-4). Should an understanding of the sequence of meteorological events which occurred on each of the storm days be desired, the mesoscale environment for storms of 22 April, 27 June, and 28 June 1983 can be reviewed in Bonewitz (1986). Further, the mesoscale environmental events for the remaining storm days (13 May and 13 June 1983) can be found in Sickler et al. (1985a, 1985b).

This chapter presents three storms to show the relationships between the reflectivity and divergence patterns, and discusses idealized single-Doppler velocity patterns that were observed in each storm.

Cases

As mentioned earlier, three storms were selected for presentation. Each had a life cycle of one hour or slightly longer. The cases will be referred to as Storm 1, 5, and 9. Furthermore, each volume scan will be identified as V1 for the first volume scan, V2 for the second volume scan, and so on. The volume scan update rate was approximately 10 minutes and the volume scans covered successive sampling periods. Storms 1 and 9 had supportive SAM data; Storm 5, which was a "to be classified storm," had no surface wind observations.

Storm 1

Storm 1 occurred on 13 June 1983 southwest of NSSL and moved southeastward, with a life cycle from about 2030 to 2150 CST. The three volume scans of Doppler radar data examined were collected from 21:03:42 to 21:28:56 CST. The divergence algorithm variables used for low-level storm outflow predictions were extracted from the changes that occurred in the storm between volume one and two (V1 and V2) scans, with V2 storm summit sampling occurring at 21:19:10 CST.

The storm moved over the Fort Sill SAM complex (90-series) from the northwest with the onset of surface storm outflow from 2109 to 2112 CST and decline from 2124 to 2134 CST. The strongest winds recorded at the sites varied from 22-27 m s⁻¹, between 2120 and 2121 CST. Table 6 lists the Fort Sill Sam sites and wind speed information, while the

Table 6. Storm₁ surface outflow at the 90-series SAM sites. Outflow is in m s^{-1} and time is CST.

SITE	ONSET	PEAK (TIME)	DECLINE
91	2110	25 (2120)	2129
92	2111	25 (2121)	2124
93	2109	27 (2121)	2126
94	2111	22 (2120)	2134
95	2112	23 (2121)	2134

minute-to-minute maximum surface wind speeds for each site from 2100 to 2130 CST are at Fig. 12.

Figs. 13 and 14 depict the areal distribution of the storm at 21:04:40 and 21:14:22 CST, respectively. Note the displacement of the 20 dBZ leading edge during the lowest sampling elevation angle and its position directly over the Fort Sill SAM complex at 21:14:22 CST (Fig. 14). Although the scans depicted in these two figures represent the lowest elevation angle (0.6 deg), it should be noted that the SAM complex is 92 km from the radar and the height of the center of the beam is about 1300 m above ground level. Consequently, drawing inferences about low-level storm outflow with respect to the radar detected location of the storm and surface locations should be considered carefully because the beam may be too high to intercept outflow or provide sufficient evidence to couple that outflow to surface conditions.

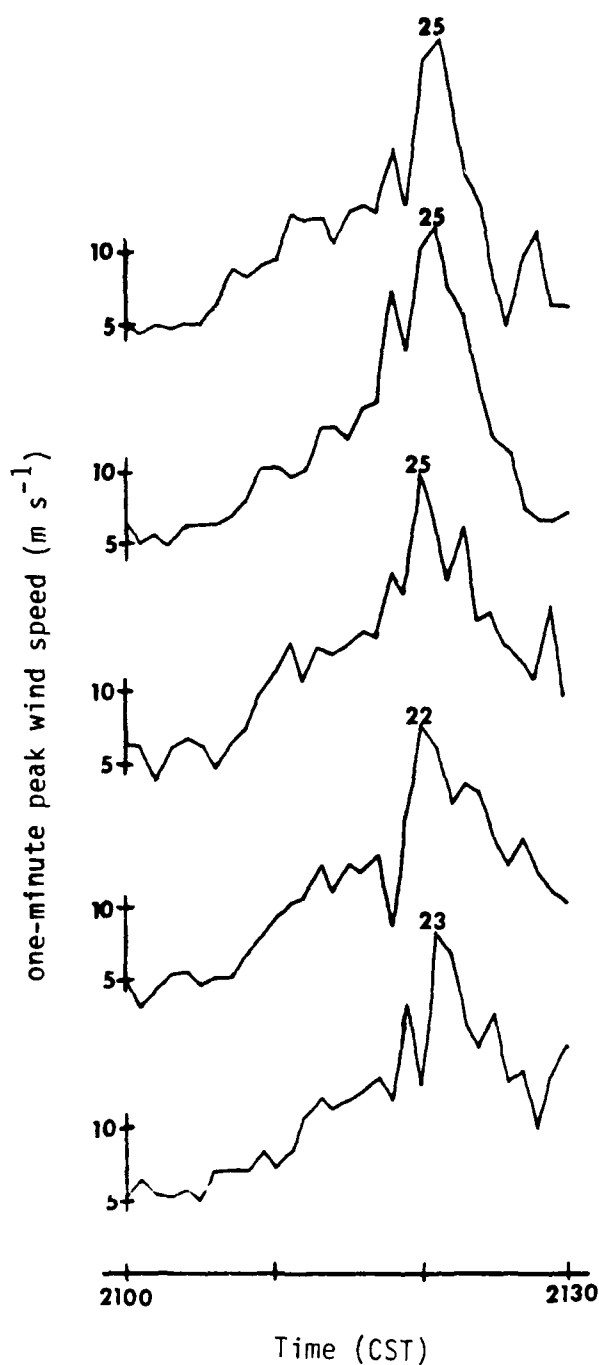


Fig. 12. SAM wind speed plot for 90-series complex for Storm 1 (2100 to 2130 CST). Storm 1 moved over the complex from the northwest. Consequently, since site 91 first recorded the surface winds it is at the top of the figure, while site 95, affected last, is at the bottom.

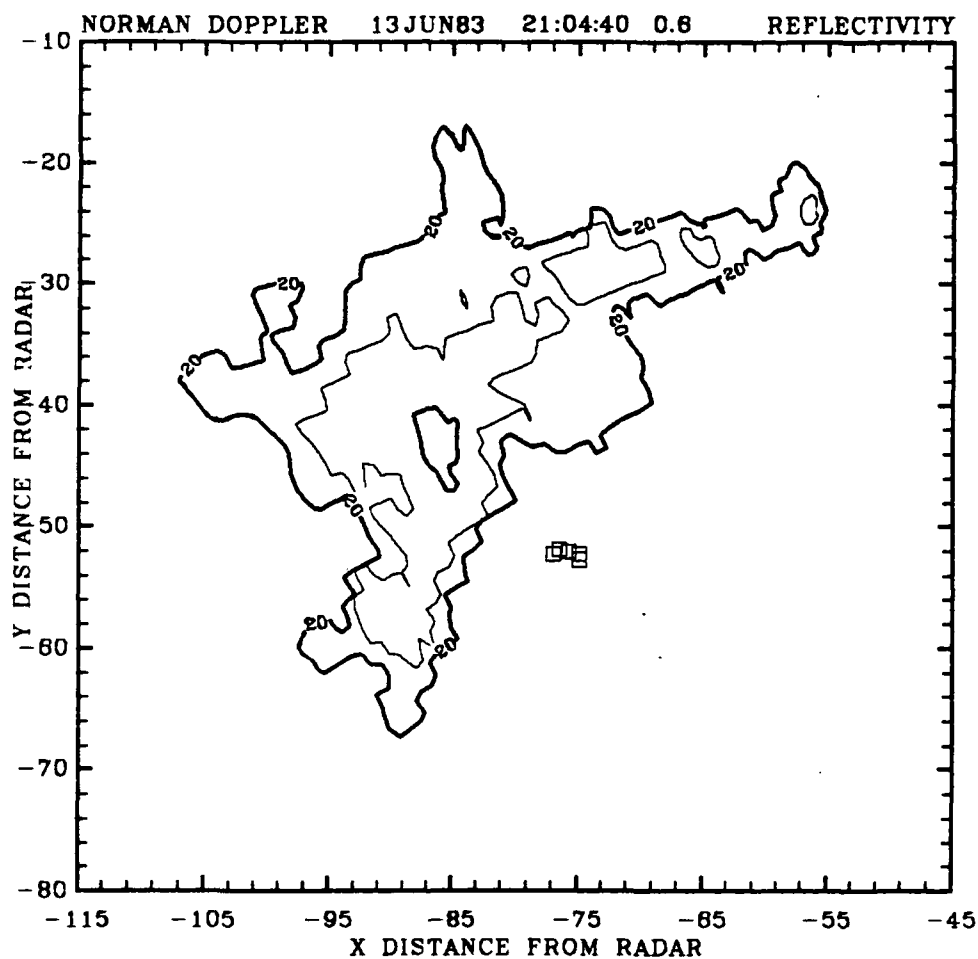


Fig. 13. Storm 1. Norman Doppler radar contoured reflectivity plot for 21:04:40 CST at 0.6 deg elevation on 13 June 1983. The 90-series SAM complex is denoted by the small boxes near the center of the figure. Reflectivity is contoured in dBZ.

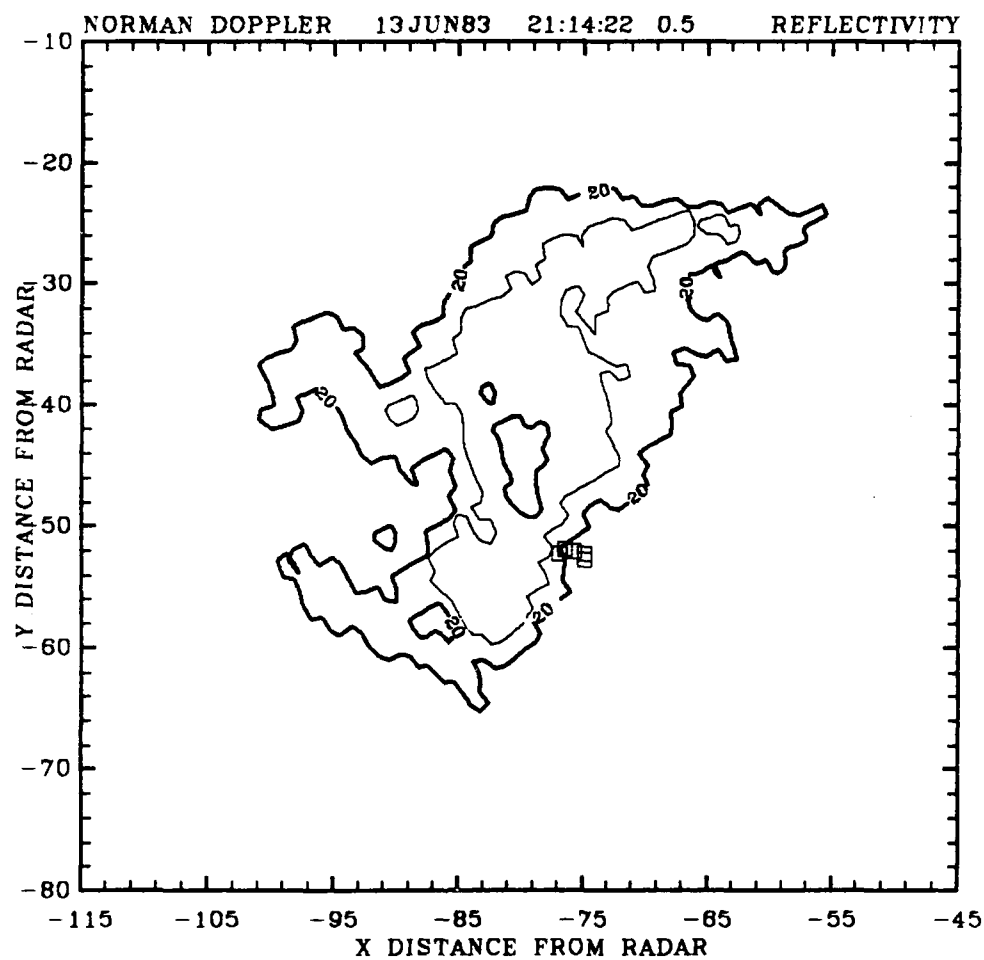


Fig. 14. As in Fig. 13, except for 21:14:22 CST at 0.5 deg elevation.

Storm 1 composite output, consisting of the contoured reflectivity and the derived areal pattern of radial divergence for all elevation angles of the second volume scan under study (V2) are shown in Figs. 15-19. As previously indicated, recall that an initial constraint of the algorithm was to threshold the data at 10 dBZ. Consequently, the radial divergence pattern occurs outside the 20 dBZ reflectivity contours of the storm. Close examination of the upper portions of the storm (Figs. 18 and 19) will reveal that the areal pattern of radial divergence sets up in preferred locations, along the edges of the storm and about the core (i.e., in the interior of the storm where the strongest reflectivities were observed) within the storm. This feature, the areal pattern of positive radial divergence, was observed to be consistently located at either side of the main storm core. To a lesser degree, the pattern elements would align themselves similarly in the lower levels of the storms, but less consistently. The upper portion of the storm's radial velocity field was observed to display a divergent signature (Fig. 3), or a slightly divergent anti-cyclonic signature (Fig. 7) at 21:09:28 CST, followed by convergent flow during contraction (at 21:19:10 CST).

Figs. 20 and 21 depict the vertical distributions of the reflectivity and divergence pattern elements through the depth of the storm. Storm 1's areal distribution (in km^2) of the 40 dBZ field from 21:03:42 to 21:28:56 CST is shown in Fig. 20 for each elevation angle. Inspection of the figure shows the 40 dBZ reflectivity field apparently sinking below the upper-levels of the storm to lower elevations between

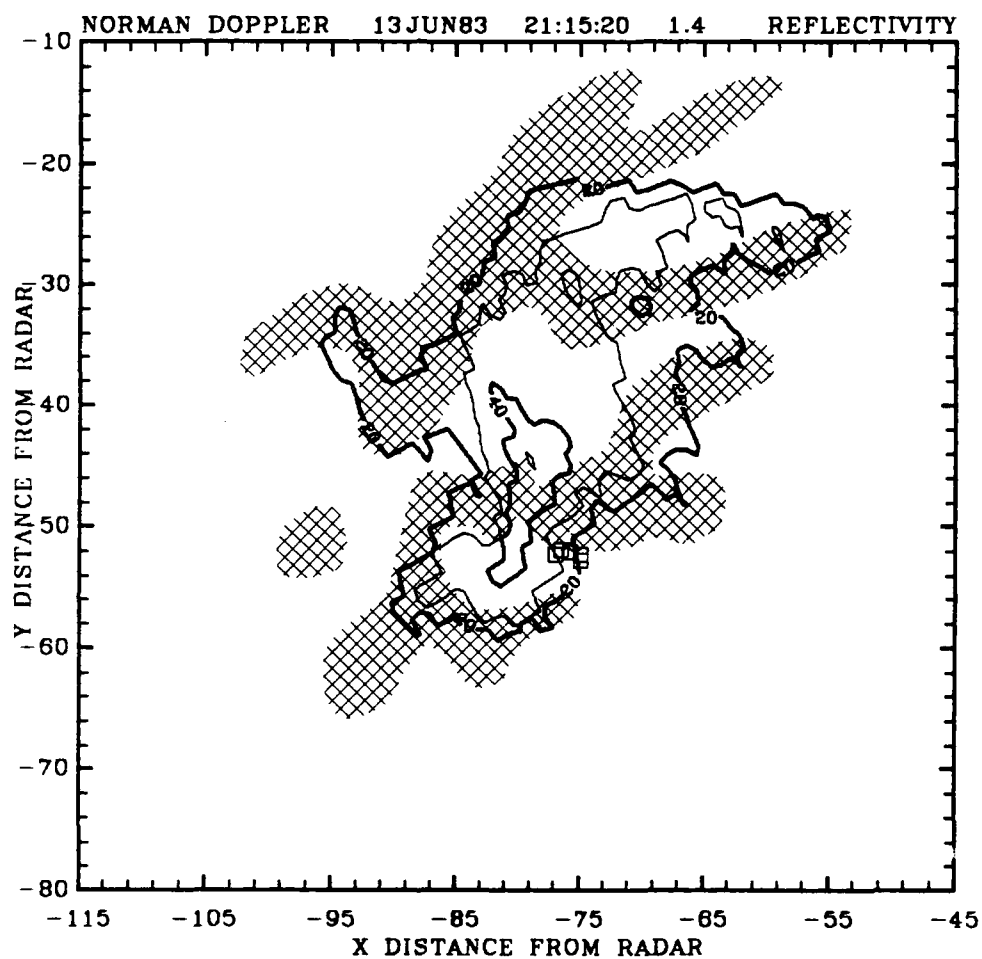


Fig. 15. Storm 1. Composite of reflectivity (contours) and positive radial divergence (cross-hatch) for 21:15:20 CST at 1.4 deg elevation. Divergence determined using storm algorithm.

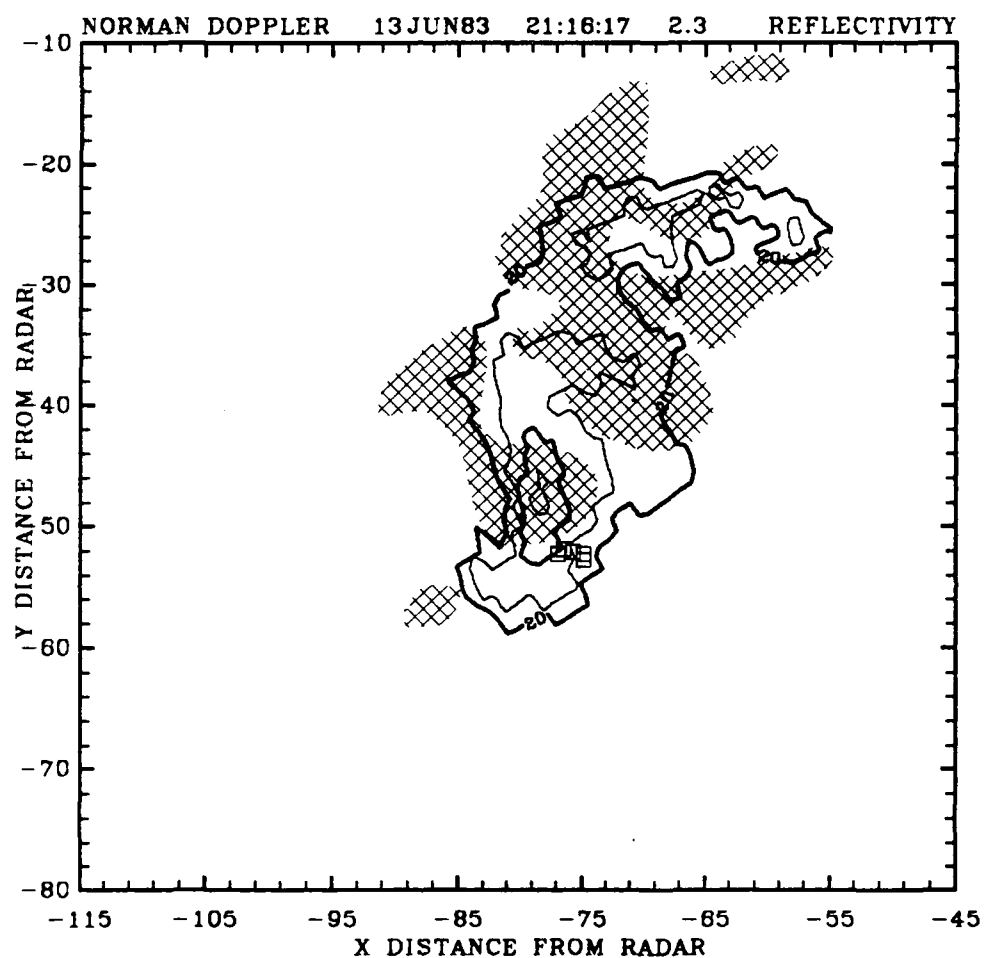


Fig. 16. As in Fig. 15, except for 21:16:17 CST at 2.3 deg elevation.

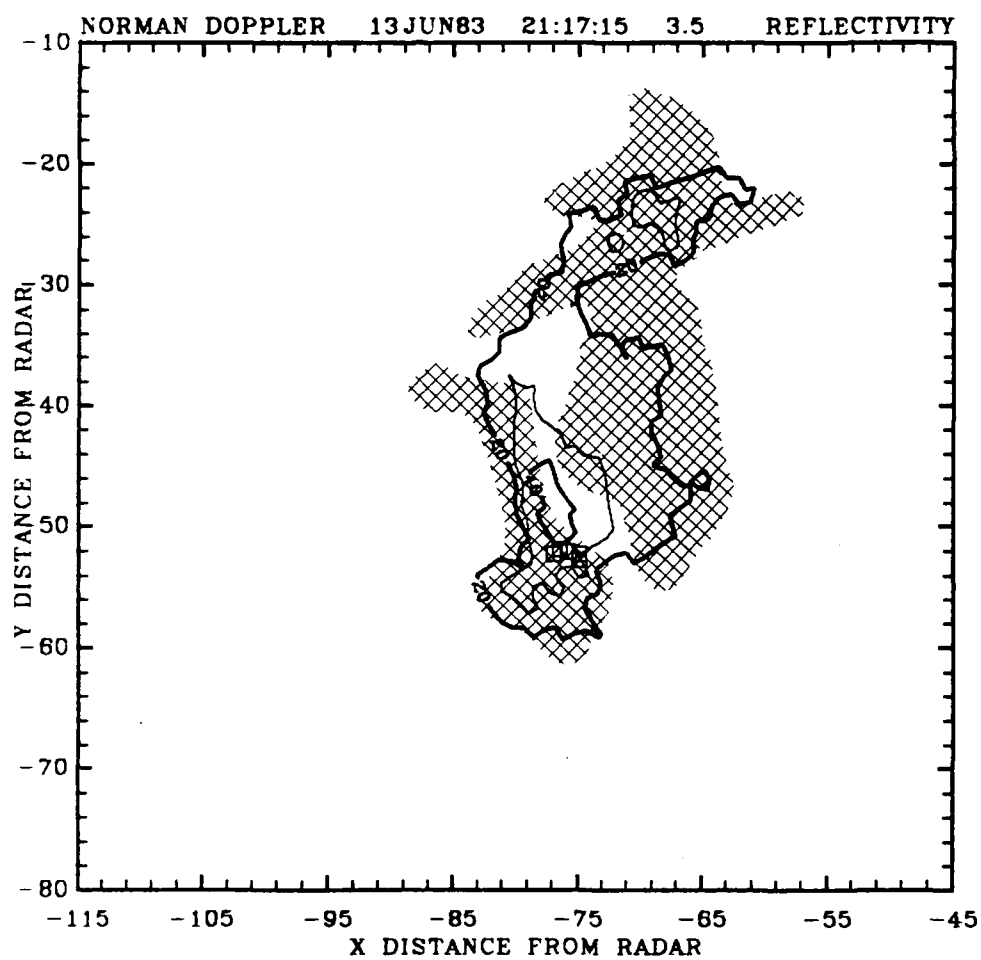


Fig. 17. As in Fig. 15, except for 21:17:15 CST at 3.5 deg elevation.

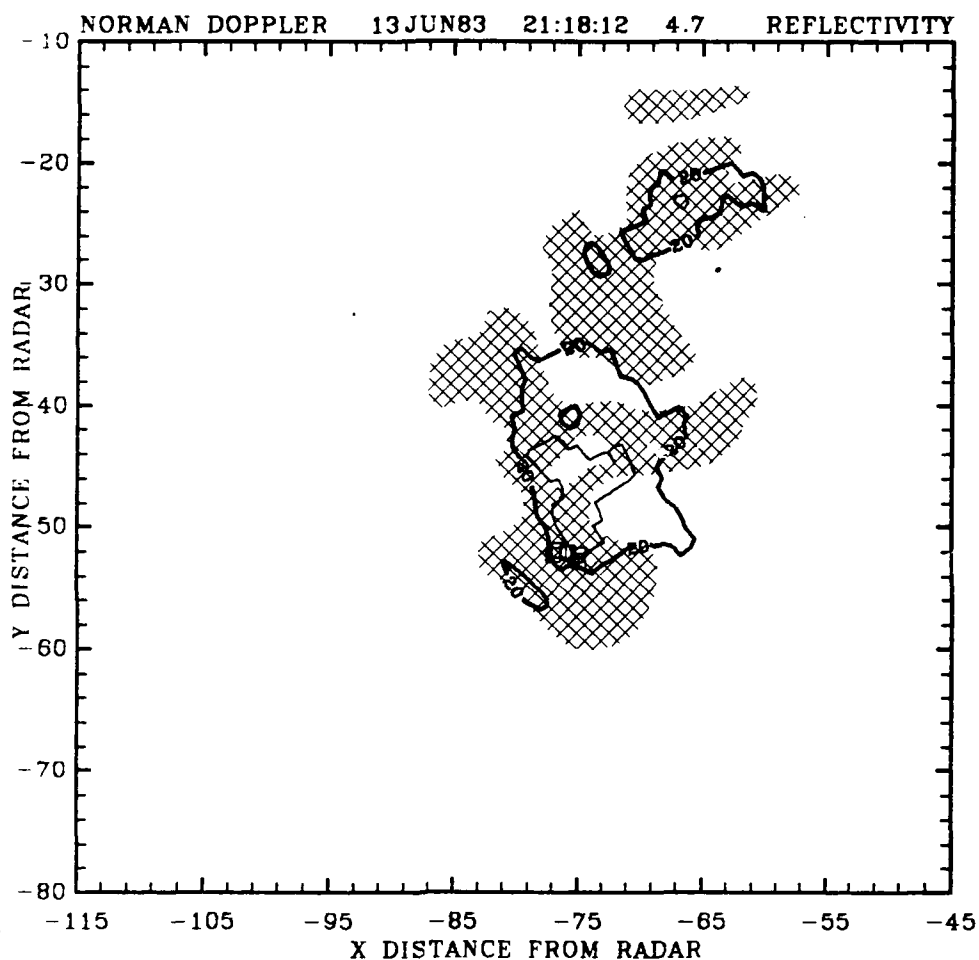


Fig. 18. As in Fig. 15, except for 21:18:12 CST at 4.7 deg elevation.

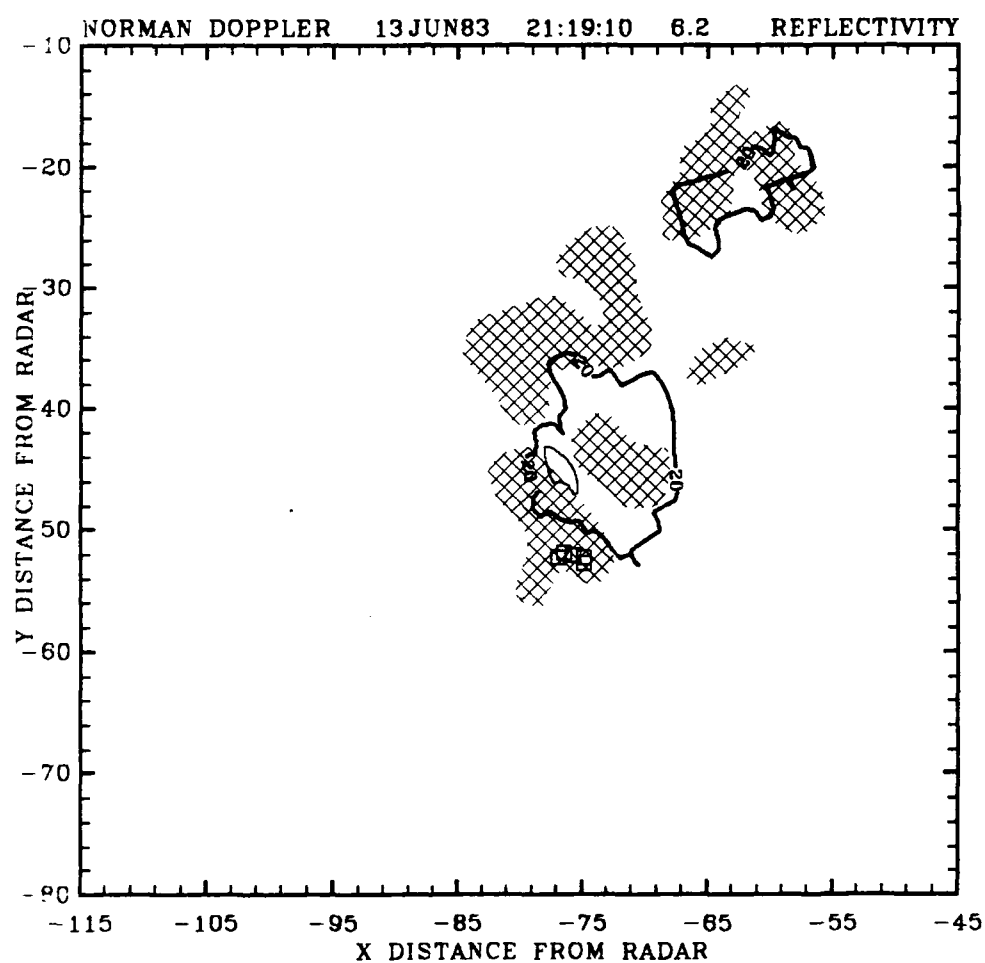


Fig. 19. As in Fig. 15, except for 21:19:10 CST at 6.2 deg elevation.

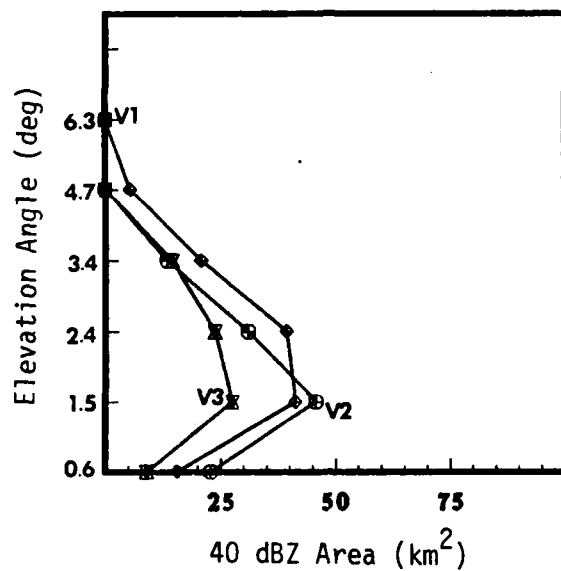


Fig. 20. Distribution of the area enclosed by the 40 dBZ contour during three successive volume scans (V1, V2, and V3) for Storm 1.

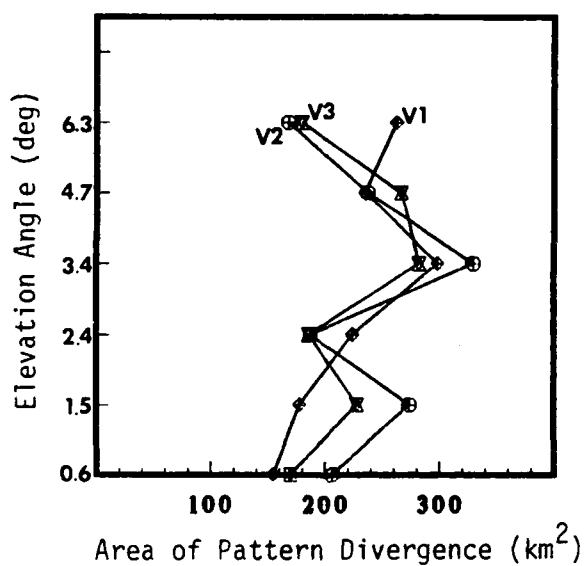


Fig. 21. Derived area of radial divergence during three successive volume scans (V1, V2, and V3) for Storm 1.

V1 to V2. During this same period, the 40 dBZ reflectivity expands at the lower levels of the storm (1.5 and 0.6 deg elevation). During V3, while the upper-levels of the storm's 40 dBZ reflectivity maintains about the same areal distribution, it contracts in the mid- and lower-levels (2.4, 1.5, and 0.6 deg elevation) as it begins to decay, indicative of storm outflow. These observations are consistent with storm theory reviewed earlier. The change of the radial divergence pattern at each elevation angle during the same period can be inferred from Fig. 21. Note that the areal pattern of radial divergence contracts at the storm summit from V1 to V2, and expands in the lower-levels with a measure of consistency with the areal distribution of the 40 dBZ field (Fig. 20). However, inconsistent with the 40 dBZ reflectivity (Fig. 20), the radial divergence field at the 2.4 deg elevation angle is noted to apparently contract. This inconsistency could have been caused by the viewing angle alignment of the storm with respect to the radar beam (see Appendix G).

By applying equation (4.2) during successive changes in the areal pattern of divergence from V1 to V2 and V2 to V3 (illustrated by Figs. 15-19 and shown in Fig. 21), the divergence from the change in the pattern of radial divergence was computed (Fig. 22). This was done to determine if the areal pattern of radial divergence would reflect changes of divergence at the storm summit and through the storm in a way consistent with storm theory. Interestingly, the changes of divergence in the vertical imply a qualitative description of the

likely true field. At storm summit, between V1 to V2, less divergence is noted on the composites of reflectivity and radial divergence due to the shrinking of the areal radial divergence pattern, while at lower levels, marked divergence is displayed over the same period.

Consistent with the observed patterns, the calculated divergence from the changes of the patterns of radial divergence (Fig. 21) show negative divergence from sampling period V1 to V2, while low-levels are noted to display a good divergence signal over the same interval. This latter observation is consistent with expected low-level storm divergence (i.e., outflow) which is confirmed by the Fort Sill SAM wind speed plots (Fig. 12), where the strongest winds were recorded at 2020 to 2021 CST, two minutes after V2 Doppler data was collected at the storm summit. This indicates that upper-level changes may be coupled with the formation or strengthening in the storm downdraft and the transfer of storm mass from upper levels to mid and low levels, as noted by the strong outflow recorded at the Fort Sill SAMs (Fig. 12) and exhibited by a divergence signature in Fig. 22.

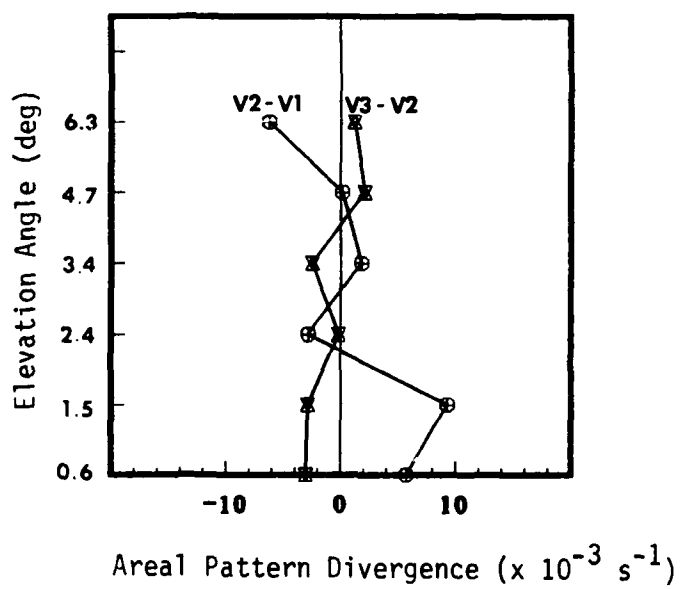


Fig. 22. Calculated divergence from changes in the area of divergence shown in Fig. 21. Each level corresponds to the elevation angles sampled.

Storm 9

Storm 9 occurred on 27 June 1983, west of NSSL and moved northeastward, with a life cycle from about 1935 to 2035 CST. The four volume scans of Doppler radar data examined were collected from 19:45:42 to 20:23:33 CST. The divergence algorithm variables used for low-level storm outflow predictions were calculated at the time intervals of V1 and V2, with storm summit sampling of V2 occurring at 20:21:34 CST.

The storm moved over the Fort Reno SAM complex (60-series) and shortly thereafter, went on to affect the Wiley Post SAM complex (40-series), passing just to the west, moving toward the northeast. Onset at the Fort Reno SAM complex was from 1956 to 2007 CST and declined from 2015 to 2029 CST. The strongest winds recorded at the Fort Reno sites ranged from 25-32 m s^{-1} , between 1956 to 2007 CST. Table 7 lists surface wind speeds recorded at the Fort Reno sites. Fig. 23 depicts the minute-to-minute maximum surface wind speeds for each site from 1950 to 2020 CST. Effects of Storm 9 at the Wiley Post SAM sites were first recorded from 2007 to 2008 CST and moved on from 2021 to 2024 CST. The strongest winds recorded ranged from 19-26 m s^{-1} , between 2015 to 2021 CST. Table 8 lists wind speeds recorded at the Wiley Post SAM complex, while Fig. 24 depicts variations of the surface wind speeds at the Wiley Post SAM complex from 2000 to 2030 CST. Note that the overall intensity and duration of the outflow at the Fort Reno SAM complex is greater than that recorded at the Wiley Post SAM complex. This implies either that the storm was decaying and

Table 7. Storm 9 surface outflow at the 60-series SAM sites. Outflow in m s^{-1} and time is CST. Note that SAM site 65 was not operational during this period.

SITE	ONSET	PEAK (TIME)	DECLINE
61	1956	32 (1957)	2023
62	1956	25 (1956)	2015
63	1956	27 (2007)	2024
64	1957	30 (2007)	2029

Table 8. Storm 9 surface outflow at the 40-series SAM sites. Outflow in m s^{-1} and time is CST.

SITE	ONSET	PEAK (TIME)	DECLINE
41	2007	26 (2017)	2023
42	2008	21 (2021)	2021
43	2008	19 (2015)	2021
44	2007	22 (2016)	2024

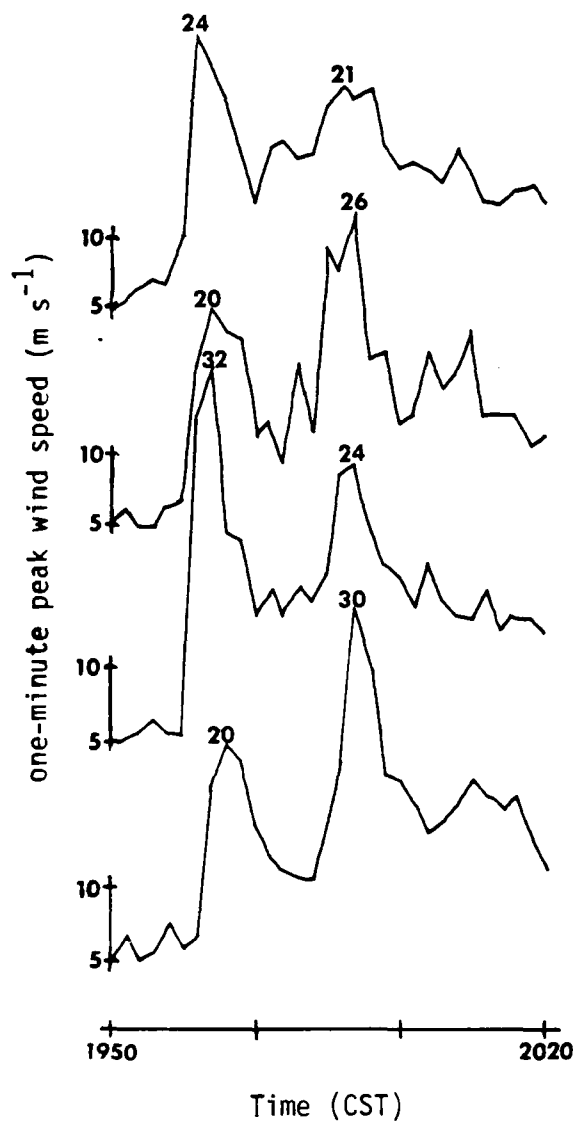


Fig. 23. SAM wind speed speed plot for 60-series complex for Storm 9 (1950 to 2020). Storm 9 moved over the SAM complex from the southwest. First site (61) affected at the top of figure, while last affected at bottom.

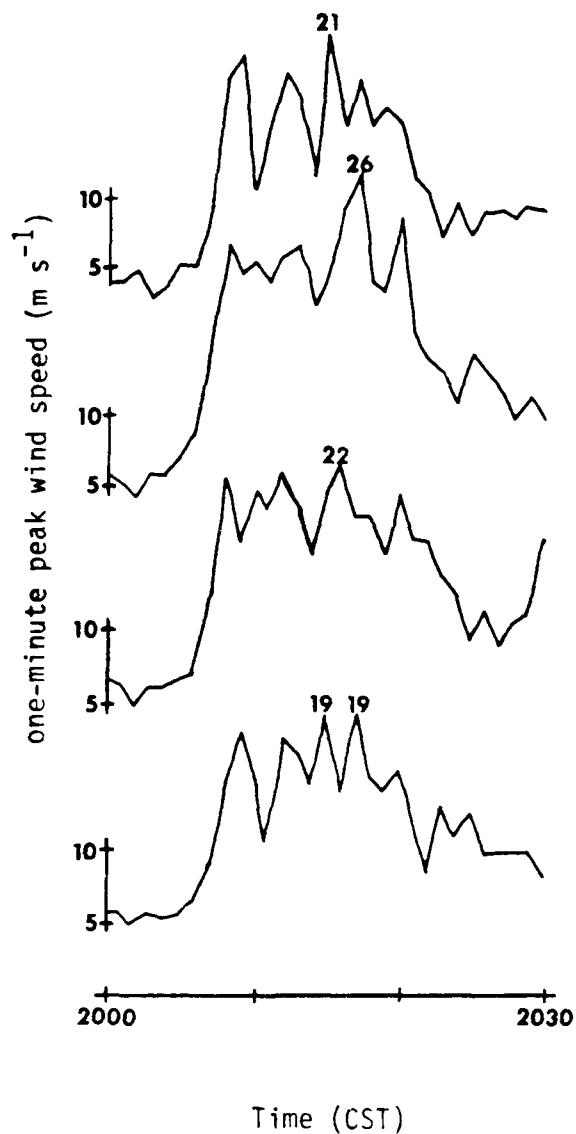


Fig. 24. SAM wind speed plot for 40-series complex for Storm 9 (2000 to 2030 CST). First affected at top, last at bottom.

losing its velocity or that the full effects were not felt over the Wiley Post area. The composite reflectivity and radial divergence pattern for 20:21:34 CST will show that the only divergence detectable by the algorithm at the storm summit was in the vicinity of the Wiley Post SAM sites. Furthermore, note in Fig. 23 how the outflow indicates a sharp increase at approximately 1957 CST at Fort Reno sites followed by a secondary surge at 2007 CST. In contrast, the Wiley Post sites received multiple surges, but of lesser intensity.

The areal distribution of the storm from 19:45:42 to 20:15:46 CST is depicted at Figs. 25-28. Note that the storm begins to move over the Fort Reno SAM complex at 19:56:22 CST (Fig. 26) and then at 20:15:46 CST (Fig. 28) begins to move into the vicinity of the Wiley Post SAM complex and influence the surface winds in and near that area. Also, as mentioned in Storm 1, note that the center of the radar beam at the lowest elevation angle (0.5 deg) is about 780 m and 400 m above the ground over the Fort Reno (63 km away) and Wiley Post (37 km away) SAM complexes, respectively.

The composite output of the reflectivity and the algorithm's areal pattern of radial divergence for the top two elevation angles (6.3 and 8.7 deg) for V2, V3, and V4 from 20:01:11 to 20:21:34 CST are at Figs. 29-34. Inspection reveals preferred positioning of the areal pattern of radial divergence about the storm core. Further inspection reveals the decay of the storm summit over this time interval. Interestingly, even after the 20 dBZ contour apparently sinks below the storm summit at 20:21:34 CST, the areal pattern of radial divergence is still

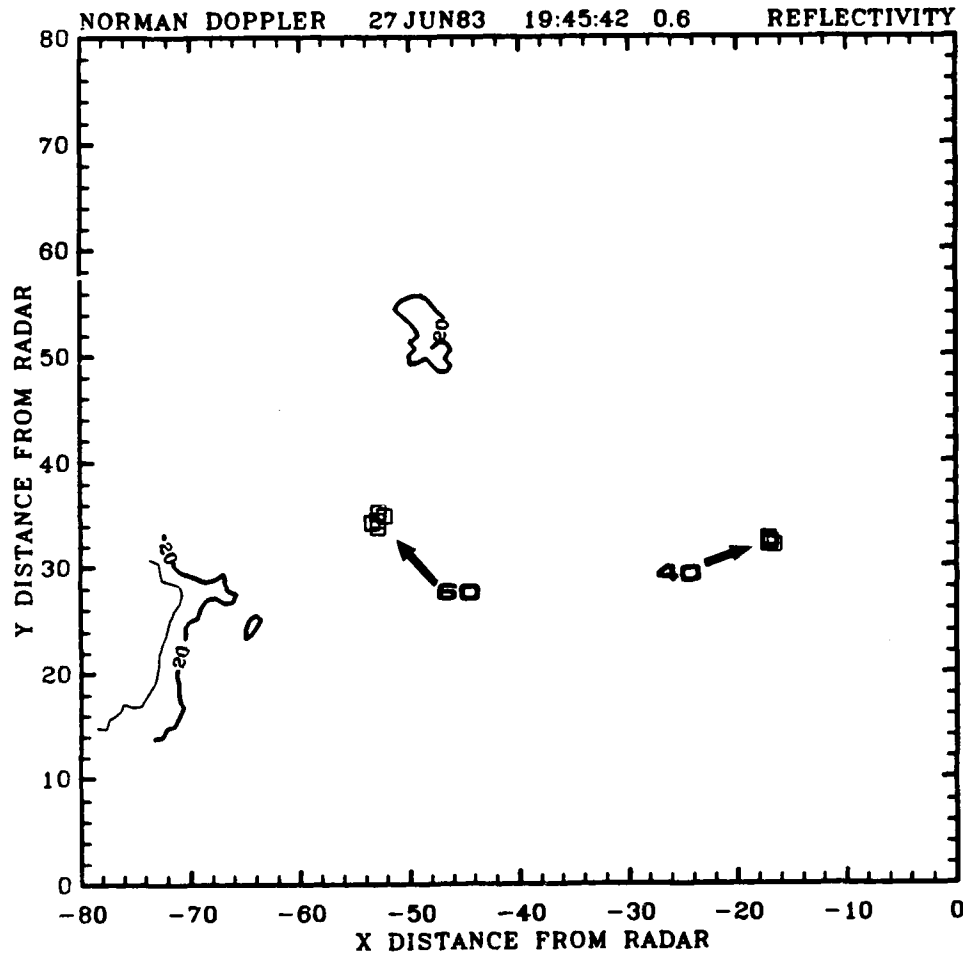


Fig. 25. Storm 9. Norman Doppler radar contoured reflectivity plot for 19:45:42 CST at 0.6 deg elevation on 27 June 1983. Arrows denote locations of SAM complexes. Reflectivity is contoured in dBZ.

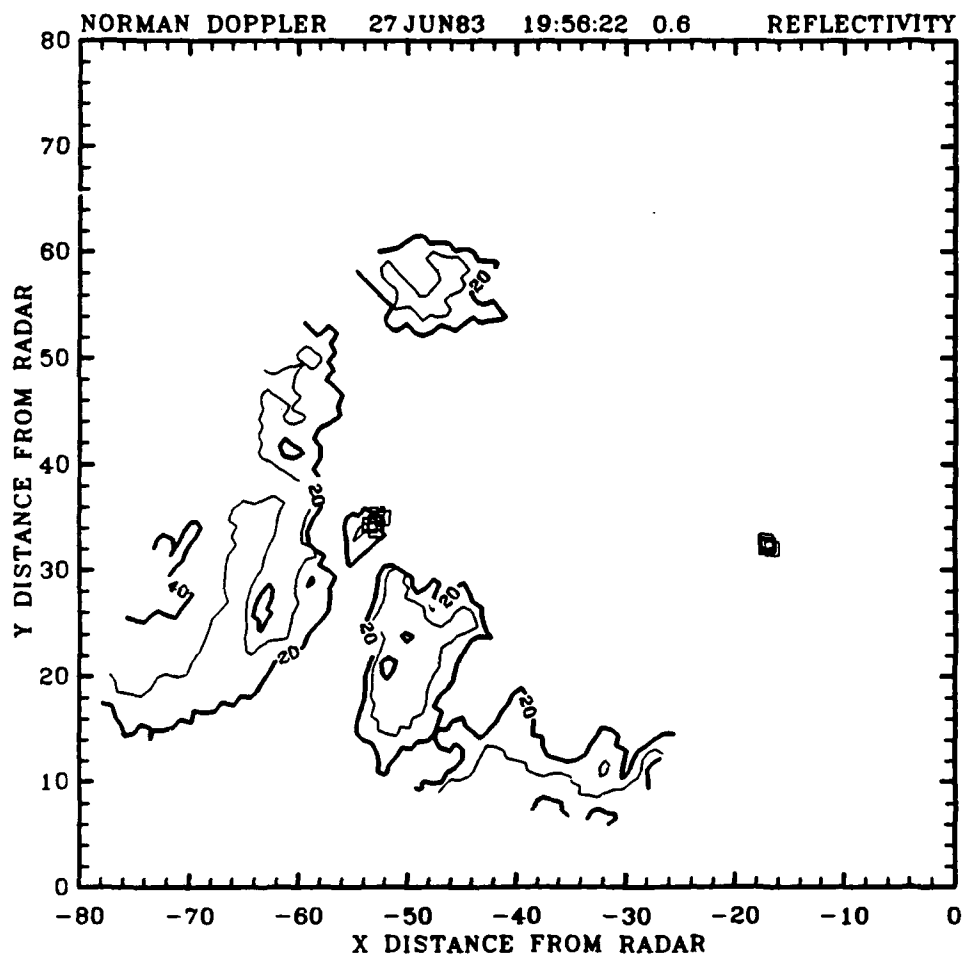


Fig. 26. As in Fig. 25, except for 19:56:22 CST.

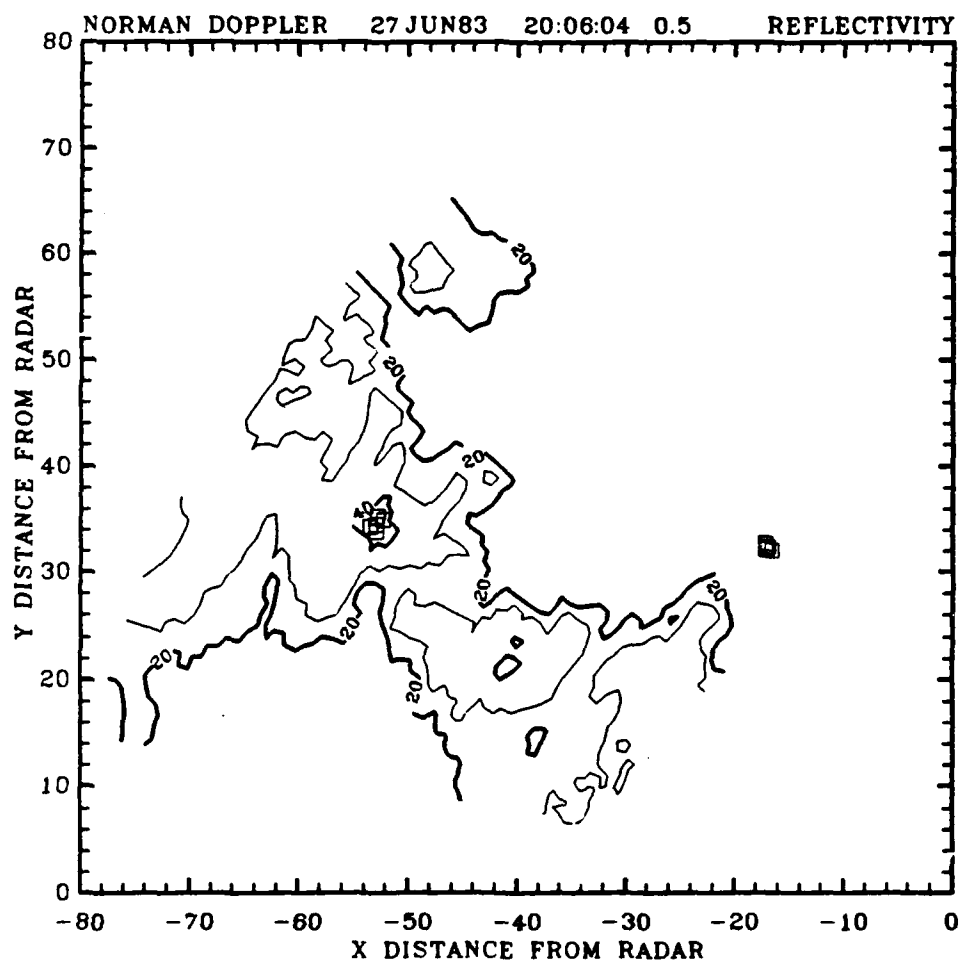


Fig. 27. As in Fig. 25, except for 20:06:04 CST.

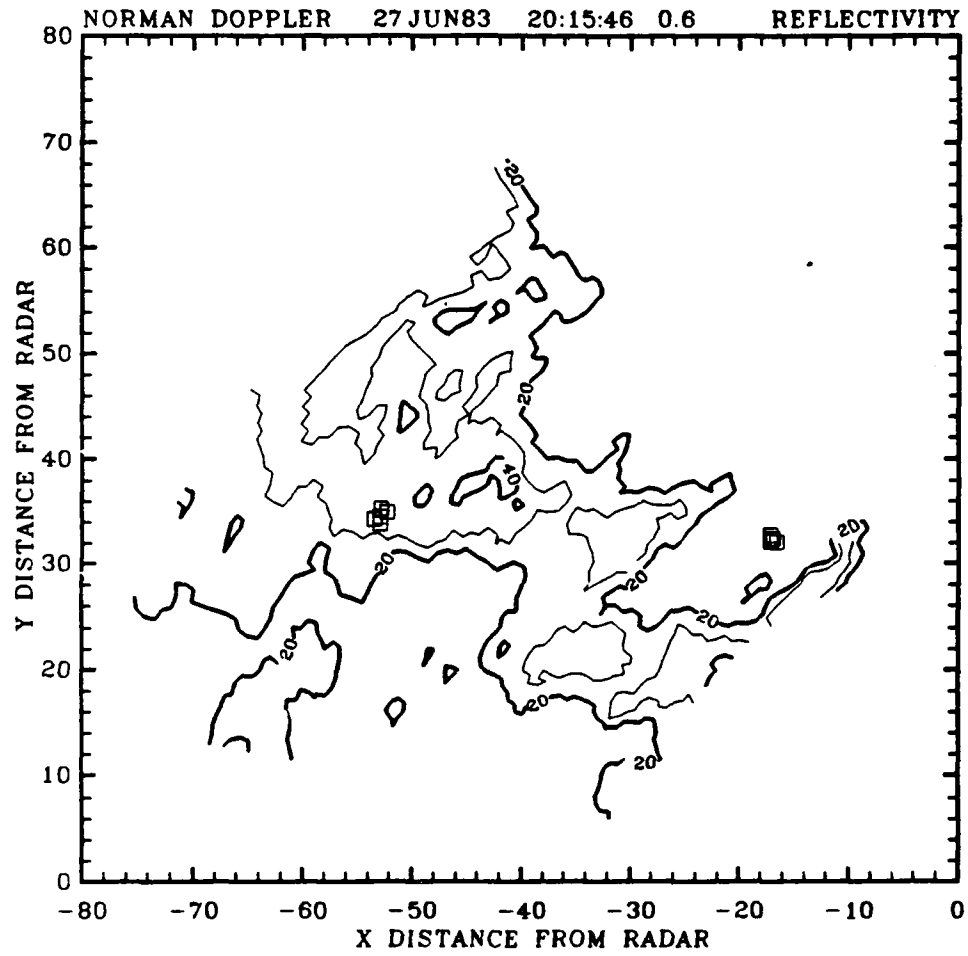


Fig. 28. As in Fig. 25, except for 20:15:46 CST.

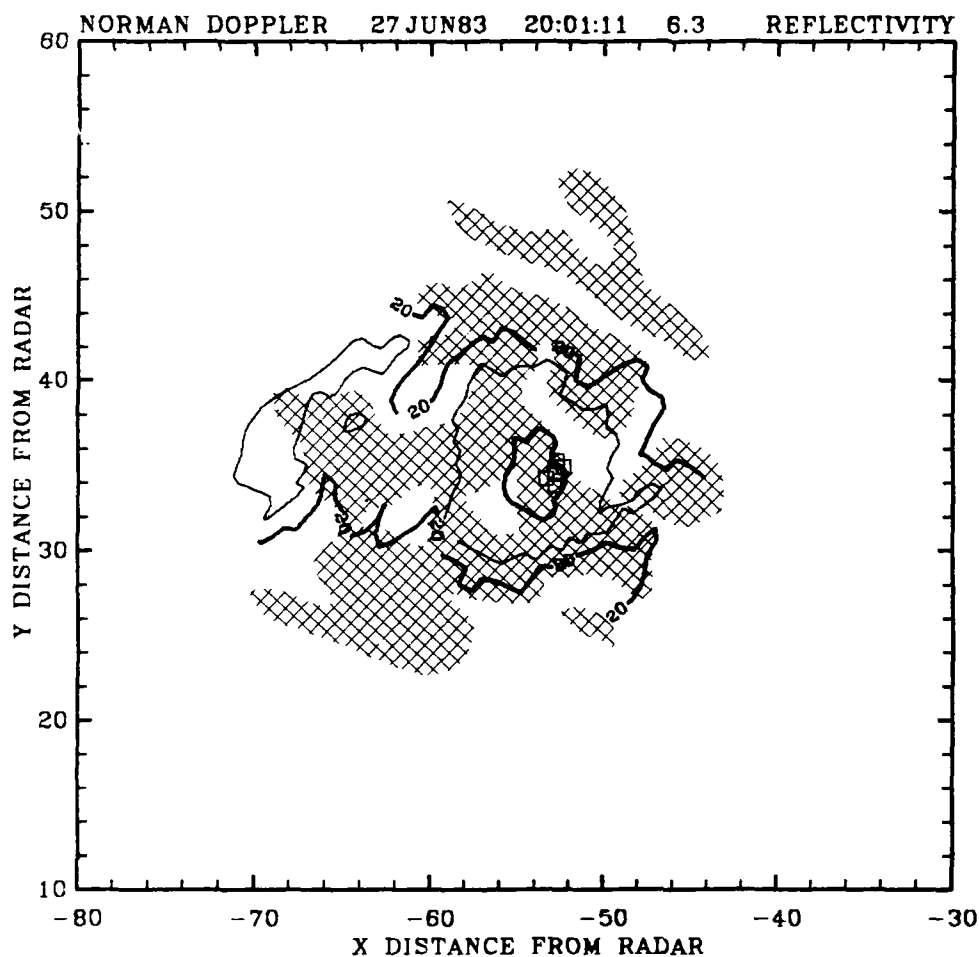


Fig. 29. Storm 9. Composite reflectivity (contours) and positive radial divergence (cross-hatching) for 20:01:11 CST at 6.3 deg elevation. Divergence determined using storm algorithm.

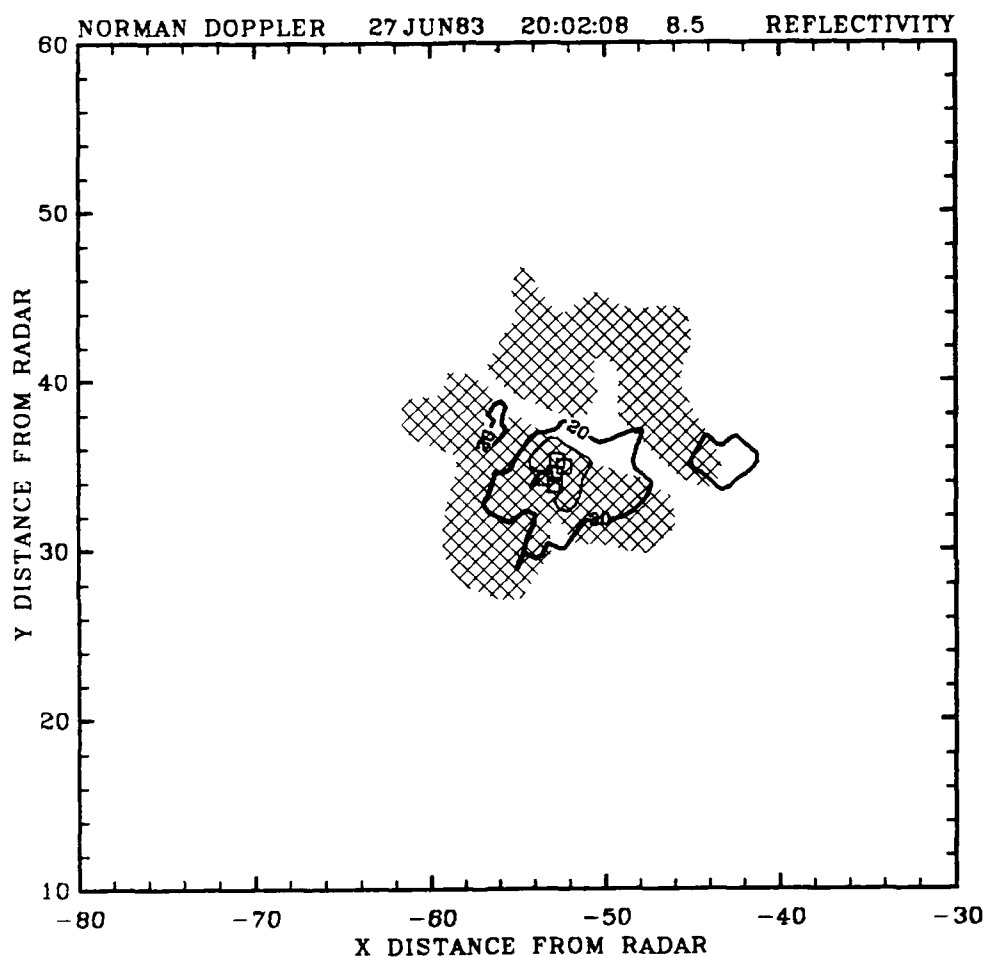


Fig. 30. As in Fig. 29, except for 20:02:08 CST at 8.5 deg elevation.

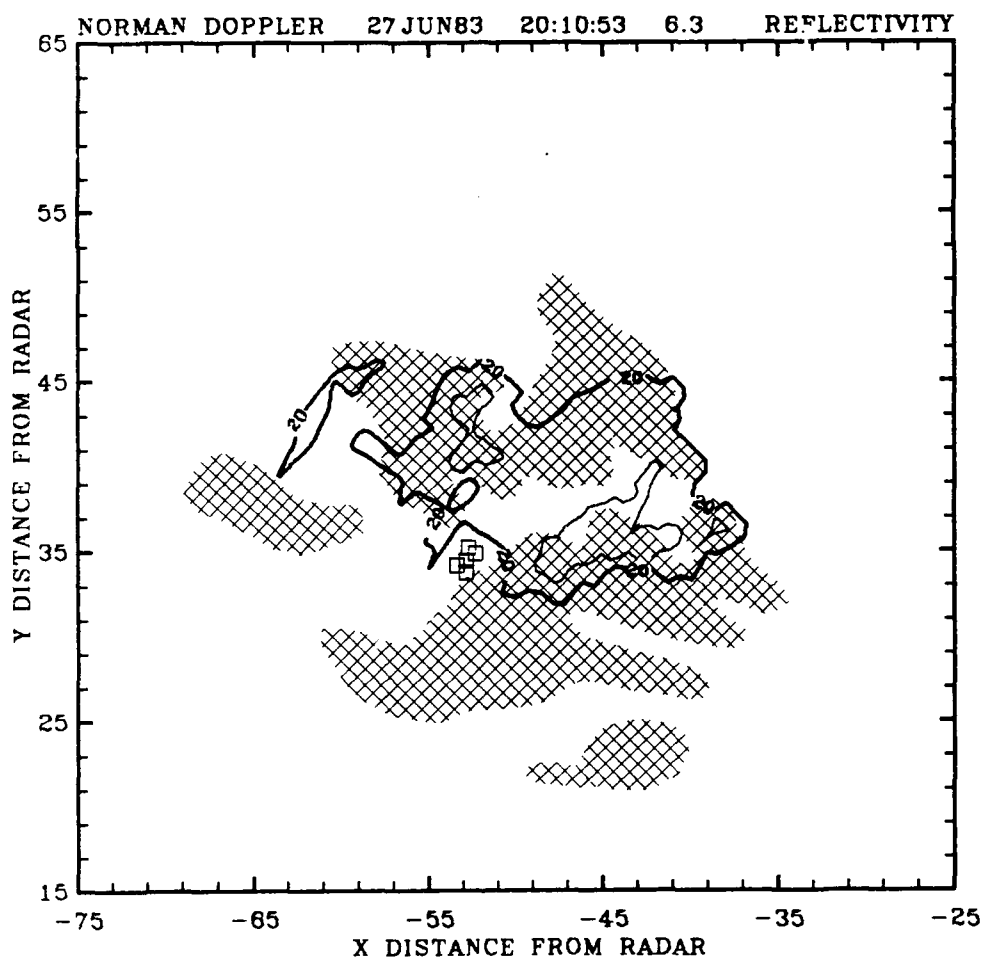


Fig. 31. As in Fig. 29, except for 20:10:53 CST at 6.3 deg elevation.

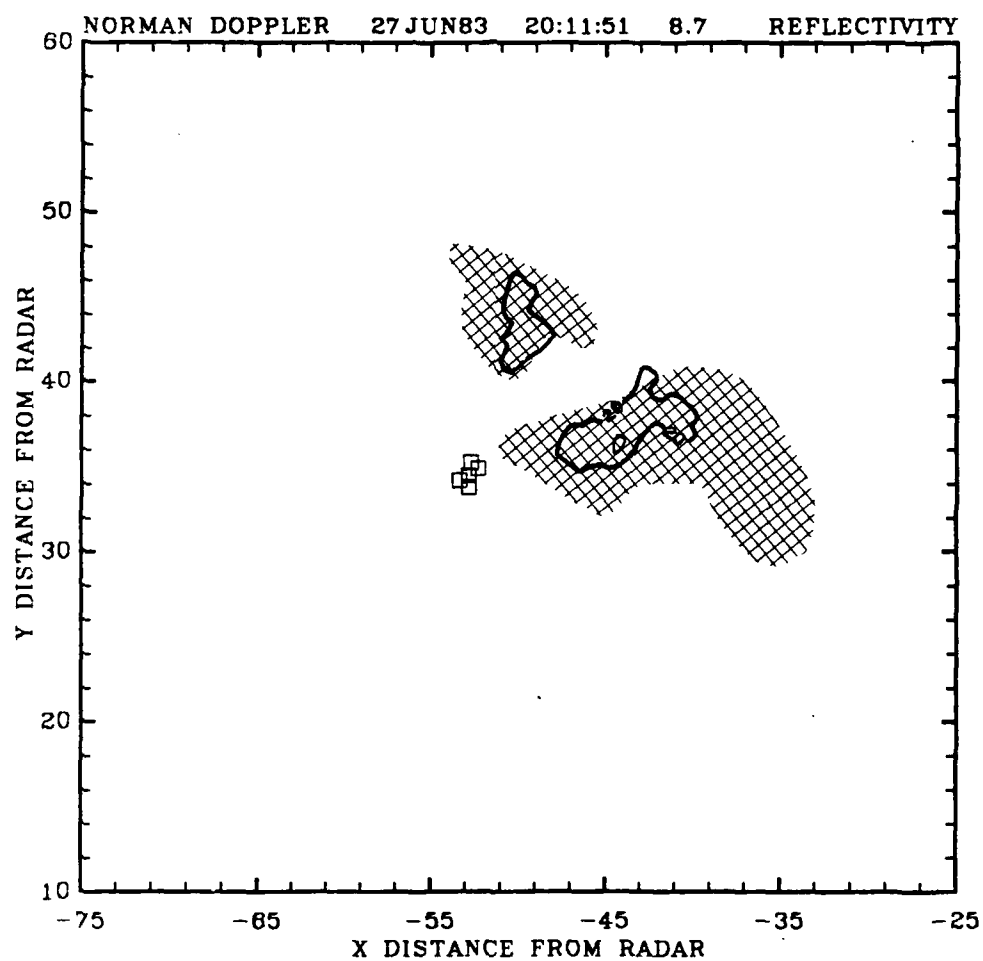


Fig. 32. As in Fig. 29, except for 20:11:51 CST at 8.7 deg elevation.

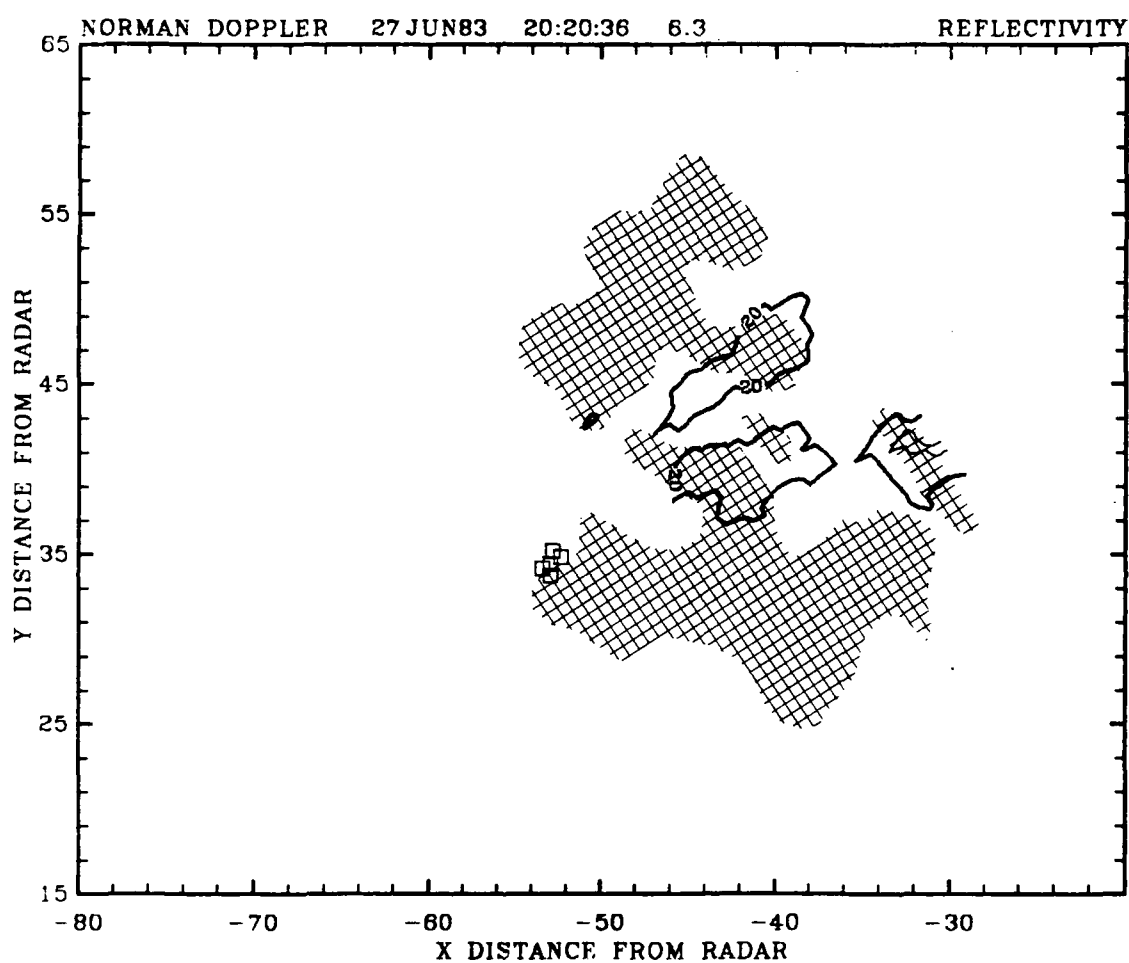


Fig. 33. As in Fig. 29, except for 20:20:36 CST at 6.3 deg elevation.

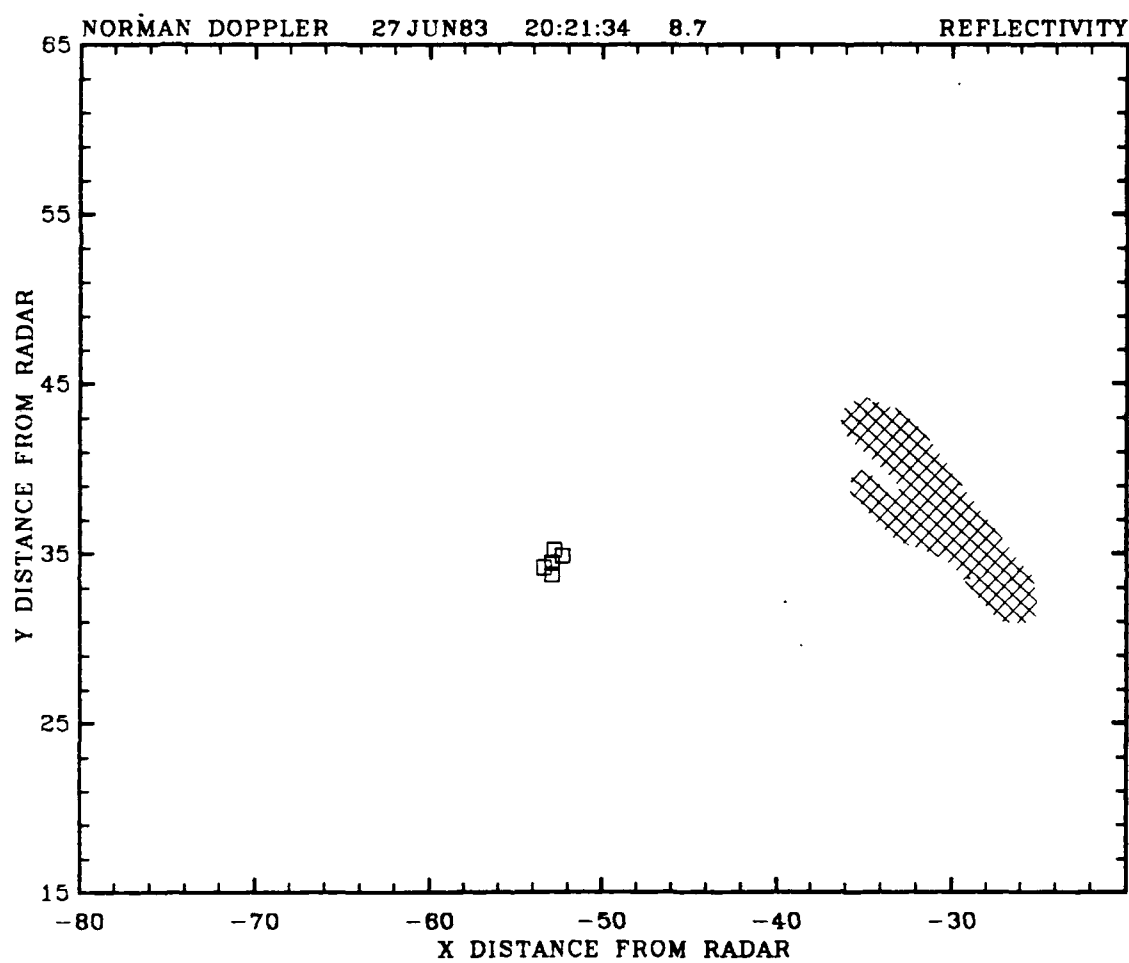


Fig. 34. As in Fig. 29, except for 20:21:34 CST at 8.7 deg elevation.

apparent (Fig. 34). This feature, radial divergence, is located directly over the Wiley Post SAMs. Comparisons of the Wiley Post surface wind speeds for 2000 to 2030 CST (Fig. 24) reveals that this feature occurs during or after most of the strongest outflow detectable at the surface near that area. As in Storm 1, the radial velocity field in the upper portions of the storm was observed to be divergent, displaying a pattern similar to divergent anti-cyclonic flow (Fig. 7), followed by convergent flow. Neither a cyclonic nor a anti-cyclonic convergent flow pattern was distinguishable during the contraction of the storm summit.

Similar to Storm 1, Storm 9's areal distribution (in km^2) of the 40 dBZ field at each elevation angle sampled for each volume scan from 19:45:42 to 20:23:33 CST was constructed (Fig. 35). Once again, Storm 9 exhibits a trend similar to Storm 1, sinking in the upper levels as the mid levels expand. However, unlike Storm 1 (Fig. 20), Storm 9 (Fig. 35) consistently decays during the latter stage of its life cycle. The changes in the radial divergence fields for Storm 9 (Fig. 36) do not demonstrate the measure of consistency to the reflectivity field (Fig. 35) as seen in Storm 1 (comparing Figs. 20 and 21). Comparisons between Storms 1 and 9, show Storm 9 to be consistent during V1 to V2, but from V2 to V3 Storm 9 expands (Fig. 36), whereas Fig. 35 indicates a shrinking during the same period.

Applying equation (4.2) the calculated divergence from successive volume scans of the storm is shown at Fig. 37. While the divergence pattern aloft shows little change, the mid levels become increasingly

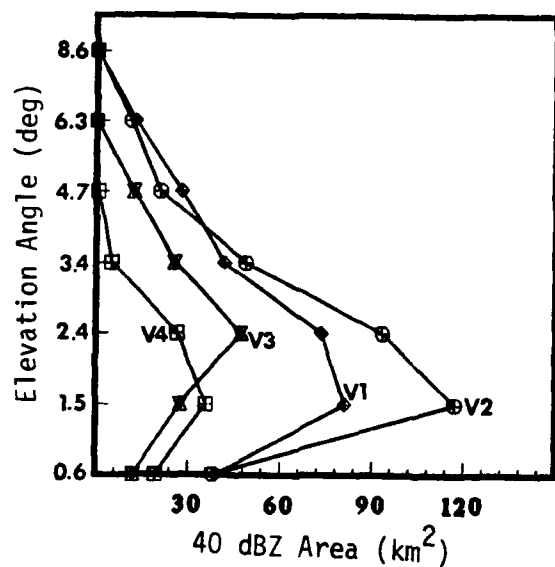


Fig. 35. Distribution of the area enclosed by the 40 dBZ contour during four successive volume scans (V1, V2, V3, and V4) for Storm 9.

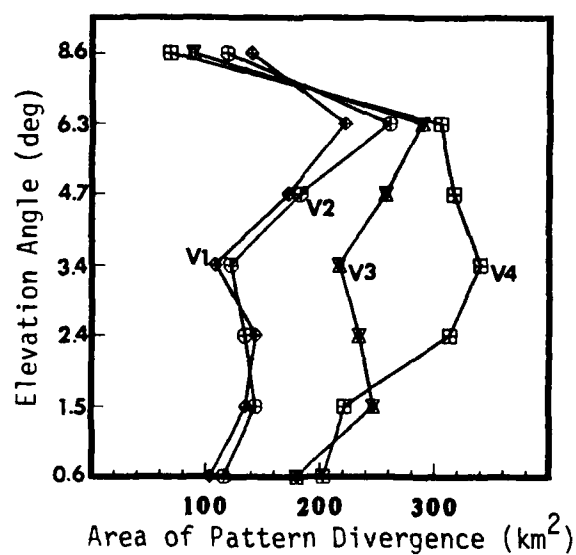


Fig. 36. Derived area of radial divergence during four successive volume scans (V1, V2, V3, and V4) for Storm 9.

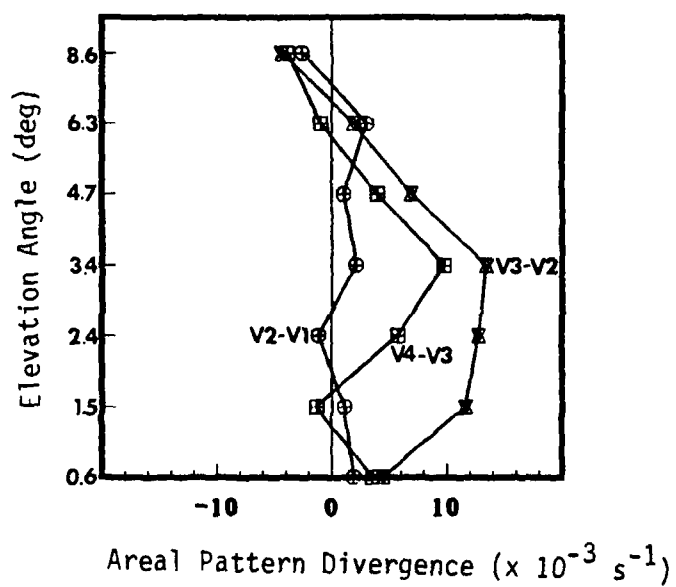


Fig. 37. Calculated divergence from the changes in the area of divergence shown in Fig. 36. Each level corresponds to the elevation angle.

divergent from V2 to V3 and then less divergent from V3 to V4. This indicates little change aloft with enhanced divergence during V2 to V3 in the mid levels followed by somewhat weaker mid-level divergence during V3 to V4. This pattern, when viewed with the composites of reflectivity and radial divergence (Figs. 29-34), accurately portrays the situation. That is, they both support the conclusion that the storm is decaying. The divergence pattern in Fig. 37 depicts a storm with steady convergence aloft, while the storm composites for the highest elevations clearly indicate decay (Figs. 30, 32, and 34).

Storm 5

Storm 5 occurred on 27 June 1983 north-northwest of NSSL and moved northward, with a life cycle from about 1945 to 2045 CST. The four volume scans of Doppler radar data examined were collected from 19:55:33 to 20:30:29 CST. The divergence algorithm variables used for prediction of low-level outflow were computed during the time interval between V2 and V3, with the storm summit sampling of V3 occurring at 20:21:40 CST. One of the convenient aspects of this storm is that it occurred away from other storms, making it an easy storm to isolate and an excellent candidate to classify because there was no contamination from other storms to remove.

Composite output of the reflectivity and the algorithm's radial divergence for the top four elevation angles are shown in Figs. 38-49. Note the changes that occur from V1 to V3 in each figure. The mid levels of the storm (elevations 3.5 and 4.7 deg) exhibit a small reflectivity with little radial divergence being detected during the early stages of the storm life cycle. At the same time, an increase of upper-level reflectivity and radial divergence (elevation 8.7 deg) as seen in V2 (Fig. 45) followed by a decrease in V3 (Fig. 49). Also, note the growth in the mid levels, as the reflectivity field at storm summit drops to mid-levels and, likely, even lower. A review of the radial velocity fields revealed rotation through the upper half of this storm. Divergent cyclonic flow field (Fig. 6) was observed in the mid-levels through the storm summit. This pattern was maintained until the storm summit began to contract at 21:21:40 CST.

The growth and decay noted in the mid levels of the storm is depicted by the areal distribution of the 40 dBZ fields and areal pattern of divergence fields (Figs. 50 and 51, respectively), for each elevation angle for each successive volume scan. Storm 5 exhibits marked decay aloft (Figs. 50 and 51) while transferring mass to the mid and lower levels.

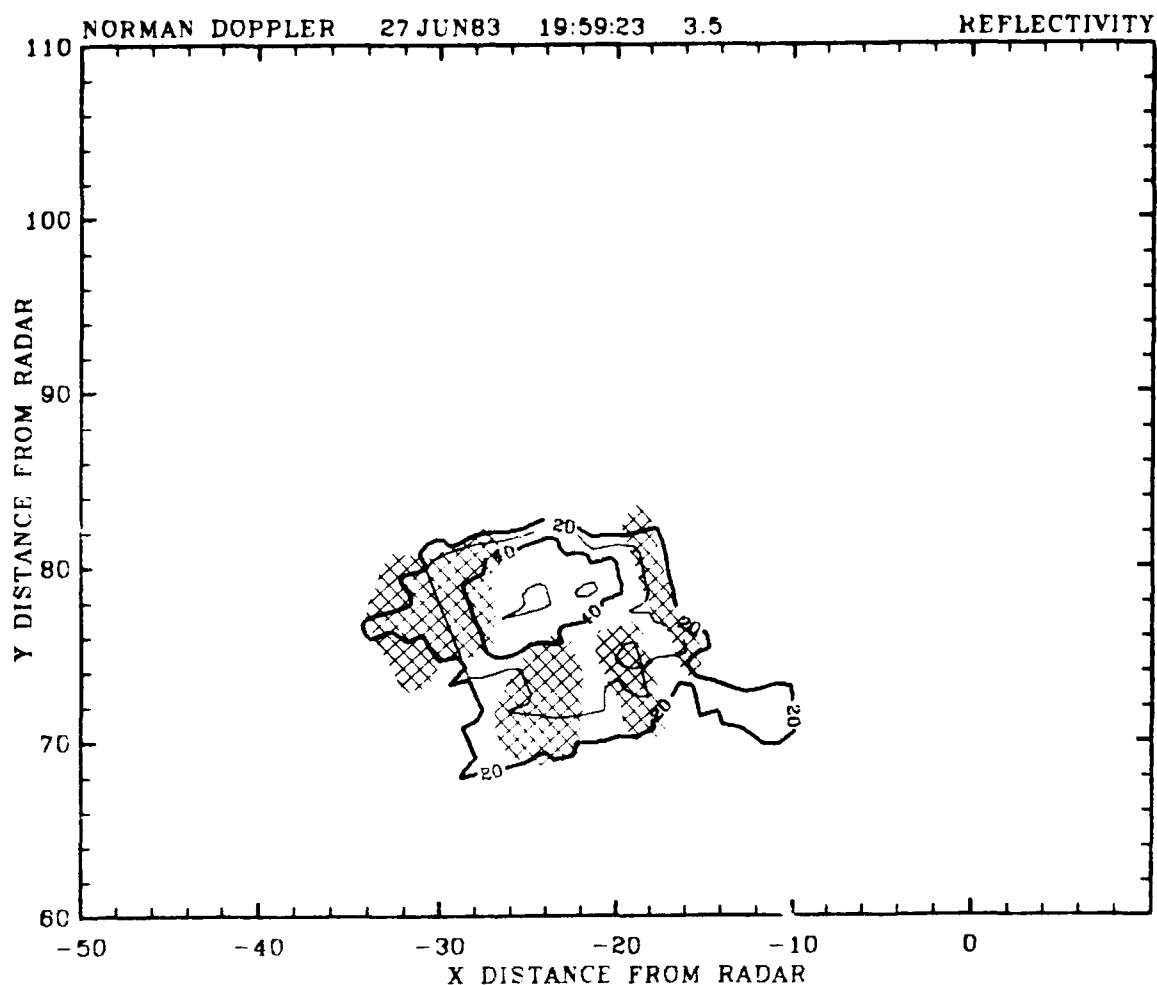
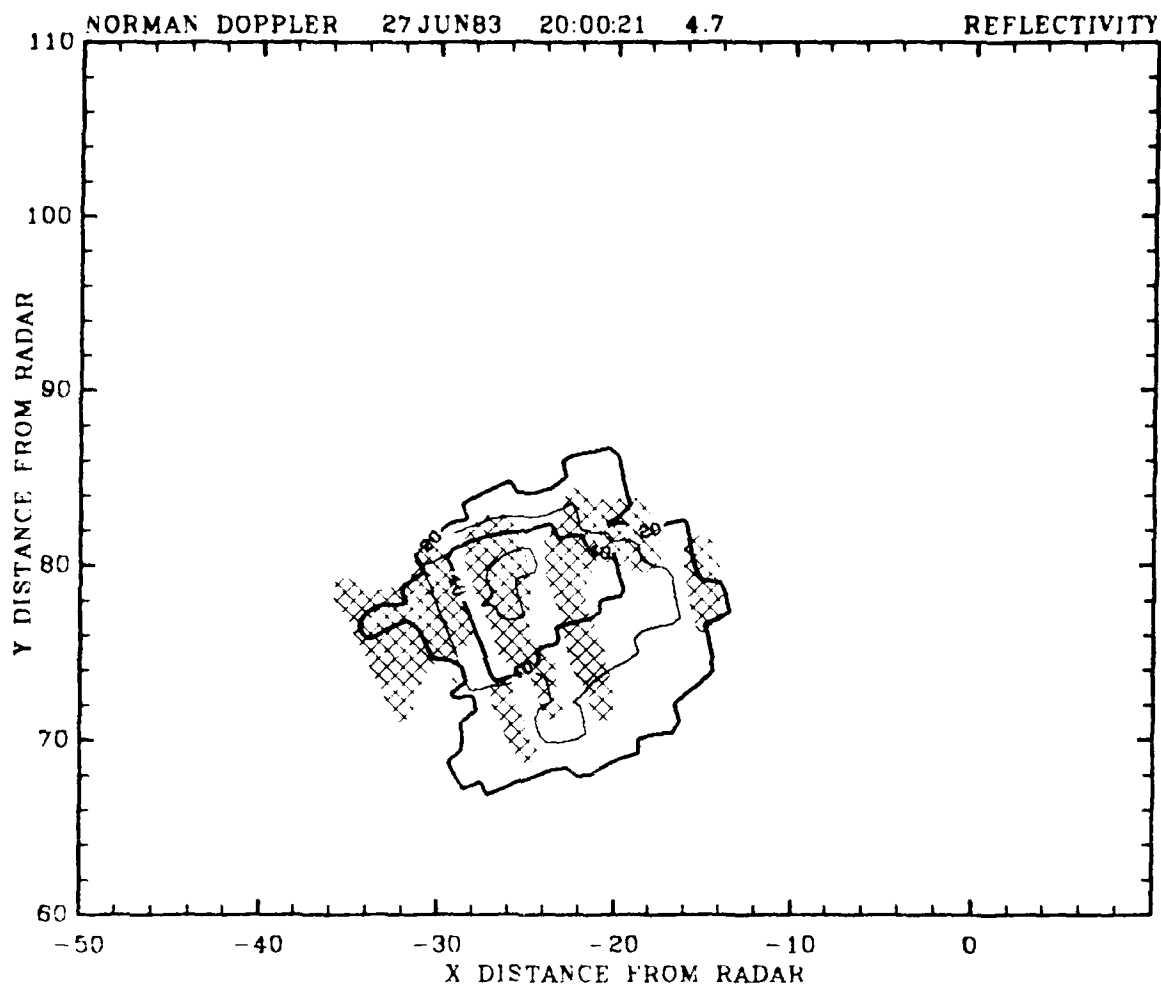


Fig. 38. Storm 5. Composite of reflectivity (contours) and positive radial divergence (cross-hatch) for 19:59:23 CSI at 3.5 deg elevation. Divergence determined using storm algorithm.



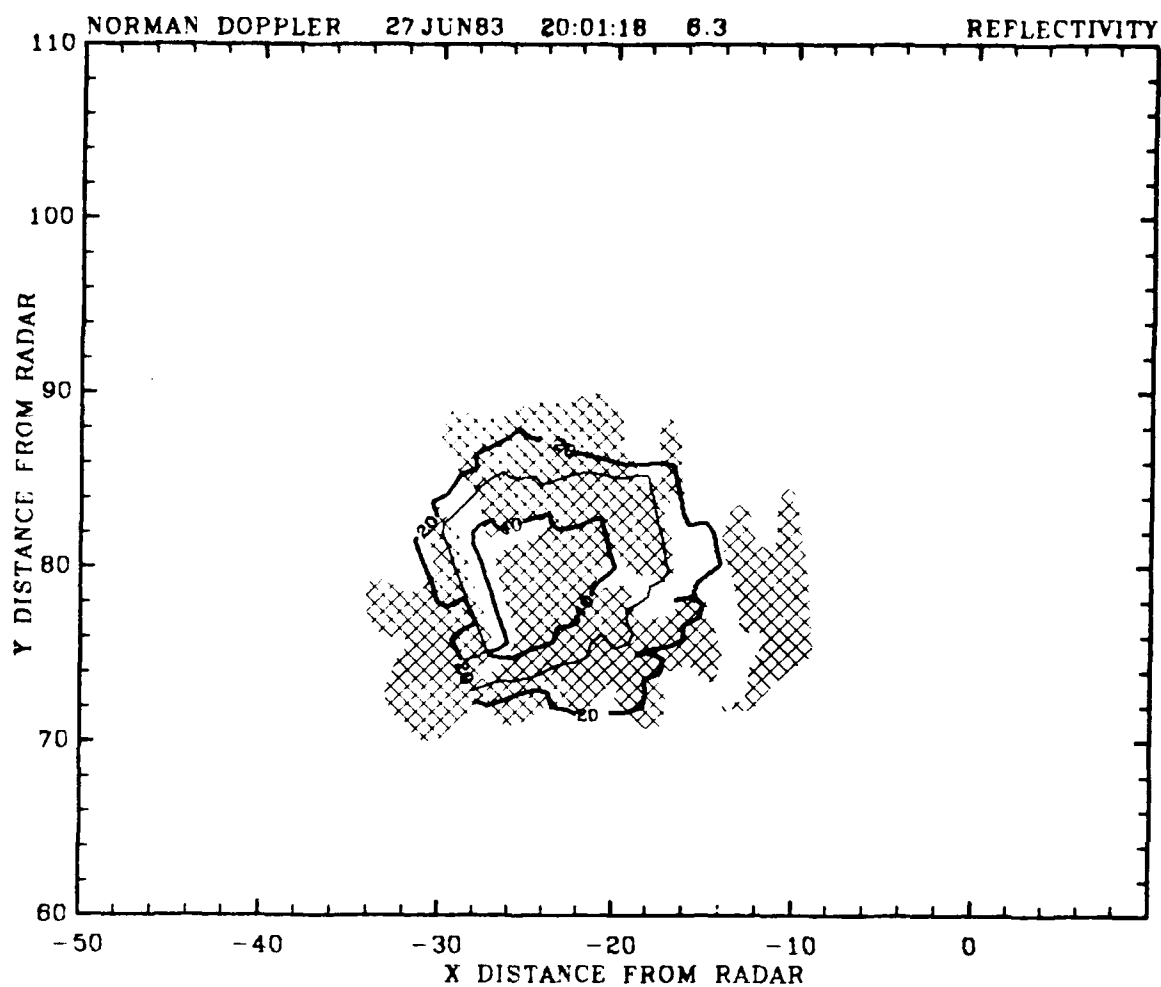


Fig. 40. As in Fig. 38, except for 20:01:18 CST at 6.3 deg elevation.

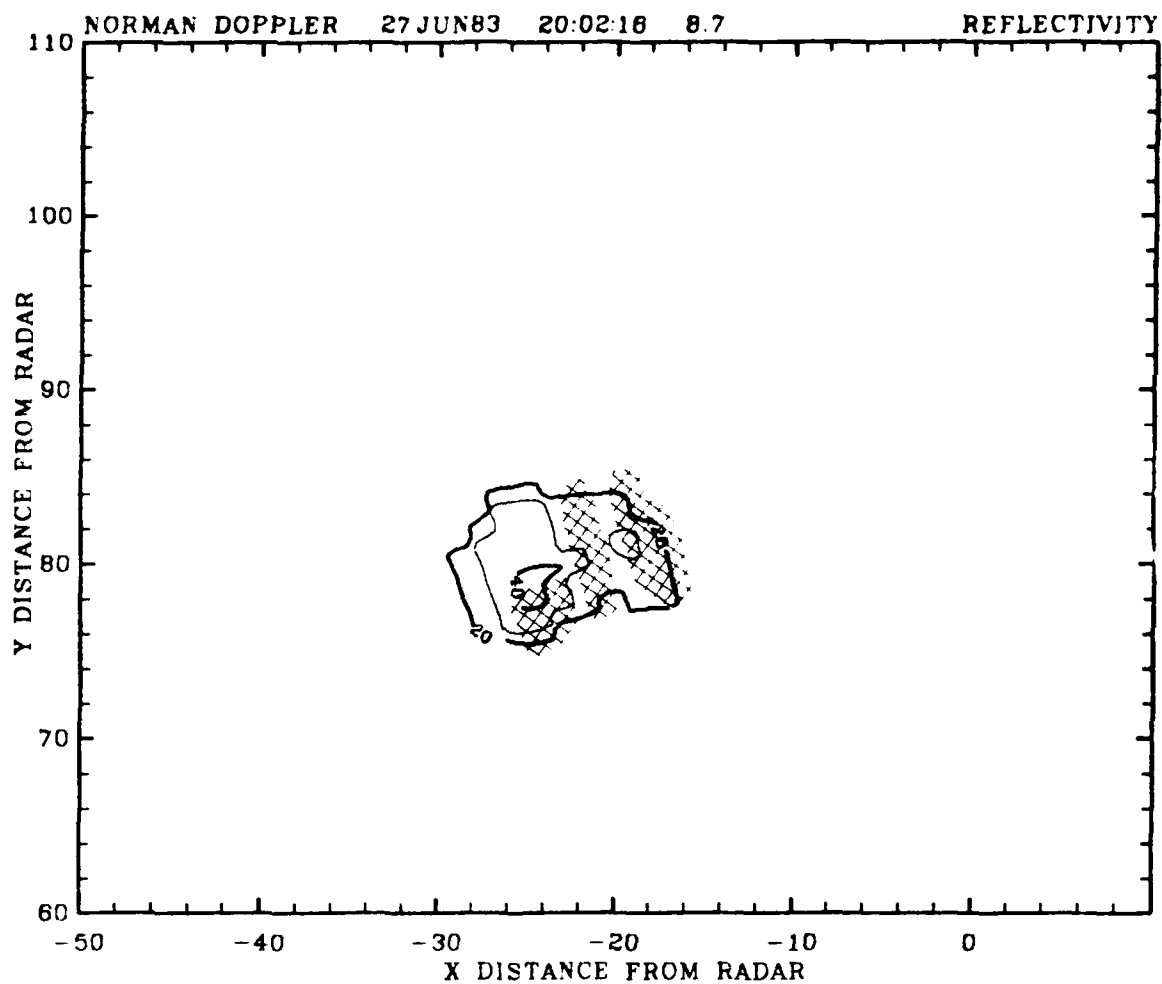


Fig. 41. As in Fig. 38, except for 20:02:16 CST at 8.7 deg elevation.

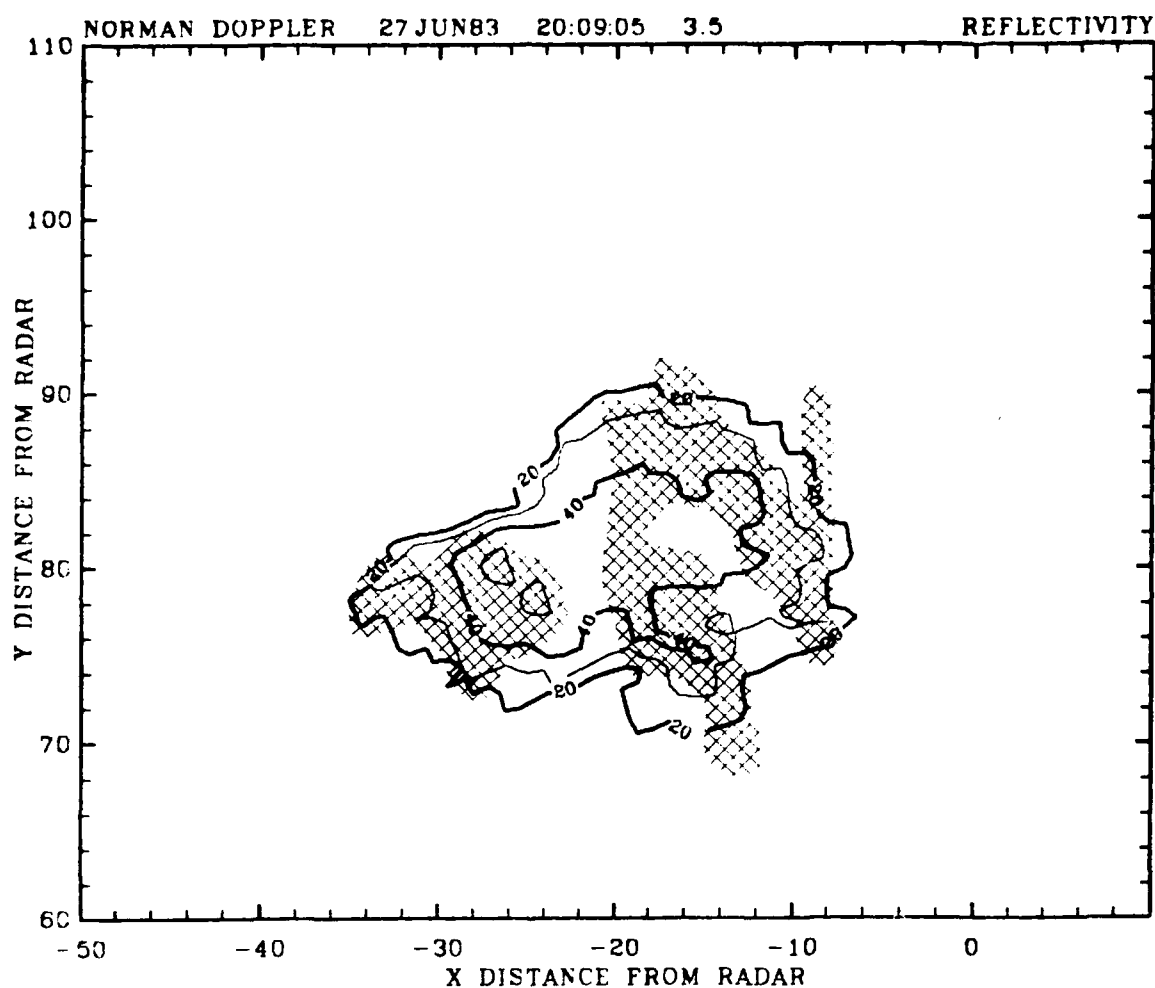


Fig. 42. As in Fig. 38, except for 20:09:05 CST at 3.5 deg elevation.

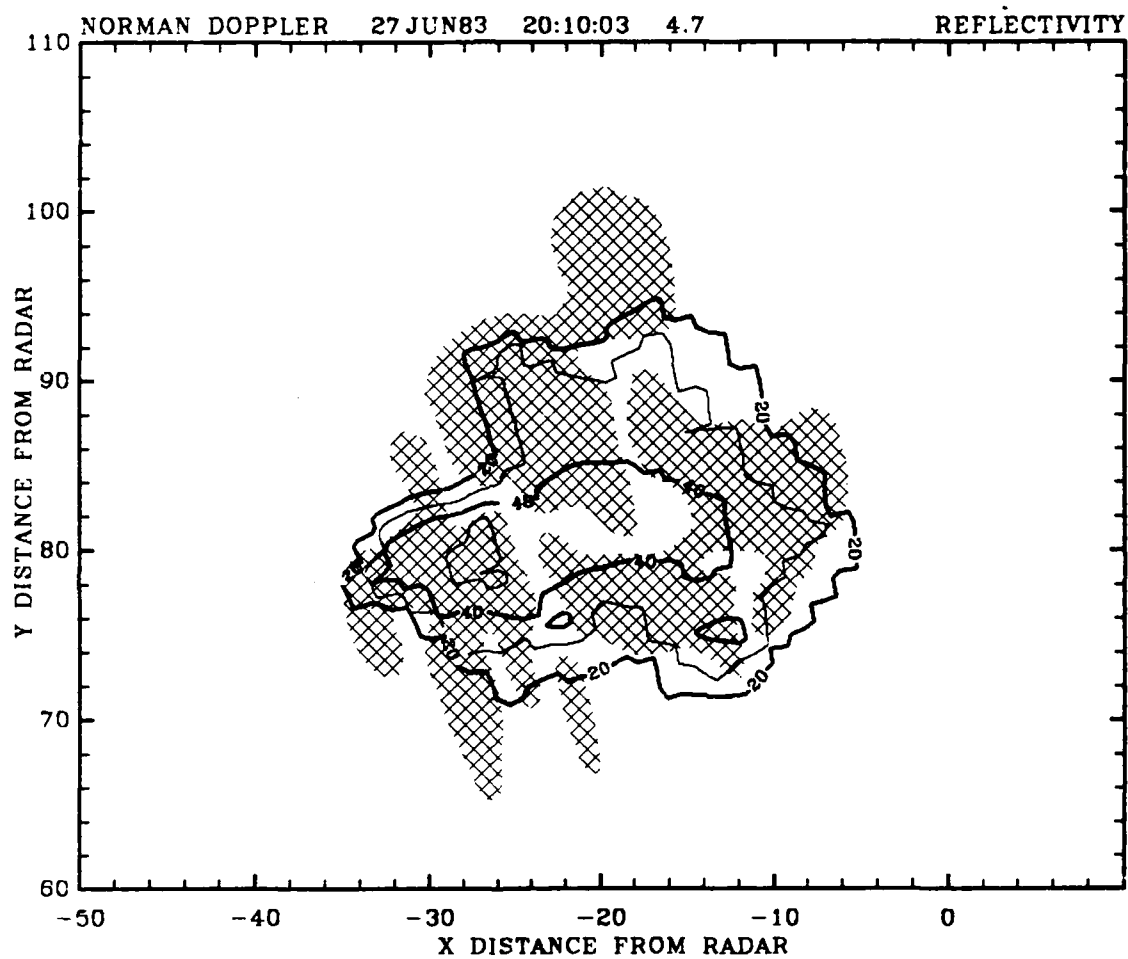


Fig. 43. As in Fig. 38, except for 20:10:03 CST at 4.7 deg elevation.

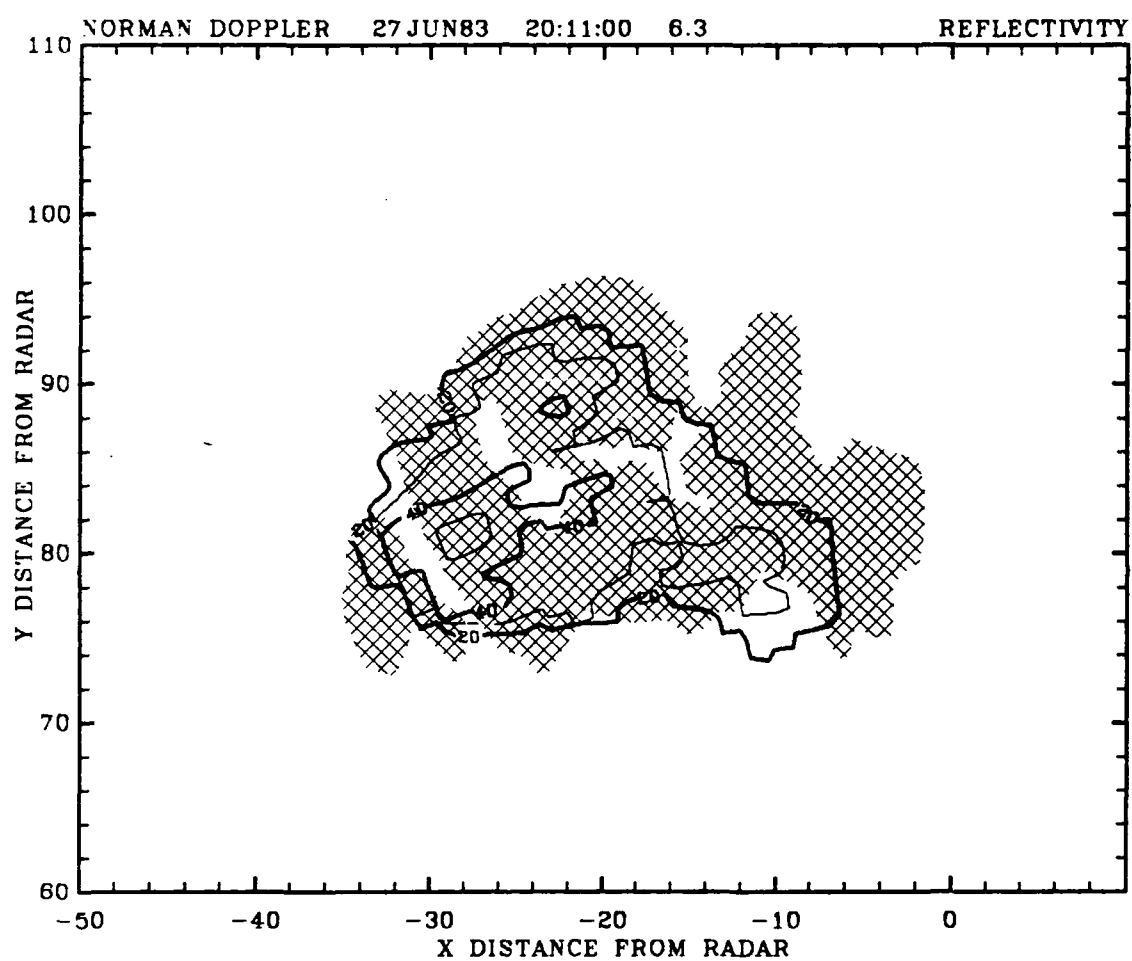


Fig. 44. As in Fig. 38, except for 20:11:00 CST at 6.3 deg elevation.

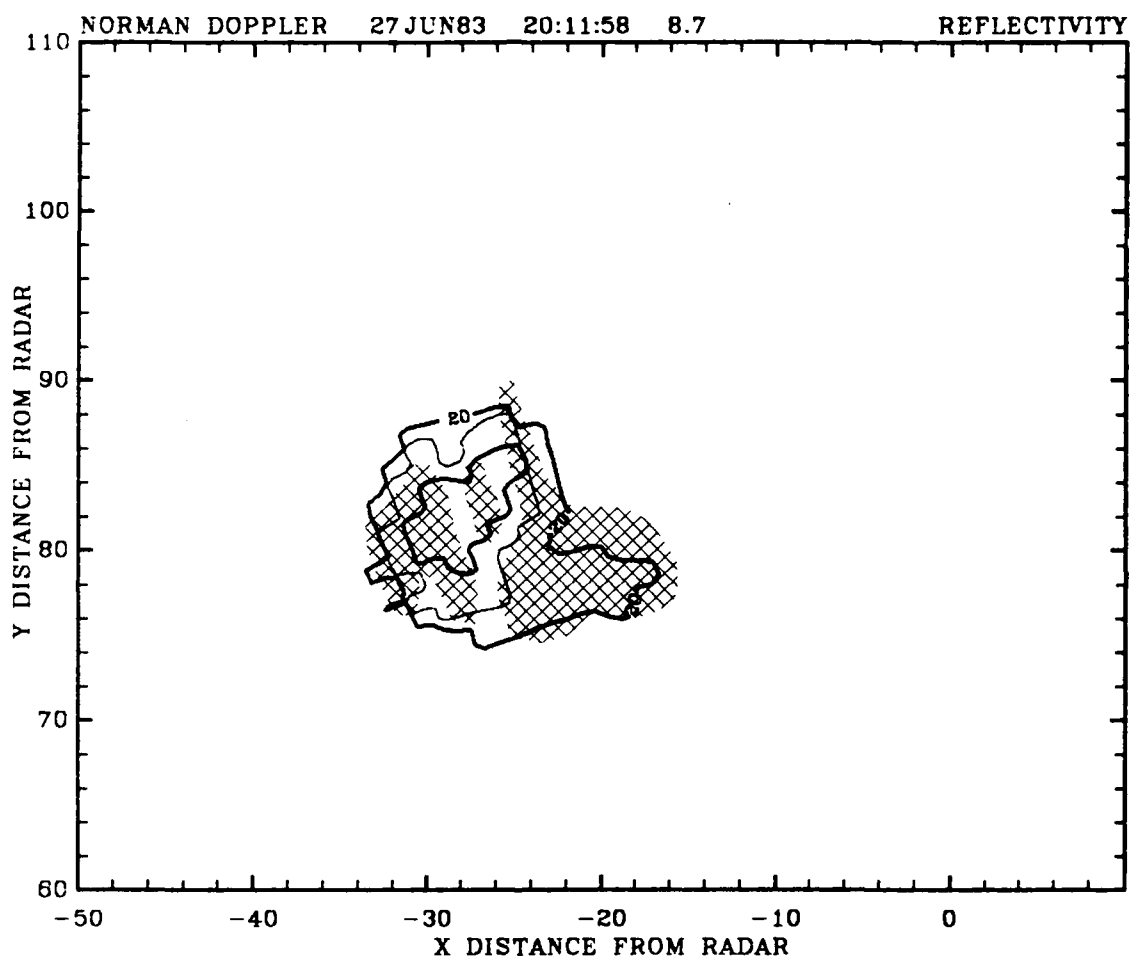


Fig. 45. As in Fig. 38, except for 20:11:58 CST at 8.7 deg elevation.

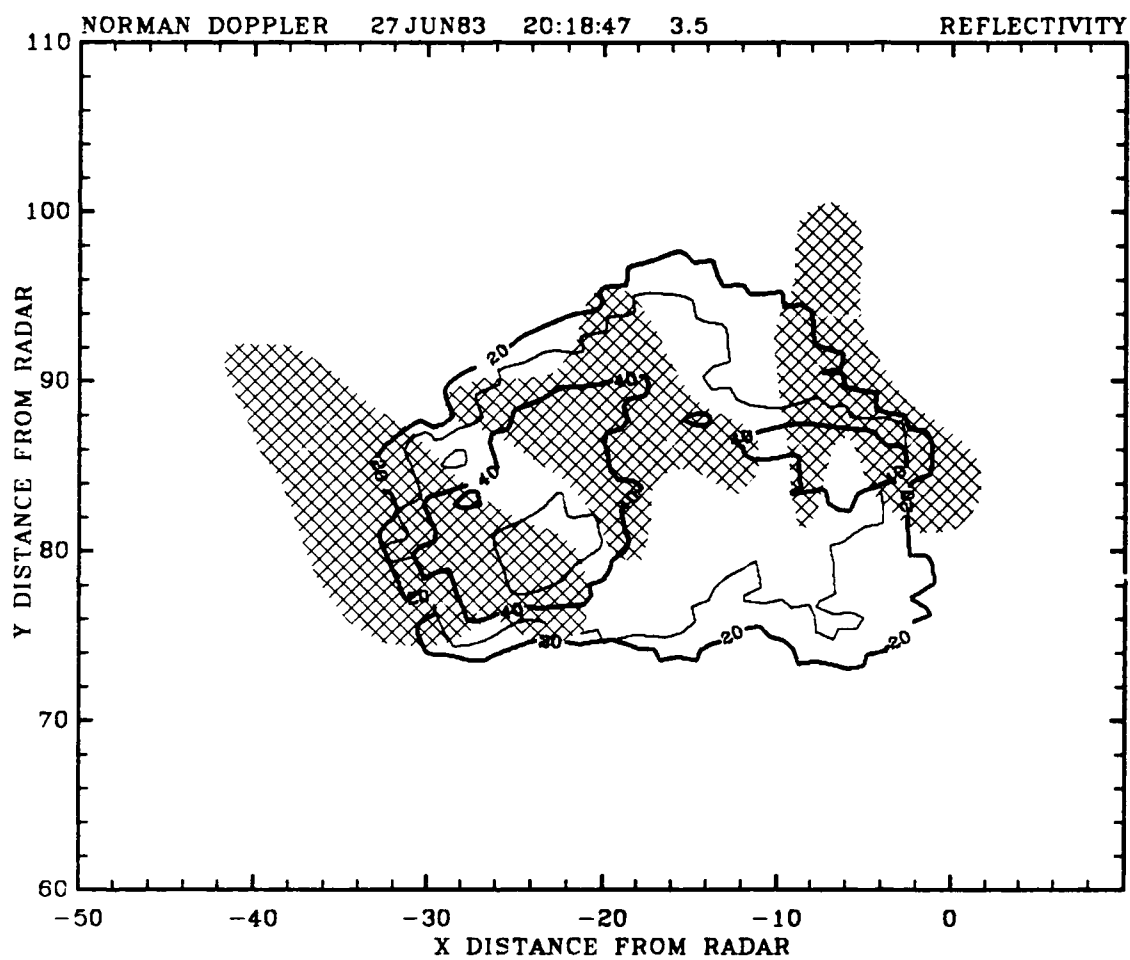


Fig. 46. As in Fig. 38, except for 20:18:47 CST at 3.5 deg elevation.

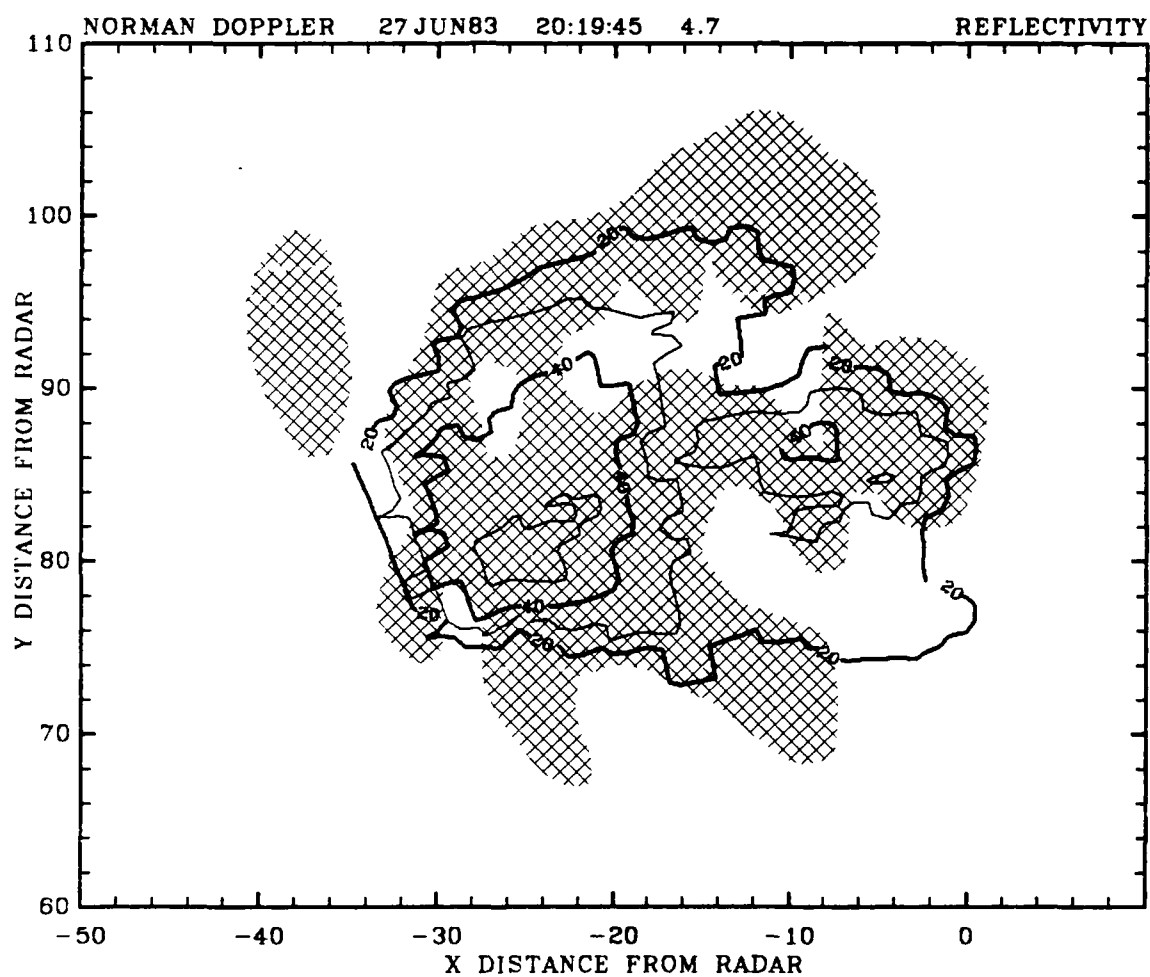


Fig. 47. As in Fig. 38, except for 20:19:45 CST at 4.7 deg elevation.

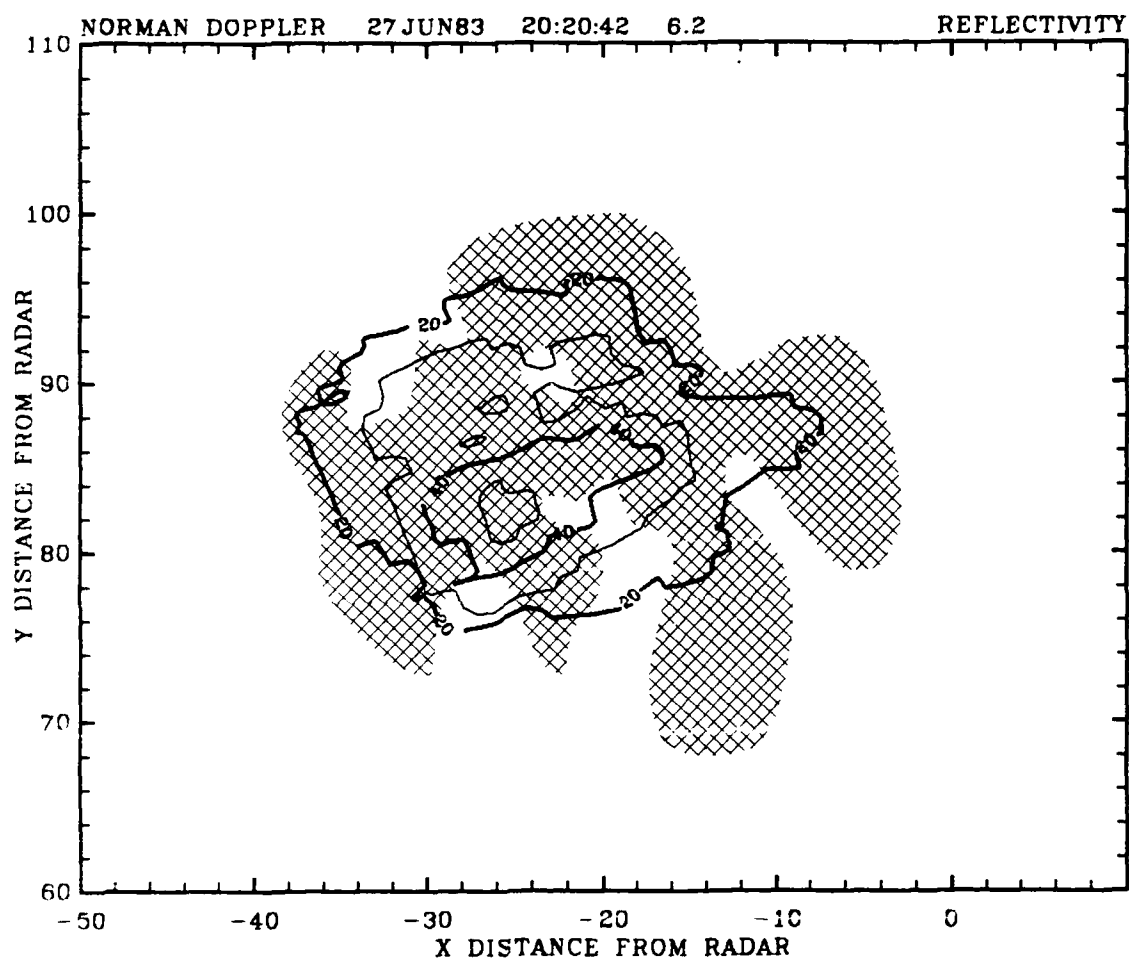


Fig. 48. As in Fig. 38, except for 20:20:42 CST at 6.2 deg elevation.

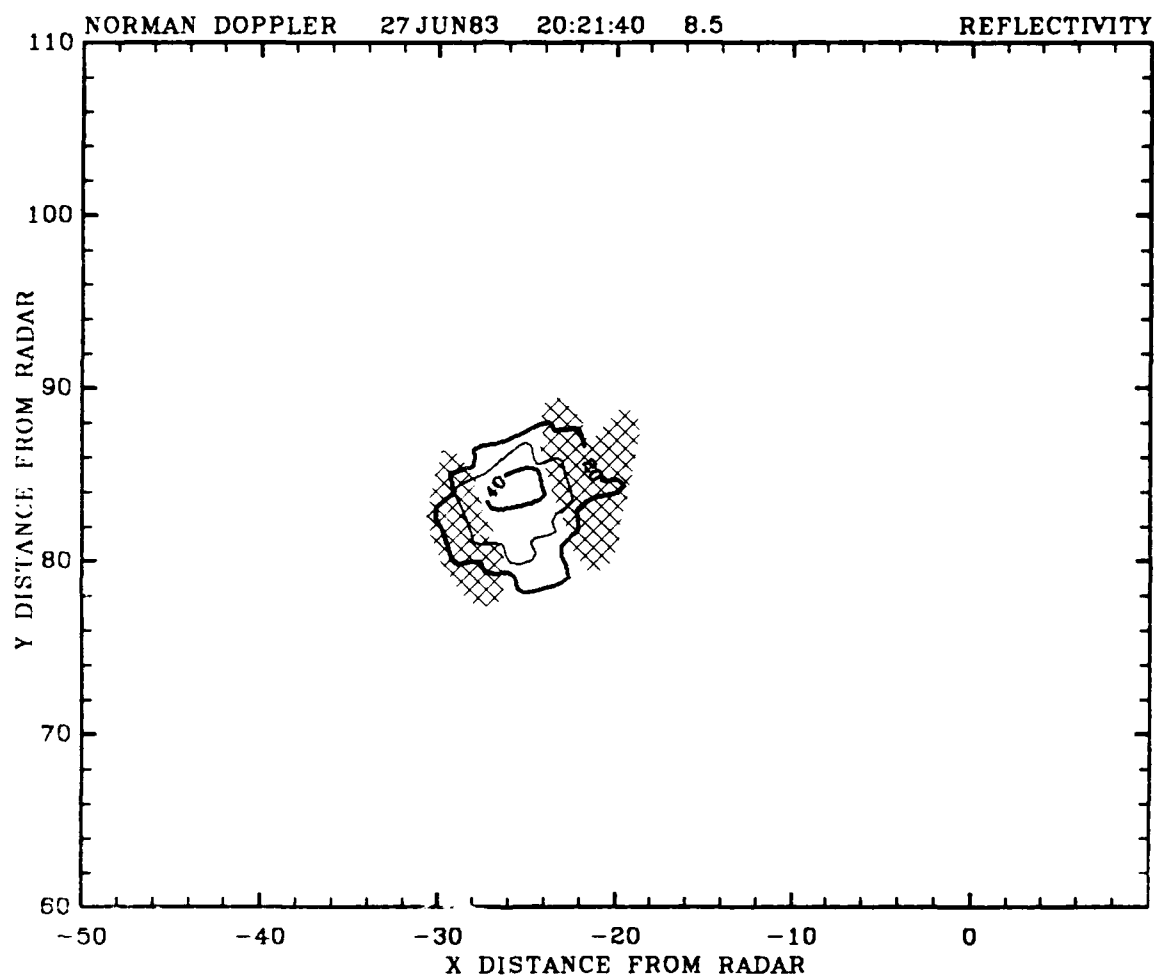


Fig. 49. As in Fig. 38, except for 20:21:40 CST at 8.5 deg elevation.

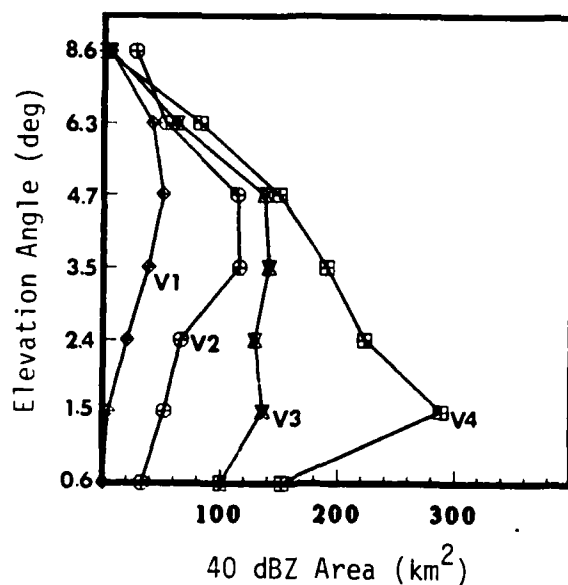


Fig. 50. Distribution of the area enclosed by the 40 dBZ contour during four successive volume scans (V1, V2, V3, and V4) for Storm 5.

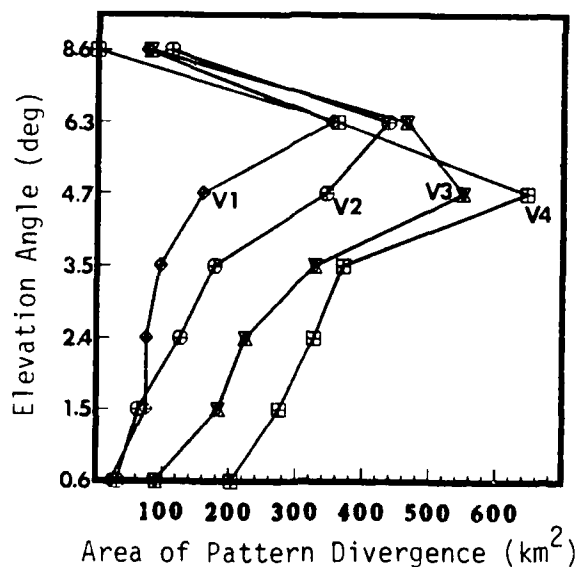


Fig. 51. Derived area radial divergence during four successive volume scans (V1, V2, V3, and V4) for Storm 5.

Consistent with Figs. 50 and 51, calculated divergence in Fig. 52 depicts good divergence at storm summit during V1 to V2 and convergence during V2 to V3 and V3 to V4, as the storm begins to decay. The mid levels show a slight weakening of divergence indicating a tendency for convergence at this level also; the low levels (1.5 and 0.6 deg elevation) exhibit marked divergence with storm outflow during V2 to V3 followed by somewhat weaker divergence during V3 to V4.

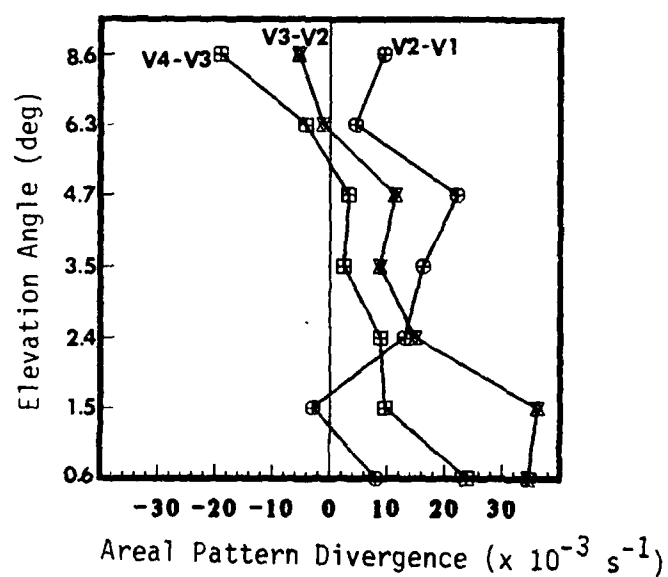


Fig. 52. Calculated divergence from the changes in the area of divergence shown in Fig. 51. Each level corresponds to the elevation angle.

CHAPTER VI

STATISTICAL ANALYSIS

Introduction

Of the over 20 parameters generated by the storm divergence algorithm, 11 were selected (Table 5) to be considered as candidate predictors. Once the data were tested for normality to ensure that statistical inference was valid, a multiple linear regression analysis method was applied for use forecasting strong low-level storm outflow events. The Texas A&M University Statistical Analysis System (SAS) package was used to aid in accomplishing the statistical analysis.

This chapter presents a brief overview of the regression models suggested by applying a statistical approach to select variables, regression models selected from using meteorological reasoning to select variables, and concludes with low-level storm outflow predictions using select regression models.

Variables Selected by Statistical Methods

The goal was to find a regression model that used the fewest independent variables (obtained from the storm summit changes), without degrading the predictability of the dependent variable (the strong low-level outflow at the surface from the storm). Both stepwise (SAS

STEPWISE) and maximum R^2 regression analysis methods (SAS MAXR) were applied. Since both the MAXR and stepwise method suggested the same four-variable model, the discussion of statistically selected variables will be limited to the MAXR method.

The MAXR method was pursued because it offered the possibility to review the best one-variable model, the best two-variable model, the best three-variable model, and so forth. While the method is not guaranteed to always find the regression model with the highest R^2 (coefficient of determination), it affords a sound approach for selecting independent variables.

Table 9 contains the results of the multiple linear regression models suggested by the MAXR method. Only the first seven models are presented because the addition of more independent variables only improved the R^2 slightly. The mean square of the error (MSE) and the Mallow's C_p statistic suggested limiting the regression model to seven variables, as the MSE and Mallow's C_p statistic approached a minimum and begin to increase as additional variables were added to successive models.

For each MAXR regression model (Table 9) the F-test was significant, rejecting hypotheses that all the coefficients were equal to zero. Adding AVGV (average velocity difference of pattern elements) to the two-variable model, only improved the R^2 by 0.019. However, when TDIV (total radial divergence of pattern elements) is added to the three-variable model, the R^2 improves to 0.79. The five-variable model adds DIV (divergence of areal pattern) to the four-variable model,

Table 9. Models suggested by the Maximum R^2 method. The independent variables are tabled below, the dependent variable is the low-level storm outflow.

Number of Variables	Variable	Parameter Estimates	Cp	MSE	F	Prob>F	R^2
1	AREF	-0.2398	58.63	18.08	11.608	0.0052	0.492
2	AREF HGT	-0.2131 1.1238	30.36	11.03	13.858	0.0010	0.716
3	AREF HGT AVGV	-0.2139 1.1006 -0.5641	29.82	11.33	9.229	0.0031	0.735
4	AREF HGT AVGV TDIV	-0.2071 1.3640 -1.1466 0.0659	24.69	10.08	8.337	0.0043	0.788
5	DIV AREF HGT AVGD TDIV	-0.9067 -0.1927 1.7608 -5.6942 0.1503	21.61	9.33	7.548	0.0067	0.825
6	DIV AREF AFLX HGT ADIV TDIV	-0.6433 -0.1984 -0.7221 1.6908 -14.9139 0.1404	20.36	9.20	6.569	0.0129	0.849
7	AREF AFLX ADIV AVGF HGT TDIV TFLX	-0.1769 -1.3388 -16.5866 0.5746 1.7449 0.2386 -0.0091	19.52	9.23	5.748	0.0245	0.870

improving R^2 to 0.83. The six-variable model improves R^2 a bit more to 0.85. Finally, the seven-variable model improves the R^2 to 0.87.

Thus, as a consequence of the multiple linear regression analysis, adding more variables improves the predictability of the dependent variable (non-tornadic thunderstorm low-level outflow), but only slightly after the four-variable model. It appears that the four- or five-variable regression model will do the job and if computing time is important, a three-variable model might be adequate in most cases.

Variables Selected by Meteorological Reasoning

Since the thrust of this study was to develop and implement a method to use the storm summit variables to infer low-level outflow, the DIV variable was hoped to demonstrate a large contribution to the regression model in which it was included. Consequently, the meteorological reasoning (MET) regression models are based on the prioritized order of importance of the independent variables calculated by the algorithm and are composed of those variables that appear in Table 5. The DIV, AREF, and HGT variables were anticipated to contribute the most information, followed by MWF (flux of areal pattern), AFLX (average flux of areal pattern), ADIV, and TFLX (total radial flux of pattern elements). Thus, these seven independent variables were hoped to provide most of the information necessary for prediction of low-level storm outflow.

Table 10 outlines the various two- to seven-variable MET regression models selected. F-tests for the three- to six-variable MET regression models were significant, while the two- and seven-variable MET regression model were just at and slightly above the preselected significance level of 0.10. The two-variable regression model performed poorly with an R^2 of 0.34. The three-variable regression model (MET3) shows improvement, with an R^2 of 0.72. In fact, a comparison of MET3 to the two-variable MAXR regression model (MAXR2) in Table 9 indicated only a very small difference (0.001) in R^2 . The four-variable regression model (MET4) is equally disappointing, as are the remaining five- through seven-variable MET regression models. One cannot, however, expect all models to produce worthwhile results. There would not be a challenge if all things worked as planned. At times there appears to be nothing that produces results as one wishes.

Table 10. Models suggested by meteorological reasoning. The independent variables are tabled below, the dependent variable is the low-level storm outflow.

Number of Variables	Variable	Parameter Estimates	F	Prob>F	R ²
2	DIV HGT	0.1771 1.3901	2.849	0.1007	0.341
3	DIV AREF HGT	0.0719 -0.2126 1.1362	8.424	0.0043	0.717
4	DIV AREF MWF HGT	0.0729 -0.2143 0.0057 1.1741	5.805	0.0137	0.721
5	DIV AREF MWF ADIV HGT	-0.1138 -0.2142 0.0091 -3.6752 1.2034	4.371	0.0324	0.732
6	DIV AREF MWF AFLX ADIV HGT	0.0800 -0.2176 0.0070 -0.4668 -1.6764 1.1417	3.367	0.0687	0.743
7	DIV AREF MWF AFLX ADIV HGT TFLX	0.0051 -0.2162 0.0015 -0.8968 -1.9650 1.3878 0.0041	2.717	0.1221	0.760

Low-level Storm Outflow Predictions

Using the various multiple linear regression models in Tables 9 and 10, descriptive tables were developed to show the MAXR and MET regression models' success at low-level storm outflow prediction (Tables 11 and 12, respectively). Each table indicates the independent variables used and scores the hits verses misses for the training data (Table 2) and the prediction and verification data (Table 3).

Table 13 consolidates all the low-level storm outflow predictions for each storm using different variable regression models. The "OBS WIND" column contains the peak wind speed detected by the SAM network or contains a "--," which indicates peak wind speeds were not available and it was one the storms entered for classification (Table 4).

Table 13. Low-level storm outflow predictions using different variable models displayed in Tables 11 and 12.

STORM	OBS WIND	MAXR MODELS							MET MODELS						
		1	2	3	4	5	6	7	2	3	4	5	6	7	
1	27	25.2	26.4	25.9	25.5	25.9	25.3	25.9	26.0	26.3	26.3	26.1	25.8	24.5	
2	28	23.9	25.2	24.7	26.1	26.8	27.4	27.3	26.3	25.2	24.5	23.7	24.2	24.9	
3	36	35.9	35.2	35.1	34.6	33.7	33.4	34.1	25.5	35.2	35.4	35.3	35.4	35.0	
4	28	27.5	30.7	31.7	29.0	29.3	30.4	29.2	28.9	30.7	30.0	31.1	31.4	31.5	
5	--	29.0	33.9	32.0	31.6	29.8	31.8	34.3	31.2	33.9	33.8	32.7	32.1	32.7	
6	--	17.1	20.0	17.4	16.9	19.3	21.2	28.9	27.5	20.1	20.3	19.8	19.2	19.8	
7	(26)	35.5	35.5	37.2	36.5	40.1	37.8	31.2	24.5	34.8	34.6	36.2	35.6	28.6	
8	--	23.9	24.4	24.3	25.3	27.2	26.5	29.5	25.2	24.4	24.8	25.0	24.7	24.4	
9	32	23.9	23.5	24.9	25.9	27.4	28.1	29.4	24.2	23.5	23.8	24.9	25.4	26.3	
10	(23)	31.5	32.4	31.5	31.5	30.8	33.3	41.2	27.0	32.5	33.1	33.0	33.5	31.0	
11	--	35.3	37.2	37.8	35.5	31.5	32.2	41.0	28.2	37.0	37.4	37.8	38.0	28.5	
12	20	27.7	24.3	24.4	24.7	25.8	25.0	24.4	20.9	24.2	24.3	24.4	24.4	24.9	
13	(21)	23.9	19.2	18.5	18.2	20.6	20.1	23.8	18.6	19.0	19.1	19.4	18.6	18.6	
14	19	23.9	19.2	18.7	19.0	17.3	18.7	20.4	19.1	19.3	19.4	18.9	18.9	19.5	
15	21	23.4	22.2	22.6	22.4	22.8	20.7	20.7	23.6	22.4	22.0	22.2	20.9	20.3	
16	18	18.4	19.6	20.4	19.4	18.4	18.0	18.0	25.6	19.7	20.1	20.7	20.6	20.5	
17	24	23.9	22.1	21.9	22.9	24.7	24.7	21.4	22.0	21.9	22.1	22.3	21.9	21.8	
18	17	20.4	18.8	18.6	17.3	16.7	16.8	18.1	21.8	18.7	18.5	18.3	19.1	17.8	
19	--	23.9	21.6	21.4	22.2	21.1	22.0	23.9	22.8	21.7	21.7	21.1	21.8	22.4	
20	20	22.7	20.9	20.5	20.4	19.2	19.6	18.4	22.3	20.9	20.9	20.5	21.1	21.4	
21	29	25.5	29.6	30.2	33.0	30.7	31.5	32.1	30.4	29.9	30.4	29.9	30.4	29.9	
22	(31)	23.9	26.2	25.8	26.3	27.9	28.4	28.3	27.1	26.1	26.2	26.4	26.2	26.5	
23	27	23.9	28.2	26.4	26.0	27.3	26.2	26.6	29.4	28.0	28.2	28.5	26.7	27.9	
24	(36)	26.2	27.7	27.5	28.9	27.9	34.2	35.0	27.1	27.8	28.1	24.7	29.4	32.2	

CHAPTER VII

CONCLUSIONS AND RECOMMENDATIONS

Conclusions

The objective of this research was to study the changes of non-tornadic thunderstorm summits, improve the predictability of low-level storm outflow (i.e., onset and intensity), and, especially, to determine when a non-tornadic thunderstorm will produce a severe downdraft. To reach this objective, it was hypothesized that early signatures exist in the structures of the upper-level, single-Doppler reflectivity and velocity fields that indicate the development of a severe downdraft in non-tornadic storms. It was believed that subtle differences exist in a non-tornadic thunderstorm and that these differences are important in classifying storm intensity. This hypothesis was evaluated using a case study approach in order obtain a qualitative view of storm severity and statistical methods employing multiple linear regression to determine the best possible variables for predicting low-level storm outflow using only the changes in the storm summit.

This research used a modified version of the storm summit divergence algorithm developed by Sickler et al. (1985b). These variables were examined by applying meteorological reasoning and statistical inference. This research demonstrated that subtle

differences exist in single-Doppler derived parameters within a storm and that the observable changes in the storm summit provide adequate information to determine the potential of severe low-level outflow situations.

While meteorological reasoning suggested some select variables might perform best (Tables 10 and 11), the inferences gained from an examination of the statistical analysis allowed a quantitative estimate of the contribution of the variables in each model. Results of the maximum R^2 (MAXR) method, which disregarded the meteorology and looked objectively at the sample, pointed out combinations of variables that would produce the best models, from a one-variable to a full-variable regression model.

This examination determined that the regression model used to predict low-level outflow cannot be limited to a one- or two-variable model. If either or both variables were not measureable, or did not indicate a representative change, a potential low-level outflow situation could be missed. For example, several storms in this study (see Table 16) did not have either a 40 dBZ change or any detectable reflectivity above 40 dBZ during the time step (i.e., from V1 to V2). In any event, for some situations, a single-variable regression model will be unreliable. Consequently, based on this study, the regression model should include a minimum of three variables. That, however, does not mean a full-variable model could not be used. Therefore, multiple linear regression models found to predict best the low-level outflow events were MET3, MAXR3, MAXR4, and MAXR5 (Tables 11 and 12).

The tabulated data in Chapter VI implies that the DIV (divergence of the areal pattern) variable offered little statistical significance. However, the review of over 30 storms and the details of three storms presented in this study, clearly demonstrated the significance of the radial divergence field. Thus, the DIV variable cannot be dismissed solely on the statistical inferences concluded from this limited sample. The locations of the areal pattern of radial divergence were in preferred areas, usually about the core of the storm and over the storm summit. Also, there was a consistency in the vertical, where the radial divergence patterns were aligned. Further, some of these storms were observed to pulsate, allowing one to conclude that some non-tornadic storms will strengthen, begin to weaken, and then strengthen again. This was confirmed by the secondary strong surface gusts (surges) during some storms, while others produced multiple surges of wind gusts at the surface. Perhaps a different handling of the data may improve the utility of DIV.

The storm divergence algorithm performs best in the upper levels of the storm and on isolated storms or storms that can be isolated by data suppression, threshold techniques, or some other method of partitioning. Recall how Storm 5 demonstrated changes (Figs. 50 and 51) that were consistent with storm theory. On the other hand, Storm 10 was incorrectly forecast as severe in every model (Table 13), while the observed surface winds were 23 m s^{-1} . Compared to other non-severe non-tornadic storms with similar outflows ($21\text{-}24 \text{ m s}^{-1}$), the parameters calculated for Storm 10 were more consistent with the stronger storms.

Based on this information, one can conclude that the strongest surface wind was not intercepted (recorded) by the SAM complex. Due to sampling limitations, this is possible for recorded surface winds for all storms. This variation was clearly noted by the variations recorded at a SAM complex (Figs. 12, 23, and 24).

This study used data recorded during the springtime (April to June 1983) in Central Oklahoma. Because spring thunderstorm activity is historically more severe across Oklahoma, any coefficients determined for models in this study should only be applied to storms occurring during the same time of year. This implies that the coefficients may have seasonal and geographical dependence and will require testing to demonstrate otherwise. Accordingly, it is anticipated that this study will provide a good seed for application and further development into the NEXRAD system. Integration of these studies into the NEXRAD system should provide a sound basis for deciding if a non-tornadic storm has the potential to develop severe, low-level outflow.

Recommendations

This research has demonstrated the need to continue single-Doppler investigations of the reflectivity and radial velocity fields of non-tornadic storms to improve the divergence algorithm to predict strong low-level storm outflow. The storm divergence algorithm should be tested against another similar data set (springtime over Central Oklahoma), preferably with the same time step (approximately 10

minutes) to see if results are the same. This will provide insights with respect to seasonal dependence of coefficients. Similarly, other statistical approaches should be explored to infer strong surface wind events.

Additional examinations are needed to inspect closely the radial divergence patterns and conduct further testing to tighten the reflectivity suppression thresholds from 10 to 30 dBZ, and perhaps to 40 dBZ, to capture a more symmetric outflow about the storm core. This will add a measure of consistency to comparisons that may provide more positive results than discovered by this study. Once this has been done, the divergence of the areal pattern (DIV) variable may yield more conclusive results to improve the regression model. Also, because the flux variables appear to be but a reflection of the divergence variables, future tests should carefully consider their utility.

Because the 40 dBZ reflectivity element areal field (AREF) contributed so significantly in the regressions, other ways to introduce the reflectivity field changes should be explored, as should the potential application of this method using the AREF and beam center areal pattern height fields (HGT) to conventional weather radar for similar low-level strong wind forecasting.

Finally, just as the 10 minute volume scan update rate provided positive results in this research, shorter volume scan intervals must be investigated because the operational NEXRAD will provide volume scan updates over intervals as short as every 5 minutes. This is needed before application of this technique to the NEXRAD algorithm inventory.

REFERENCES

- Adler, R. F., and D. D. Fenn, 1979: Thunderstorm intensity as determined from satellite data. J. Appl. Meteor., 18, 502-517.
- Atkinson, B. W., 1981: Meso-Scale Atmospheric Circulations. Academic Press, New York, 495 pp.
- Atlas, D., 1964: Advances in radar meteorology. Advances in Geophysics, 10, 318-478.
- Auer, A. H., D. L. Veal, and J. D. Marwitz, 1969: Updraft deterioration below cloud base. Sixth Conf. on Severe Local Storms, Chicago, Amer. Meteor. Soc., 16-19.
- Barnes, S. L., 1976: Severe local storms: Concepts and understanding. Bull. Amer. Soc., 57, 412-419.
- _____, 1978: Oklahoma thunderstorm on 29-30 April 1970. Part I: Morphology of a tornadic storm. Mon. Wea. Rev., 106, 673-684.
- _____, 1980: Report on a meeting to establish a common Doppler radar data exchange format. Bull. Amer. Meteor. Soc., 61, 1401-1404.
- Bonewitz, J. D., 1978: Development of Doppler radar techniques for severe thunderstorm wind advisories. M.S. Thesis, University of Oklahoma, 69 pp.
- _____, 1984: Personal communication.
- _____, 1986: Surface wind fields in the vicinity of meso-convective storms as derived from radar observations: non-tornadic storms. Ph.D. Dissertation, Texas A&M Univ., 157 pp.
- Brandes, E.A., 1977: Flow in severe thunderstorms observed by dual-Doppler radar. Mon. Wea. Rev., 105, 113-120.
- Browning, K. A., 1962: Cellular structure of convective storms. Meteor. Mag., 91, 341-350.
- _____, and G. B. Foote, 1976: Airflow and hail growth in supercell storms and some implications for hail suppression. Quart. J. Roy. Meteor. Soc., 102, 499-534.
- Burgess, D. W., 1976: Single-Doppler radar vortex recognition: Part 1, mesocyclone signatures. 17th Conf. on Radar Meteor., Seattle, Amer. Meteor. Soc., 97-103.

Byers, H. R., and R. R. Braham, 1949: The Thunderstorm. U.S. Govt Printing Office, Washington D.C., 287 pp.

Charba, J., 1972: Gravity current model applied to analysis of squall-line gust front. NOAA Tech. Memo. ERLTM-NSSL No. 61, National Severe Storms Laboratory, Norman, OK, 58 pp.

_____, and Y. Sasaki, 1971: Structure and movement of the severe thunderstorm of 3 April 1964 as revealed from radar and surface mesonet network data analysis. J. Meteor. Soc. Japan, 49, 191-213.

Chisholm, A. J., and J. H. Renick, 1972: The kinematics of multi-cell and supercell Alberta hailstorms. Alberta Research Studies Report 72-2, Alberta, Canada, 24-31.

Donaldson, R. J., Jr., 1967: Horizontal wind measurement by Doppler radar in a severe squall line. Fifth Conf. on Severe Local Storms, St. Louis, Amer. Meteor. Soc., 89-98.

_____, 1970: Vortex signature recognition by Doppler radar. J. Appl. Meteor., 9, 661-670.

_____, G. M. Armstrong, A. C. Chmela and M. J. Kraus, 1969: Doppler radar investigation of air flow and shear within severe thunderstorms. Proc. Sixth Conf. on Severe Local Storms, Boston, Amer. Meteor. Soc., 146-154.

Doswell, C. A. III., D. L. Kelly, and J. T. Schaefer, 1983: A preliminary climatology of non-tornadic severe thunderstorm events. Proc. Thirteenth Conf. on Severe Local Storms, Tulsa, Amer. Meteor. Soc., 25-32.

Doviak, R. J., and D. Sirmans, 1973: Reflectivity equation for NSSL's WDS-71 10 cm Doppler radar. Unpublished Report, NSSL, Norman, OK, 8 pp.

Eyster, R., 1985: Personal communication.

Fankhauser, J. C., 1971: Thunderstorm-environment interactions determined from aircraft and radar observations. Mon. Wea. Rev., 99, 171-192.

Fujita, T., 1981: Tornadoes and downbursts in the context of generalized planetary scales. J. Atmos. Sci., 38, 1511-1534.

Goff, R. C., 1975: Thunderstorm-outflow kinematics and dynamics. NOAA Tech. Memo. ERL-NSSL-75, National Severe Storms Laboratory, Norman, OK, 66 pp.

- _____, 1976: Vertical structure of thunderstorm outflows. Mon. Wea. Rev., 104, 66 pp.
- Hennington, L. D., and D. W. Burgess, 1981: Automatic recognition of mesocyclones from single-Doppler radar data. Proc. 20th Conf. on Radar Meteor., Boston, Amer. Meteor. Soc., 704-706.
- Heymfield, G. M., 1978: Kinematic and dynamic aspects of the Harrah tornadic storm analyzed from dual-Doppler radar data. Mon. Wea. Rev., 106, 233-254.
- _____, R. H. Blackmer, Jr., and S. Schatz, 1983: Upper-level structure of Oklahoma tornadic storms on 2 May 1979. I: Radar and satellite observations. J. Atmos. Sci., 40, 1740-1755.
- Istok, M., 1983: Personal communication.
- JAWS Staff, 1984: JAWS interim report for third year's effort (FY-84). JAWS NCAR Report No. 01-85, Boulder, CO, 14 pp.
- JDOP Staff, 1979: Final report on the Joint Doppler Operational Project (JDOP) 1976-1978. NOAA Tech. Memo., ERL-NSSL-86, Norman, OK, 84 pp.
- Klemp, J. B., R. B. Wilhelmson, and P. S. Ray, 1981: Observed and numerically simulated structure of a mature supercell thunderstorm, J. Atmos. Sci., 38, 1558-1580.
- Klingbe, D. L., 1985: A gust front case studies handbook. MIT Project Report DOT/FAA/PM-84/15, Lexington, MA, 122 pp.
- Koscielny, A. J., R. J. Doviak, and R. Rabin, 1982: Statistical consideration in the estimation of divergence from single-Doppler radar and application to prestorm boundary-layer observations. J. Appl. Meteor., 21, 197-210.
- Kropfli, R. A., and L. J. Miller, 1976: Kinematic structure and flux quantities in a convective storm from dual-Doppler radar observations. J. Atmos. Sci., 33, 520-529.
- Lemon, L. R., 1974: Interaction of two convective scales within a severe thunderstorm: A case study. NOAA Tech. Memo. ERLTM-NSL No. 71, National Severe Storms Laboratory. Norman, OK, 16 pp.
- _____, 1977: Severe thunderstorm radar identification techniques and warning criteria. NOAA Tech. Memo. NWS-NSSFC-1, National Severe Storms Forecast Center, Kansas City, MO, 60 pp.

- _____, and D. W. Burgess, 1980: Magnitude and implications of high speed outflow a severe storm summits. Proc. 19th Conf. on Radar Meteor., Boston Amer. Meteor. Soc., 364-368.
- _____, R. J. Donaldson Jr., D. W. Burgess, and R. A. Brown, 1977: Doppler radar applilcation to a severe thunderstorm study and potential real-time warning. Bull. Amer. Meteor. Soc., 58, 1187-1193.
- _____, and C. A. Doswell III, 1979: Severe thunderstorm evolution and mesocyclone structure as related to tornadogenesis. Mon., Wea. Rev., 107, 1184-1197.
- Lhermitte, R. M., 1964: Doppler radars as severe storm sensors. Bull. Amer. Meteor. Soc., 45, 587-596.
- _____, 1966: Application of pulse Doppler radar technique to meteorology. Bull. Amer. Meteor. Soc., 47, 703-711.
- _____, and D. Atlas, 1961: Precipitation motions by pulse Doppler radar. Proc. Ninth Wea. Conf., Boston, Amer. Meteor. Soc., 218-223.
- Ludlum, F. H., 1963: Severe local storms: A review. Meteor. Monogr., 5. 1-30.
- Mack, Robert A., D. F. Wylie, 1982: An estimation of the condensation rates in three severe storm systems from satellite observations of the convective mass flux. J. Appl. Meteor., 110, 725-744.
- Mack, R. A., A. F. Hasler, and F. F. Adler, 1983: Thunderstorm cloud top observations using satellite stereoscopy. Mon. Wea. Rev., 111, 1949-1964.
- Marwitz, J. D., 1972: The structure and motion of severe hailstorms, Part I. Supercell storms. J. Appl. Meteor., 11, 180-188.
- McCann, D. W., 1983: The enhanced-V: a satellite observable severe storm signature. Mon. Wea. Rev., 111, 887-894.
- Miller, R. C., 1972: Notes of the analysis and severe storm forecasting procedures of the Air Force Global Weather Central. Air Weather Service Technical Report 200, Scott AFB, IL, 102 pp.
- NEXRAD JSPO Staff, 1983: Plan for spring 1983 demonstration of prototype NEXRAD products in an operational environment. NEXRAD Report, Silver Spring, MD, 82 pp.
- _____, 1985: Next generation weather radar algorithm report. NEXRAD Report R400A-AR301, Silver Spring, MD, 890 ppp.

- Nelson, S. P., 1976: Characteristics of multi-cell and supercell hailstorms in Oklahoma. Proc. International Conf. on Cloud Physics, Boulder, 335-340.
- _____, 1977: Rear flank downdraft. A hailstorm intensification mechanism. Proc. Tenth Conf. on Severe Storms, Omaha, Amer. Meteor. Soc., 521-525.
- Roberts, R. D., and J. W. Wilson, 1984: Precipitation and kinematic structure of microburst producing storms. Proc. 22nd Conf. on Radar Meteor., Zurich, Amer. Meteor. Soc., 71-76.
- Schlesinger, R. E., 1978: A three-dimensional model of an isolated thunderstorm. Part I: Comparative experiments for variable ambient wind shear. J. Atmos. Sci., 35, 690-713.
- Scorer, R. S., and F. H. Ludlum, 1953: Bubble theory of penetrative convection. Quart. J. Roy. Meteor. Soc., 79, 94-103.
- Sickler, G. L., 1979: Convective rainfall estimation from GOES-1 infrared data. M.S. Thesis, Texas A&M Univ., 88 pp.
- _____, J. D. Bonewitz, and G. L. Huebner, 1985a: Horizontal and vertical structure of non-tornadic meso-beta scale convective complexes. Proc. 2nd Conf. on Mesoscale Process, University Park, Amer. Meteor. Soc., 29.
- _____, J. D. Bonewitz, and G. L. Huebner, 1985b: A study of non-tornadic thunderstorm fields detected during the NEXRAD Operational Test Facility's spring 1983 demonstration. Proc. 14th Conf. on Severe Local Storms, Indianapolis, Amer. Meteor. Soc., 236-239.
- _____, and G. L. Huebner, 1986: Outflow potential of non-tornadic storms inferred from single-Doppler radar. Proc. 23rd Conf. on Radar Meteor., Snowmass, Amer. Meteor. Soc., Unpublished.
- _____, and A. H. Thompson, 1980: Convective rainfall estimation from GOES-1 infrared data. Second Conf. on Flash Floods, Atlanta, Amer. Meteor. Soc., 109-114.
- Snapp, M. R., 1979: Investigation of the single-Doppler divergence signature as an objective severe hailstorm detection method. M.S. Thesis, Univ. of Oklahoma, 47 pp.
- Stommel, H., 1947: Entrainment of air into cumulus cloud. J. Meteor., 4, 91-94.
- Turner, J. S., 1964: The flow into an expanding spherical vortex. J. Fluid Mech., 18, 195-208.

Udeya, H., and D. S. Zrnic, 1986: Automatic detection of gust fronts. J. Atmos. Oceanic Tech., 3, 36-50.

Wakimoto, R. M., 1981: Investigations of thunderstorm gust fronts using Project NIMROD data. Ph.D. Thesis, Univ. of Chicago, 129 pp.

Wilk, K. E., L. R. Lemon, and D. W. Burgess, 1978: Interpretation of radar echoes from severe thunderstorms: A series of illustrations with extended captions. Unpublished Report, NSSL, Norman, OK, 75 pp.

Witt, A., and S. P. Nelson, 1984: The relationship between upper-level divergent outflow magnitude as measured by Doppler radar and hailstorm intensity. Proc. 22nd Conf. on Radar Meteor., Zurich, Amer. Meteor. Soc., 108-111.

Wood, V. T., and R. A. Brown, 1983: Single-Doppler velocity signatures: An atlas of patterns in clear air/widespread precipitation and convective storms. NOAA Tech. Memo., ERL-NSSL-95, Norman, OK, 71 pp.

_____, 1986: Single Doppler velocity signature interpretation of nondivergent environmental winds. J. Atmos. Oceanic Tech., 3, 114-128.

Woodward, B., 1959: The motion in and around isolated thermals. Quart. J. Roy. Meteor. Soc., 85, 144-155.

Ziegler, D., 1984: Daily meteorological summaries of the NEXRAD Interim Operational Test Facility spring 1983 demonstration. NEXRAD IOTF Report, unpublished, Norman, OK, 115 pp.

Zrnic, D. S., 1985: Personal communication.

_____, D. W. Burgess, and Y. Gal-Chen, 1983: Automatic detection of mesocyclonic shear test results. NEXRAD IOTF Final Report, unpublished, Norman, OK, 44 pp.

_____, L. D. Hennington, and J. Skelton, 1982: Automatic recognition of mesocyclones from single-Doppler radar data. Final Report, AFGL-TR-82-0291, Boston, MA, 42 pp.

_____, and Y. Gal-Chen, 1984: Divergence measurement in storm tops. CIMMS Report, unpublished, University of Oklahoma, 51 pp.

_____, and J. T. Lee, 1983: Investigation of the detectability and lifetime of gust fronts and other weather hazards to aircraft. FAA Final Report No. DOT/FAA/PM-83/33, Norman, OK, 58 pp.

APPENDIX A

ACRONYMS AND ABBREVIATIONS

ADIV	Average radial divergence of areal pattern
AFLX	Average radial flux of areal pattern
AREAL	Areal extent of the radial divergence pattern
AREA30	Area enclosed by 30 dBZ contour(s)
AREF	Reflectivity area
AVGD	Average radial divergence of pattern elements
AVGF	Average radial flux of pattern elements
AVGV	Average velocity difference of pattern elements
AVG30	Average reflectivity within 30 dBZ contour(s)
BAZ	Begin azimuth
CAZ	Center azimuth of radial divergence pattern
CRNG	Center range of radial divergence pattern
CST	Central standard time
DELTAR	Range interval between begin and end range
DELTAV	Velocity difference between begin and end range
DIV	Divergence of of the areal pattern
EAZ	End azimuth
ELEV	Elevation angle of radar
HGT	Height of the center of the areal pattern
IOTF	Interim Operational Test Facility
JAWS	Joint Airport Weather Studies
JDOP	Joint Doppler Operational Project
JSP0	Joint System Program Office
MAXD	Maximum radial divergence computed for a PEL
MAXF	Maximum radial flux computed for a PEL
MAXR	Maximum R^2 multiple linear regression technique
MAXRE	Longest PEL
MAXR4	Four-variable MAXR model
MAXV	Maximum velocity difference for all PELs
MET	Meteorological Reasoning
MET3	Three-variable MET model
MSE	Mean square of the error
MWF	Mass weighted flux of areal pattern
NEXRAD	Next Generation Weather Radar
NSSL	National Severe Storms Laboratory
N30	Number of bins with values of 30 dBZ or greater
PEL	Pattern element
PRF	Pulse rate frequency

RADAREA	Divergence element area
RADDIV	Radial divergence
RADFLUX	Radial flux
RB	Begin range
RBAR	Average range
RC	Center of range interval
RE	End range
REF	Reflectivity of each bin
REF30	Reflectivities of 30 dBZ or greater
SAM	Surface automated mesonet
SAS	Statistical Analysis System
TDIV	Total radial divergence of pattern elements
TFLX	Total radial flux of pattern elements
TPEL	Number of PELs in the areal pattern
UTF	Universal tape format
V	Single-Doppler weather radar volume scan
VB	Begin velocity
VE	End velocity
V1	First volume scan of a set of volume scans
VEL	Velocity of each bin
WBAR	Average radar beamwidth

APPENDIX B

BASIC PRINCIPLES OF DOPPLER WEATHER RADAR

Doppler radar measures the net radial component of the velocity (inbound or outbound from the radar) of the scatterers within the sampled volume. Consequently, the observed winds will almost always be less than the true-mean wind speeds. This radial component of velocity results from the measurement of the change in phase over time within the sample volume. The sample volume is defined by the radar beam characteristics and the discrete gate spacing along the radar beam. Because the main lobe is assumed to be of constant dimensions, measurements are considered valid at the center of this "pulse volume." Thus, the average radial velocity v of the scatterers within a pulse volume is describe by

$$f = \frac{2v}{\lambda} , \quad (A.1)$$

where λ = radar wavelength and f = Doppler shift frequency.

For a given pulse repetition frequency (PRF), the maximum Doppler shift frequency detectable is

$$f_{\max} = \frac{\text{PRF}}{2} , \quad (A.2)$$

and the maximum unambiguous Doppler velocity is

$$v_{\max} = \text{PRF} \left(\frac{\lambda}{4} \right) . \quad (\text{A.3})$$

Similarly, the maximum unambiguous range is

$$r_{\max} = \frac{c}{2\text{PRF}} , \quad (\text{A.4})$$

where c = speed of light. The PRF, noted in both equations, results in what is often remarked as the "Doppler dilemma," where

$$v_{\max} r_{\max} = \frac{\lambda c}{8} . \quad (\text{A.5})$$

The average radial velocity is a spatial average over each pulse volume. Variation within pulse volumes cannot be detected. However, variation of the radial velocity within the pulse volume is measured by the spectrum width.

APPENDIX C

NSSL DOPPLER RADAR OPERATIONAL CHARACTERISTICS

The radar data used in this investigation were recorded by NSSL's narrow beamwidth (0.81 deg) Doppler radar, a modified FPS-18 system operating at a 10 cm wavelength. The data were recorded in real-time and are but part of the data recorded during the NEXRAD IOTF Spring 1983 Demonstration. The radar operational parameters for the storm mode are described in Table 14. Note that actual data collection scan rate was approximately 1 rpm with a volume update rate of approximately every 10 minutes.

Table 14. Planned NSSL Doppler radar operational parameters for 1983 Spring NEXRAD IOTF demonstration.

PARAMETER	STORM MODE
Scan Rate	1.67 rpm
Volume Update Rate	6 minutes
Elevation Angles	0.5, 0.5, 1.4, 2.3, 3.4, 4.6, 6.2, 8.4, 11.8, 18.0 degrees
Pulse Rate Time	768 or 1075 μ s
Pulse Length	1 μ s
Number of Pulses Averaged	32
Gain	Normal
Velocity Range Gate Spacing	150 or 210 m
Intensity Range Gate Spacing	600 or 840 m
Velocity Range	115 or 161 km
Intensity Range	460 or 644 km
Unambiguous Velocity	± 34.2 or ± 24.5 m s ⁻¹

APPENDIX D

DIVERGENCE ELEMENT THRESHOLDS

After the completion of each divergence element pattern, candidate divergence elements are tested to see if they should be retained. In a study of supercell storms producing tornadoes and large hail, Zrnic and Gal-Chen (1984) set threshold variables to determine the number of vectors (their term for divergence elements) to be retained. This study use a similar approach, using some and adding others. Threshold variables not applied to this study were: minimum height of storm, range separation, and retention of a minimum number of vectors (divergence elements). This study of non-tornadic storms added three threshold variables: moderate shear, moderate flux, and a minimum acceptable length for a divergence element.

Application of this technique to operational use will be restricted until decision boundaries, or thresholds, have been determined due to geographical and seasonal dependence. Table 15 lists the threshold variables used in this investigation.

Table 15. Horizontal threshold variables.

VARIABLE	THRESHOLD
High Shear	$1.5 \text{ m s}^{-1} \text{ km}^{-1}$
Moderate Shear	$1.0 \text{ m s}^{-1} \text{ km}^{-1}$
Low Shear	$0.6 \text{ m s}^{-1} \text{ km}^{-1}$
High Flux	$30 \text{ m s}^{-1} \text{ km}$
Moderate Flux	$20 \text{ m s}^{-1} \text{ km}$
Low Flux	$10 \text{ m s}^{-1} \text{ km}$
Maximum Azimuthal Separation	1 deg
Minimum Length of Divergence Element	2 km
Reflectivity Suppression Threshold	10 dBZ

APPENDIX E

STORM SUMMIT PREDICTIVE VARIABLES

This Appendix reviews the calculation procedure for storm summit divergence and lists the resulting predictive variables.

Given Doppler radar reflectivity and average radial velocity fields in storage, each "bin" of information is recoverable for select volume scans of the storms under study. The first operations on the fields screen them to suppress undesirable or insignificant data. The mean radial velocity fields were dealiased prior to performing a running average to approximate an effective range resolution of 1 km (to approximate the mid-range azimuthal resolution). After this, the search for divergence elements was accomplished prior to testing as outlined in Appendix D. At this same time, operations were performed on the reflectivity field to tabulate the areal extent of the 30, 40, and 50 dBZ reflectivity distribution and average reflectivity for each storm.

At this point, the following information was known for the reflectivity and divergence elements:

RB	= begin range
RE	= end range
VB	= begin velocity
VE	= end velocity

BAZ = begin azimuth
 EAZ = end azimuth
 ELEV = elevation angle (θ)
 VEL = velocity of each bin
 REF = reflectivity of each bin

Thus, the following calculations could be made for reflectivity and divergence elements (Note that reflectivity elements were fields containing dBZ values; while divergence elements contained radial velocity values):

DELTAR = $RE - RB$ = range interval
 RC = $DELTAR/2$ = center of range interval
 RBAR = $(RB + RE)/2$ = average range
 WBAR = $RBAR * ELEV$ = average beamwidth
 AREF = $WBAR * RBAR$ = reflectivity element area
 RADAREA = $WBAR * RBAR$ = divergence element area

Now, because the reflectivity field requires no additional manipulation, all reflectivity computations can be tabulated:

AREA30 = $\Sigma AREF30$ = area enclosed by 30 dBZ contour
 AREA40 = $\Sigma AREF40$ = area enclosed by 40 dBZ contour
 AREA50 = $\Sigma AREF50$ = area enclosed by 50 dBZ contour
 N30 = number of bins with values of 30 dBZ or greater

N40 = number of bins with values of 40 dBZ or greater
 N50 = number of bins with values of 50 dBZ or greater
 REF30 = reflectivities of 30 dBZ or greater
 REF40 = reflectivities of 40 dBZ or greater
 REF50 = reflectivities of 50 dBZ or greater
 AVG30 = $(\sum \text{REF30})/N30$ = avg reflectivity within 30 dBZ
 AVG40 = $(\sum \text{REF40})/N40$ = avg reflectivity within 40 dBZ
 AVG50 = $(\sum \text{REF50})/N50$ = avg reflectivity within 50 dBZ

And, the following calculation could be performed on the divergence elements:

DELTAV = $VE - VB$ = radial velocity difference
 RADDIV = $\text{DELTAV}/\text{DELTAR}$ = radial divergence
 RADFLUX = $\text{DELTAV} * \text{DELTAR}$ = radial flux

Once the shear and flux tests were performed, only the divergence elements meeting the criteria in Appendix D were saved. These were then renamed divergence pattern elements (PELs), which form the areal pattern of divergence.

After threshold tests, these were the final calculations of predictive variables prior to analysis:

TPEL = number of PELs in the areal pattern
 MAXRE = longest PEL

MAXV	=	maximum velocity difference for a PEL
MAXD	=	maximum radial div computed for a PEL
MAXF	=	maximum radial flux computed for a PEL
AREAL	= Σ RADAREA	= areal extent of div pattern
CAZ	= (BAZ + EAZ)/2	= center azimuth of div pattern
CRNG	= (Σ RC/TPEL)	= center range of div pattern
AVGV	= (Σ DELTAV)/TPEL	= avg velocity difference of PELs
TDIV	= Σ RADDIV	= total radial div of PELs
AVGD	= TDIV/TPEL	= average radial div of PEL
ADIV	= TDIV/AREAL	= average div of areal pattern
TFLX	= Σ RADFLX	= total radial flux of PELs
AVGF	= TFLX/TPEL	= average radial flux of a PEL
AFLX	= TFLX/AREAL	= average flux of areal pattern
MWF	= $TFLX / [\Sigma (DELTAR / MAXRE)^2]$	= flux of areal pattern
HGT	= $CRNG * (\sin ELEV) + (CRNG^2) / [2 * (4/3) * (6731)]$	= beam center areal pattern height
DIV	= $(1/AREAL_1) * ([AREAL_2 - AREAL_1] / [t_2 - t_1])$	= div of areal pattern over time

With the exception of height of the areal pattern (HGT), the values of the storm summit predictive variables in Table 16 represent the change of the storm over a given time interval. While the storm scan and volume scan rates were planned to be 1.67 rpm and 6 minutes respectively, the actual data sampling rate for storm scan was

approximately 1 rpm and for volume update approximately 10 minutes.

Thus, the time interval from one storm summit sample to the next is on the order of every 10 minutes. Consequently, values for the predictive variables in Table 16 (with the exception of HGT) represent a 10 minute change in storm life cycle at or within the time step prior to strong storm outflow near the surface.

Table 16. Storm divergence algorithm predictive variable calculations applied to this study to forecast strong low-level outflow from non-tornadic storms (units for each variable are as described in Table 5).

OBS	DIV	$\Delta AREF$	$\Delta AREF$	$\Delta AFLX$	$\Delta ADIV$	$\Delta AVGF$	HGT	$\Delta AVGD$	$\Delta AVGV$	$\Delta TDIV$	$\Delta TFLX$
1	-6.20	-5.4	-64.4	-0.2	0.10	-8.3	8.7	0.1	-0.5	-32.4	-863
2	-3.50	0.0	-183.0	-0.6	0.03	-12.6	9.6	0.0	-0.6	-5.5	-515
3	-3.52	-50.1	-27.5	-0.2	-0.04	-4.0	9.0	-0.4	-1.2	-32.3	-492
4	-5.70	-15.1	-185.6	-3.0	-0.37	-9.4	11.7	-1.3	-3.1	-95.8	-1120
5	-5.40	-21.6	-102.7	1.5	0.29	2.3	13.3	1.2	1.9	-22.8	-458
6	-3.05	28.4	-30.1	1.1	0.05	6.7	10.4	0.5	3.2	-6.7	-189
7	-13.80	-48.7	-108.1	-2.7	-0.03	-36.5	9.6	-0.6	-4.3	-65.4	-2670
8	-4.73	0.0	23.1	-0.4	-0.02	-3.2	8.9	-0.3	-1.2	-13.6	-453
9	-3.89	0.0	2.5	-2.9	-0.34	-6.3	6.1	-1.3	-3.9	-35.6	-421
10	-2.81	-31.9	40.7	-1.1	0.00	-5.5	10.0	0.1	0.3	-16.6	-1060
11	-5.77	-47.8	-20.2	-1.8	-0.03	-21.3	11.2	-0.3	-2.6	-81.5	-3046
12	-4.46	-16.0	-23.2	-0.3	-0.07	-3.7	5.8	-0.5	-1.4	-13.0	-118
13	-8.70	0.0	-14.5	0.8	-0.06	5.9	4.3	-0.2	0.0	-5.6	-43
14	-2.60	0.0	-6.7	0.7	-0.01	0.5	4.3	0.1	-0.2	2.7	155
15	-0.90	1.8	-112.5	2.8	-0.34	-3.5	7.3	-1.2	-2.0	-32.8	-233
16	-3.01	22.8	15.8	-1.1	-0.22	-5.0	9.0	-1.0	-2.7	-60.5	-487
17	-7.06	0.0	1.0	-0.4	0.08	-11.7	6.9	0.2	-0.8	-2.2	-363
18	-6.16	14.5	-52.8	-2.3	0.09	-8.9	6.7	-0.1	-1.0	-40.5	-869
19	-1.86	0.0	-37.4	-0.7	-0.02	-5.1	6.4	-0.2	-0.9	-4.4	-146
20	-3.71	4.8	-25.6	-1.1	0.05	-8.3	6.7	-0.1	-0.7	-21.2	-287
21	-2.00	-6.8	20.0	-1.1	0.06	-16.0	12.3	0.0	-2.5	-10.9	-728
22	-6.14	0.0	-38.1	-1.0	0.02	-7.3	10.5	0.0	-0.8	-24.7	-549
23	-7.59	0.0	-33.0	0.9	0.34	2.2	12.3	0.9	1.6	-24.7	-281
24	-2.58	-9.8	-21.8	-2.8	-0.22	-6.4	10.0	0.0	-1.0	-9.9	-40

APPENDIX F

STORM DIVERGENCE ALGORITHM

PROGRAM PATTERN

```

C      COMMON/DATA/BIN(300,90,3),ELARY(10),NG(3),AZ(90),ITIME
      COMMON/DATA2/BIN2(300,90,3)
      COMMON/RECORD/AZCNT(10),MNGATE(3),MXGATE(3),NFLD,ELCNT,
      +      BRANGE,ERANGE
      COMMON/PARMS/IVOL,KVOL,SN,FN
      COMMON/UNITS/IUNIT,JUNIT,KUNIT
      DIMENSION R01(3),DR1(3),MPG(3)
      DIMENSION V(300,90),V2(300,90),VDIV(300,90),VPAT(300,90)
      INTEGER VAVG(300,90)
      INTEGER BEGVEC(10,90),ENDVEC(10,90),NUMVEC(90)
      REAL LOAZ,HIAZ,LRNG,HRNG,MWFLUI
      INTEGER BEGDIV(10,90),ENDDIV(10,90),DIVNUM(90)
      INTEGER BEGPAT(10,90),ENDPAT(10,90),BP,EP
      INTEGER BRANGE,ERANGE,ELCNT,AZCNT,LHC,RHC,BTIME,FILTER
      INTEGER ED,BD,PEL,TPEL,ABTPEL,TMPPEL,PATNUM(90)
      REAL MAXDR,MAXVEL,MAXDIV,MAXFLX
      REAL BVEL(10,90),EVEL(10,90),BEGRNG(10,90),ENDRNG(10,90)
      REAL SHEAR(10,90),FLUX(10,90),VELDIF(10,90),RNGDIF(10,90)
      REAL LSHR,MSHR,HSR,LFLX,MFLX,HFLX
      REAL RC(10,90),AREA(10,90)
      INTEGER SUPGAT,DV
      CHARACTER*2 ALOOP(5)
      CHARACTER*3 MON
      CHARACTER*6 SN
      CHARACTER*2 FN
      LOGICAL FLAG,FIRST,DIV,ASECT,CW
      LOGICAL INBOU,OUTBOU

C      ALOOP(1)='VP'
      ALOOP(2)=' '
      ALOOP(3)=' '
      RADTAC=3.14159/180.
      READ(5,20) IVOL
20  FORMAT(I1)
      READ(5,30) FILTER,THRES
30  FORMAT(I1,1X,F5.1)
      READ(5,1010) LRNG
      READ(5,1010) HRNG
1010 FORMAT(1X,F6.2)
      READ(5,1020) LOAZ
      READ(5,1020) HIAZ
1020 FORMAT(1X,F5.2)
      READ(5,1033) MOVE
1033 FORMAT(I2)
      IF(MOVE.EQ.0) THEN
        INBOU=.FALSE.
        OUTBOU=.FALSE.
      ENDIF
      IF(MOVE.EQ.1) INBOU=.TRUE.
      IF(MOVE.EQ.2) OUTBOU=.TRUE.
      KVUL = 0
40  KVUL = KVUL + 1
      JUNIT = KVUL + 30
      KUNIT = KVUL + 40
      REWIND(JUNIT)
      REWIND(KUNIT)
      READ(KUNIT) SN
      READ(KUNIT) FN
      READ(KUNIT) KVOLD
      READ(KUNIT) IVOLD
      READ(KUNIT) ISECTR
      IF(ISECTR.EQ.1) ASECT=.TRUE.
      READ(KUNIT) BRANGE
      READ(KUNIT) ERANGE
      READ(KUNIT) IDAY
      READ(KUNIT) MON
      READ(KUNIT) IYEAR
      READ(KUNIT) NFLD

```



```

DO 60 ILOOP=1,NFLD
  READ(KUNIT) IWJ
  IF(IWJ.EQ. 22085) READ(KUNIT) VN
  READ(KUNIT) IW2
  READ(KUNIT) IW3
  READ(KUNIT) IW4
  IF(ILOOP.EQ.2) THEN
    RL=FLOAT(IW4)
  ENDIF
  READ(KUNIT) IWS
  RO1(ILOOP) = FLOAT(IW2) + FLOAT(IW3)*0.001
  DR1(ILOOP) = FLOAT(IW4)*0.001
  MPG(ILOOP) = IW4
60 CONTINUE
DO 80 ILOOP=1,NFLD
  READ(KUNIT) MNGATE(ILOOP)
  READ(KUNIT) MXGATE(ILOOP)
  NG(ILOOP) = MXGATE(ILOOP)-MNGATE(ILOOP)+1
80 CONTINUE
READ(KUNIT) ELCNT
DO 100 ILOOP=1,ELCNT
  READ(KUNIT) ELARY(ILOOP)
  READ(KUNIT) AZCNT(ILOOP)
100 CONTINUE
DO 800 LLOOP=1,ELCNT
  FLAG = .TRUE.
  IF(ASECT) THEN
    READ(JUNIT) AZ(1),BTIME
    DO 681 JLOOP=1,NFLD
      DO 581 ILOOP=1,NG(JLOOP)
        READ(JUNIT) BIN(ILOOP,1,JLOOP)
581 CONTINUE
681 CONTINUE
    READ(JUNIT) AZ(2),ITIME
    DO 602 JLOOP=1,NFLD
      DO 502 ILOOP=1,NG(JLOOP)
        READ(JUNIT) BIN(ILOOP,2,JLOOP)
502 CONTINUE
602 CONTINUE
    IF(AZ(1).LT.AZ(2)) CW=.TRUE.
    IF(AZ(1).GT.AZ(2)) CW=.FALSE.
    IF(CW) THEN
      DO 705 KLOOP=3,AZCNT(LLOOP)
        READ(JUNIT) AZ(KLOOP),ITIME
        IF(KLOOP.EQ.AZCNT(LLOOP)) ETIME=ITIME
        DO 605 JLOOP=1,NFLD
          NGATES=NG(JLOOP)
          DO 505 ILOOP=1,NGATES
            READ(JUNIT) BIN(ILOOP,KLOOP,JLOOP)
505 CONTINUE
605 CONTINUE
705 CONTINUE
      ELSE
        AZ(AZCNT(LLOOP))=AZ(1)
        AZ(AZCNT(LLOOP)-1)=AZ(2)
        ETIME=BTIME
        DO 707 KLOOP=AZCNT(LLOOP)-2,1,-1
          READ(JUNIT) AZ(KLOOP),ITIME
          IF(KLOOP.EQ.1) BTIME=ITIME
          DO 607 JLOOP=1,NFLD
            NGATES=NG(JLOOP)
            DO 507 ILOOP=1,NGATES
              BIN(ILOOP,AZCNT(LLOOP),JLOOP)=BIN(ILOOP,1,JLOOP)
              BIN(ILOOP,AZCNT(LLOOP)-1,JLOOP)=BIN(ILOOP,2,JLOOP)
              READ(JUNIT) BIN(ILOOP,KLOOP,JLOOP)
507 CONTINUE
607 CONTINUE
707 CONTINUE
        ENDIF
      ELSE

```

```

DO 500 KLOOP=1,AZCNT(LLOOP)
  READ(JUNIT) AZ(KLOOP),ITIME
  IF(AZ(KLOOP).LT.90.) AZ(KLOOP)=AZ(KLOOP)+360.
  IF(FLAG) THEN
    BTIME = ITIME
    FLAG = .FALSE.
  ENDIF
  DO 400 JLOOP=1,NFLD
    NGATES = NG(JLOOP)
    DO 300 ILOOP=1,NGATES
      READ(JUNIT) BIN(ILOOP,KLOOP,JLOOP)
300    CONTINUE
400    CONTINUE
500    CONTINUE
  ENDIF
  DO 555 IAZ=1,AZCNT(LLOOP)
    DO 484 IFLD=1,NFLD
      DO 383 IGT=1,NG(IFLD)
        BIN2(IGT,IAZ,IFLD)=BIN(IGT,IAZ,IFLD)
383    CONTINUE
484    CONTINUE
555    CONTINUE
    IF(FILTER.EQ. 1) THEN
      NGATES=NG(1)
      DO 601 KLOOP = 1,AZCNT(1)
        DO 501 ILOOP = 1,NGATES
          IF(BIN2(ILOOP,KLOOP,1).LT. THRES) THEN
            BIN2(ILOOP,KLOOP,1) = 99999.
            IF(ILOOP.EQ. 1) THEN
              BIN2(ILOOP,KLOOP,2) = 99999.
              BIN2(ILOOP+1,KLOOP,2) = 99999.
              BIN2(ILOOP+2,KLOOP,2) = 99999.
              BIN2(ILOOP,KLOOP,3) = 99999.
              BIN2(ILOOP+1,KLOOP,3) = 99999.
              BIN2(ILOOP+2,KLOOP,3) = 99999.
            ENDIF
            IF(ILOOP.EQ. NGATES) THEN
              BIN2(ILOOP*4-4,KLOOP,2) = 99999.
              BIN2(ILOOP*4-3,KLOOP,2) = 99999.
              BIN2(ILOOP*4-4,KLOOP,3) = 99999.
              BIN2(ILOOP*4-3,KLOOP,3) = 99999.
            ELSE
              DO 1 II=1,4
                BIN2(ILOOP*4-5+II,KLOOP,2) = 99999.
                BIN2(ILOOP*4-5+II,KLOOP,3) = 99999.
1              CONTINUE
            ENDIF
          ENDIF
        CONTINUE
      ENDIF
    CONTINUE
501    CONTINUE
601    CONTINUE
  ENDIF
  NUMAZ=AZCNT(LLOOP)
  N4GATE=NG(2)
  VCRIT=VN
  DO 444 IGT=1,NG(2)
    DO 443 IAZ=1,NUMAZ
      V(IGT,IAZ)=BIN2(IGT,IAZ,2)
      V2(IGT,IAZ)=V(IGT,IAZ)
443    CONTINUE
444    CONTINUE
    TMPPEL=0
    TMPARE=0.
    TOTREF=0.0
    TOTGAT=0.0
    AREA20=0.0
    AREA30=0.0
    AREA40=0.0
    AREA50=0.0
    DO 487 M=20,50,10
      DO 486 IAZ=1,AZCNT(LLOOP)

```

```

      IGT=0
485  IGT=IGT+1
      IF (IGT.GT.NG(1)) GO TO 486
      IF (BIN2(IGT,IAZ,1).GT.900.) GO TO 485
      IF (BIN2(IGT,IAZ,1).LT.M) GO TO 485
      K=0
      JBEG=IGT
494  K=K+1
      REF=BIN2(IGT+K,IAZ,1)
      IF ((REF.LT.900.) .AND. (REF.GE.M)) THEN
        GO TO 494
      ELSE
        JEND=IGT+K-1
        RBEG=(MNGATE(1)+JBEG-2)*DR1(1) + R01(1)
        REND=(MNGATE(1)+JEND-2)*DR1(1) + R01(1)
        RSPACE=DR1(1)
        CALL AREALR(RBEG,REND,RSPACE,RAREA)
        IF (M.EQ.20) AREA20=AREA20+RAREA
        IF (M.EQ.30) AREA30=AREA30+RAREA
        IF (M.EQ.40) AREA40=AREA40+RAREA
        IF (M.EQ.50) AREA50=AREA50+RAREA
        IGT=JEND
        GO TO 485
      ENDIF
486  CONTINUE
487  CONTINUE
      AVGR20=0.0
      AVGR30=0.0
      AVGR40=0.0
      AVGR50=0.0
      RGAT20=0.0
      RGAT30=0.0
      RGAT40=0.0
      RGAT50=0.0
      TOTR20=0.0
      TOTR30=0.0
      TOTR40=0.0
      TOTR50=0.0
      DO 573 IAZ=1,AZCNT(LLOOP)
      DO 572 IGT=1,NG(1)
        IF (BIN2(IGT,IAZ,1).LT.900.) THEN
          IF (BIN2(IGT,IAZ,1).GE.20.) THEN
            RGAT20=RGAT20+1.
            TOTR20=TOTR20+BIN2(IGT,IAZ,1)
          ENDIF
          IF (BIN2(IGT,IAZ,1).GE.30.) THEN
            RGAT30=RGAT30+1.
            TOTR30=TOTR30+BIN2(IGT,IAZ,1)
          ENDIF
          IF (BIN2(IGT,IAZ,1).GE.40.) THEN
            RGAT40=RGAT40+1.
            TOTR40=TOTR40+BIN2(IGT,IAZ,1)
          ENDIF
          IF (BIN2(IGT,IAZ,1).GE.50.) THEN
            RGAT50=RGAT50+1.
            TOTR50=TOTR50+BIN2(IGT,IAZ,1)
          ENDIF
        ENDIF
572  CONTINUE
573  CONTINUE
      IF (RGAT20.EQ.0.) RGAT20=1.
      IF (RGAT30.EQ.0.) RGAT30=1.
      IF (RGAT40.EQ.0.) RGAT40=1.
      IF (RGAT50.EQ.0.) RGAT50=1.
      AVGR20=TOTR20/RGAT20
      AVGR30=TOTR30/RGAT30
      AVGR40=TOTR40/RGAT40
      AVGR50=TOTR50/RGAT50
      INBOU=.TRUE.
      OUTBOU=.FALSE.

```

```

DO 232 IAZ=1,AZCNT(LLOOP)
VLAST=V(1,IAZ)
SUPGAT=0
DO 231 IGT=2,N4GATE
IF((V(IGT,IAZ).GT.900.).AND.(V(IGT-1,IAZ).GT.900)) THEN
    SUPGAT=SUPGAT+1
    GO TO 231
ENDIF
IF((V(IGT,IAZ).GT.900.).AND.(V(IGT-1,IAZ).LT.900)) THEN
    VLAST=V(IGT-1,IAZ)
    SUPGAT=SUPGAT+1
    GO TO 231
ENDIF
IF((V(IGT,IAZ).LT.900.).AND.(V(IGT-1,IAZ).LT.900.)) THEN
    SUPGAT=0
    IF(IGT-1.EQ.1) THEN
        IF(INBOU) THEN
            IF((V(IGT-1,IAZ).GT.0.).AND.
+           (V(IGT-1,IAZ).GT.0.25*VCRIT)) THEN
                V2(IGT-1,IAZ)=V(IGT-1,IAZ)-2.*VCRIT
                VLAST=V2(IGT-1,IAZ)
                V(IGT-1,IAZ)=VLAST
                GO TO 231
            ENDIF
        ENDIF
        IF(OUTBOU) THEN
            IF((V(IGT-1,IAZ).LT.0.)
+           .AND.(ABS(V(IGT-1,IAZ)).GT.0.25*VCRIT)) THEN
                V2(IGT-1,IAZ)=2.*VCRIT-V(IGT-1,IAZ)
                VLAST=V2(IGT-1,IAZ)
                V(IGT-1,IAZ)=VLAST
                GO TO 231
            ENDIF
        ENDIF
        ENDIF
        VLAST= V(IGT-1,IAZ)
        GO TO 111
    ENDIF
    IF((V(IGT,IAZ).LT.900.).AND.(V(IGT-1,IAZ).GT.900.))
+    .AND.(VLAST.LT.900.)) THEN
        IF(SUPGAT.LT.17) THEN
            IF(INBOU) THEN
                IF((V(IGT-1,IAZ).GT.0.).AND.
+                (V(IGT-1,IAZ).GT.0.25*VCRIT)) THEN
                    V2(IGT-1,IAZ)=V(IGT-1,IAZ)-2.*VCRIT
                    VLAST=V2(IGT-1,IAZ)
                    V(IGT-1,IAZ)=VLAST
                    GO TO 231
                ENDIF
            ENDIF
            GO TO 231
        ENDIF
        IF(OUTBOU) THEN
            IF((V(IGT-1,IAZ).LT.0.)
+            .AND.(ABS(V(IGT-1,IAZ)).GT.0.25*VCRIT)) THEN
                V2(IGT-1,IAZ)=2.*VCRIT-V(IGT-1,IAZ)
                VLAST=V2(IGT-1,IAZ)
                V(IGT-1,IAZ)=VLAST
                GO TO 231
            ENDIF
        ENDIF
        GO TO 111
    ELSE
        SUPGAT=0
        GO TO 231
    ENDIF
ELSE
    IF(VLAST.GT.900.) VLAST=V(IGT,IAZ)
    IF(INBOU) THEN

```

```

      IF((V(IGT,IAZ).GT.0.).AND.
+      (V(IGT,IAZ).GT.0.25*VCRIT)) THEN
        V2(IGT,IAZ)=V(IGT,IAZ)-2.*VCRIT
        VLAST=V2(IGT,IAZ)
        V(IGT,IAZ)=VLAST
        GO TO 231
      ENDIF
      GO TO 231
    ENDIF
    IF(OUTBOU) THEN
      IF((V(IGT,IAZ).LT.0.)
+      .AND.(ABS(V(IGT,IAZ)).GT.0.25*VCRIT)) THEN
        V2(IGT,IAZ)=2.*VCRIT-V(IGT,IAZ)
        VLAST=V2(IGT,IAZ)
        V(IGT,IAZ)=VLAST
        GO TO 231
      ENDIF
      GO TO 231
    ENDIF
    GO TO 231
  ENDIF
111 IF((V(IGT,IAZ).LT.0.).AND.(V(IGT-1,IAZ).LT.0.)) GO TO 231
    IF((V(IGT,IAZ).GT.0.).AND.(V(IGT-1,IAZ).GT.0.)) GO TO 231
    IF(ABS(V(IGT,IAZ)-VLAST).GT.VCRIT+6.) THEN
      V2(IGT,IAZ)=V(IGT,IAZ)+ 2.*VCRIT
      IF(V2(IGT,IAZ).GT.2.*VCRIT) V2(IGT,IAZ)=V(IGT,IAZ)-2.*VCRIT
      VLAST=V2(IGT,IAZ)
      V(IGT,IAZ)=VLAST
    ELSE
      IF((V2(IGT-1,IAZ).GT.VCRIT-4.)) THEN
        K=-3
66      K=K+1
        IF((ABS(V2(IGT+K,IAZ-1)).GT.VCRIT).AND.
+        (V2(IGT+K,IAZ-1).LT.900.)) THEN
          V2(IGT,IAZ)=V(IGT,IAZ)+ 2.*VCRIT
          IF(V2(IGT,IAZ).GT.2.*VCRIT) V2(IGT,IAZ)=V(IGT,IAZ)-2.*VCRIT
          VLAST=V2(IGT,IAZ)
          V(IGT,IAZ)=VLAST
          VLAST=V(IGT,IAZ)
          GO TO 231
        ENDIF
        IF(K.EQ.2) THEN
          GO TO 231
        ELSE
          GO TO 66
        ENDIF
      ENDIF
    ENDIF
231 CONTINUE
232 CONTINUE
    DO 51 IGT=2,NG(2)
      DO 49 IAZ=1,AZCNT(LLOOP)
        V(IGT,IAZ)=V2(IGT,IAZ)
49      CONTINUE
51      CONTINUE
        DO 243 IAZ=1,AZCNT(LLOOP)
          NUMVEC(IAZ)=0
          J=0
          FIRST=.TRUE.
          DO 101 IGT=1,NG(2)-1
            IF((IGT.EQ.NG(2)-1).AND.(V(IGT+1,IAZ).LT.900.)) THEN
              IEND=IGT+1
              GO TO 103
            ENDIF
            IF((V(IGT,IAZ).GT.900.).AND.(V(IGT+1,IAZ).GT.900.)) THEN
              VAVG(IGT,IAZ)=66666
              VAVG(IGT+1,IAZ)=66666
              FIRST=.FALSE.
              GO TO 101
            ENDIF

```

```

IF((V(IGT,IAZ).GT.900.).AND.(V(IGT+1,IAZ).LT.900.)) THEN
  FIRST= .TRUE.
  VAVG(IGT,IAZ)=66666
  IBEG=IGT+1
  GO TO 101
ENDIF
IF((V(IGT,IAZ).LT.900.).AND.(V(IGT+1,IAZ).LT.900.)) THEN
  IF(FIRST) THEN
    IBEG=IGT
    FIRST=.FALSE.
  ENDIF
  GO TO 101
ENDIF
IF((V(IGT,IAZ).LT.900.).AND.(V(IGT+1,IAZ).GT.900.)) THEN
  IEND=IGT
  VAVG(IGT+1,IAZ)=66666
  GO TO 103
ENDIF
103 IDIF=IEND-IBEG + 1
IF(IDIF.GE.9) THEN
  J=J+1
  NUMVEC(IAZ)= J
  CALL AVG(IBEG,IEND,IAZ,V,VN,NUMNYQ,VAVG)
  BEGVEC(J,IAZ)=IBEG
  ENDVEC(J,IAZ)=IEND
  GO TO 101
ELSE
  DO 575 ISUP=IBEG,IEND
    VAVG(ISUP,IAZ)=66666
575 CONTINUE
  GO TO 101
ENDIF
101 CONTINUE
243 CONTINUE
  LSHR = 0.5
  MSHR = 0.85
  HSHR = 1.5
  LFLX = 10
  MFLX = 18
  HFLX = 30
  DO 182 IAZ=1,AZCNT(LLOOP)
    DO 181 IGT=1,NG(2)
      VDIV(IGT,IAZ)=6666.
181 CONTINUE
182 CONTINUE
    DO 94 IAZ=1,AZCNT(LLOOP)
      DIVNUM(IAZ)=0
      PE=NUMVEC(IAZ)
      IF(PE.EQ.0) GO TO 94
      L=1
      DO 93 INUM=1,PE
        IBEG=BEGVEC(INUM,IAZ)
        IEND=ENDVEC(INUM,IAZ)
        IGATE=IBEG
11      MINMAX=VAVG(IBEG,IAZ)
        DIV=.FALSE.
22      K=0
        IF(.NOT.DIV) THEN
          BEGDIV(L,IAZ)=IGATE
        ENDIF
33      K=K+1
        IF(VAVG(IGATE+K,IAZ).GE.MINMAX) GO TO 44
        DIV=.FALSE.
        IF((K.LT.NUMNYQ).AND.(IGATE+K.NE.IEND)) GO TO 33
        GO TO 55
44      MINMAX=VAVG(IGATE+K,IAZ)
        IF(IGATE+K.EQ.IEND) THEN
          ENDDIV(L,IAZ)= IGATE + K
          TEST=ENDDIV(L,IAZ)-BEGDIV(L,IAZ)
          IF(TEST.LT.9.) GO TO 93

```

```

        DIVNUM(IAZ)=L
        L=L+1
        GO TO 93
    ENDIF
    IGATE=IGATE+K
    DIV=.TRUE.
    GO TO 22
55 IF(IGATE+K.EQ.IEND) THEN
    ENDDIV(L,IAZ)=IGATE
    TEST=ENDDIV(L,IAZ)-BEGDIV(L,IAZ)
    IF(TEST.LT.9) GO TO 93
    DIVNUM(IAZ)=L
    L=L+1
    GO TO 93
ELSE
    ENDDIV(L,IAZ)=IGATE
    IGATE=IGATE+1
    MINMAX=VAVG(IGATE,IAZ)
    DIV=.FALSE.
    TEST=ENDDIV(L,IAZ)-BEGDIV(L,IAZ)
    IF(TEST.LT.9) GO TO 22
    DIVNUM(IAZ)=L
    L=L+1
    GO TO 22
ENDIF
93 CONTINUE
94 CONTINUE
    DO 124 IAZ=1,AZCNT(LLOOP)
    DV=DIVNUM(IAZ)
    IF(DV.EQ.0) GO TO 124
    DO 123 IDIV=1,DV
    IPEG=BEGDIV(IDIV,IAZ)
    IEND=ENDDIV(IDIV,IAZ)
    DO 122 IGT=IBEG,IEND
    VDIV(IGT,IAZ)= VAVG(IGT,IAZ)
122 CONTINUE
123 CONTINUE
124 CONTINUE
    DO 413 IAZ=1,AZCNT(LLOOP)
    DO 412 IGT=1,NG(2)
    VPAT(IGT,IAZ)=9999.
412 CONTINUE
413 CONTINUE
    DO 377 IAZ=1,AZCNT(LLOOP)
    PATNUM(IAZ)=0
    DV=DIVNUM(IAZ)
    J=1
    IF(DV.EQ.0) GO TO 377
    DO 376 L=1,DV
    BD=BEGDIV(L,IAZ)
    ED=ENDDIV(L,IAZ)
    RBEG=(MNGATE(2)+BD-1)*DR1(2) + R01(2)
    REND=(MNGATE(2)+ED-1)*DR1(2) + R01(2)
    VBEG=VAVG(BD,IAZ)
    VEND=VAVG(ED,IAZ)
    IF((VBEG.GT.900.) .OR. (VEND.GT.900.)) GO TO 376
    DELV=ABS(VEND-VBEG)
    DELR= REND-RBEG
    SHR= DELV/DELR
    FLX=DELV*DELR
    IF( ((SHR.GT.LSHR) .AND. (FLX.GT.HFLX)) .OR.
      - ((SHR.GT.MSHR) .AND. (FLX.GT.MFLX)) .OR.
      + ((SHR.GT.HSHR) .AND. (FLX.GT.LFLX)) ) THEN
    IF((RBEG.GE.LRNG) .AND. (RBEG.LT.HRNG)
      + .AND. (IAZ).GE.LOAZ) .AND. (IAZ).LT.HIAZ)) THEN
    IF(DELV.GT.1.4*VN) THEN
    TEMPCR=(RBEG+REND)/2.
    TMPARE= TMPARE+ RADFAC*TEMPCR*DELR
    TMPPEL=TMPPEL+1
    ELSE

```

```

      BVEL(J,IAZ)=VBEG
      BEGPAT(J,IAZ)=BD
      ENDPAT(J,IAZ)=ED
      PATNUM(IAZ)=J
      EVEL(J,IAZ)=VEND
      BEGRNG(J,IAZ)=RBEG
      ENDRNG(J,IAZ)=REND
      SHEAR(J,IAZ)=SHR
      FLUX(J,IAZ)=FLX
      VELDIF(J,IAZ)=DELV
      RNGDIF(J,IAZ)=DELR
      RC(J,IAZ)= (REND+RBEG)/2.
      AREA(J,IAZ)= (3.14159/180.)*RC(J,IAZ)*DELR
      J=J+1
    ENDIF
  ENDIF
ENDIF
376 CONTINUE
377 CONTINUE
    DO 546 IAZ=1,AZCNT(LLOOP)
      IF(PATNUM(IAZ).EQ.0) GO TO 546
      DO 545 IPAT=1,PATNUM(IAZ)
        BP=BEGPAT(IPAT,IAZ)
        EP=ENDPAT(IPAT,IAZ)
        DO 543 IGT=BP,EP
          VPAT(IGT,IAZ)= VDIV(IGT,IAZ)
        543 CONTINUE
      545 CONTINUE
    546 CONTINUE
      WRITE(6,301)
301  FORMAT('1'//,T35,' PATTERN ELEMENTS ',//)
      WRITE(6,302)
302  FORMAT(' ',T2,' AZ ',T11,' BR ',T20,' ER ',T31,' DR',T38,' BV',
+         T44,' EV ',T52,' DV',T57,' SHR',T66,' FLUX',T74,' RC ',
+         T85,' AREA',T93,' EL',//)
      DO 283 IAZ=1,AZCNT(LLOOP)
        PEL=PATNUM(IAZ)
        IF(PEL.EQ.0) GO TO 283
        DO 282 IPEL=1,PEL
          DELR=ENDRNG(IPEL,IAZ)-BEGRNG(IPEL,IAZ)
          DVEL=EVEL(IPEL,IAZ)-BVEL(IPEL,IAZ)
          WRITE(6,303) AZ(IAZ),BEGRNG(IPEL,IAZ),ENDRNG(IPEL,IAZ),
+          DELR, BVEL(IPEL,IAZ),EVEL(IPEL,IAZ),DVEL,SHEAR(IPEL,IAZ),
+          FLUX(IPEL,IAZ),RC(IPEL,IAZ),AREA(IPEL,IAZ),ELARY(LLOOP)
303  FORMAT(' ',F5.1,3X,F6.2,3X,F6.2,3X,F6.2,3X,F4.0,3X,F4.0,
+          3X,F4.0,3X,F4.2,3X,F5.1,3X,F6.2,3X,F7.2,3X,F4.1)
        282 CONTINUE
      283 CONTINUE
        TPEL=0
        TOTSHR=0
        TOTFLX=0
        TDVEL=0
        TOTRC=0
        TAREA=0
        MAXDR=0
        MAXVEL=0
        MAXDIV=0
        MAXFLX=0
        DRSQR=0
        K=0
        DO 344 IAZ=1,AZCNT(LLOOP)
          PEL=PATNUM(IAZ)
          IF(PEL.EQ.0) GO TO 344
          K=K+1
          TPEL=TPEL+PEL
          IF(K.EQ.1) BAZ=AZ(IAZ)
          EAZ=AZ(IAZ)
          DO 343 J=1,PEL
            TOTSHR=TOTSHR+SHEAR(J,IAZ)
            TOTFLX=TOTFLX+FLUX(J,IAZ)
          343 CONTINUE
        344 CONTINUE
      ENDIF
    ENDIF
  ENDIF

```



```

TDVEL=TDVEL+VELDIF(J,IAZ)
TOTRC=TOTRC+RC(J,IAZ)
TAREA=TAREA+AREA(J,IAZ)
DRSQR=DRSQR+RNGDIF(J,IAZ)**2
IF(MAXDR.LT.RNGDIF(J,IAZ)) MAXDR=RNGDIF(J,IAZ)
IF(MAXVEL.LT.VELDIF(J,IAZ)) MAXVEL=VELDIF(J,IAZ)
IF(MAXDIV.LT.SHEAR(J,IAZ)) MAXDIV=SHEAR(J,IAZ)
IF(MAXFLX.LT.FLUX(J,IAZ)) MAXFLX=FLUX(J,IAZ)
343 CONTINUE
344 CONTINUE
IF(TPEL.EQ.0) GO TO 3
AVGVEL=TDVEL/TPEL
AVGSHR=TOTSHR/TPEL
AVGFLX=TOTFLX/TPEL
CAZ=(BAZ+EAZ)/2.
1045 CRNG=TOTRC/TPEL
THETA=ELARY(LLOOP)*RADFAC
AE=(4./3.)*6731.
HGT=CRNG*(SIN(THETA)) + (CRNG**2)/(2.*1E)
AREFLX= TOTFLX/TAREA
AREDIV= TOTSHR/TAREA
AVGDIV=TOTSHR/TPEL
AVGFLX=TOTFLX/TPEL
MWFLUX=TOTFLX/DRSQR/(MAXDR**2)
ABTPEL=TPEL+TMPPEL
ABAREA=TAREA+TMPARE
3 WRITE(6,305)
305 FORMAT(////,' ',T20,'AREAL PATTERN',/)
WRITE(6,307) MAXVEL
307 FORMAT(' ',17X,'MAXVEL = ',F6.1)
WRITE(6,308) AVGVEL
308 FORMAT(' ',17X,'AVGVEL = ',F6.1)
WRITE(6,333) MAXDR
333 FORMAT(' ',17X,'MAXRNG = ',F7.2,/)
WRITE(6,310) MAXDIV
310 FORMAT(' ',13X,'MAX RADDIV = ',F6.1)
WRITE(6,320) AVGDIV
320 FORMAT(' ',13X,'AVG RADDIV = ',F7.2)
WRITE(6,318) AREDIV
318 FORMAT(' ',11X,'AREAL RADDIV = ',F7.2)
WRITE(6,1314) TOTSHR
1314 FORMAT(' ',11X,'TOTAL RADDIV = ',F7.2,/)
WRITE(6,312) MAXFLX
312 FORMAT(' ',15X,'MAX FLUX = ',F6.1)
WRITE(6,319) AVGFLX
319 FORMAT(' ',15X,'AVG FLUX = ',F6.1)
WRITE(6,317) AREFLX
317 FORMAT(' ',13X,'AREAL FLUX = ',F7.2)
WRITE(6,1313) TOTFLX
1313 FORMAT(' ',13X,'TOTAL FLUX = ',F7.1)
WRITE(6,309) MWFLUX
309 FORMAT(' ',10X,'MASS WTD FLUX = ',F6.1,/)
WRITE(6,313) CAZ
313 FORMAT(' ',20X,'CAZ = ',F6.1)
WRITE(6,314) CRNG
314 FORMAT(' ',19X,'CRNG = ',F7.2,/)
WRITE(6,315) HGT
315 FORMAT(' ',15X,' HEIGHT = ',F7.2)
WRITE(6,316) TAREA,ABAREA
316 FORMAT(' ',16X,' AREA = ',F7.2,2X,'(',F7.2,')',/)
WRITE(6,321) TPEL,ABTPEL
321 FORMAT(/,' ', '***** TOTAL PATTERN ELEMENTS THIS EL = ',
+ I4,2X,'(',I4,')')
WRITE(6,322) AREA20,AVGR20
WRITE(6,323) AREA30,AVGR30
WRITE(6,324) AREA40,AVGR40
WRITE(6,325) AREA50,AVGR50
322 FORMAT(//,' ', '20dBZ AREAL REFLECTIVITY = ',F6.1,8X,
+ 'AVGR20 = ',F4.1,' dBZ')
323 FORMAT(/,' ', '30dBZ AREAL REFLECTIVITY = ',F6.1,8X,

```

```

+ 'AVGR30 = ',F4.1,' dBZ')
324 FORMAT(/, ' ', '40dBZ AREAL REFLECTIVITY = ',F6.1,8X,
+ 'AVGR40 = ',F4.1,' dBZ')
325 FORMAT(/, ' ', '50dBZ AREAL REFLECTIVITY = ',F6.1,8X,
+ 'AVGR50 = ',F4.1,' dBZ')
WRITE(6,338)
338 FORMAT(/, ' ', 'T5, WINDOW COORDINATES ARE .....')
WRITE(6,337) LOAZ,HIAZ,LRNG,HRNG
337 FORMAT(' ',T10,'LOAZ= ',F5.1,3X,'HIAZ= ',F5.1,
+ 3X,'LRNG= ',F6.2,3X,'HRNG= ',F6.2)
GO TO 800
24 DO 700 K=1,1
LHC = 1
IPG = 1
IF(AZCNT(LLOOP) .GT. 30) THEN
RHC = 30
ELSE
RHC = AZCNT(LLOOP)
ENDIF
550 WRITE(6,560) ELARY(LLOOP),ALOP(K),AZ(LHC),AZ(RHC),
+BTIME,IDAY,MON,IYEAR,SN,FN,IPG
560 FORMAT('1','EL ANGLE = ',F4.1,2X,'FIELD = ',A2,2X,
+ 'AZM ',F6.1,' TO ',F6.1,2X,'BTIME = ',I6,
+ 2X,'DATE: ',I2,1X,A3,' 19',I2,3X,'TAPE SN: ',A6,
+ 2X,'FILE: ',A2,3X,'PAGE ',I2)
DO 600 I = NG(2),1,-1
RNG = (MNGATE(2)+I-1) * DR1(2) + R01(2)
IF(K.EQ.1) THEN
WRITE(6,570) (RNG,(VPAT(I,J),J=LHC,RHC))
ENDIF
570 FORMAT(' ',F6.2,5X,30F4.0)
580 FORMAT(' ',F6.2,5X,30(I3,1X))
600 CONTINUE
IF(RHC .NE. AZCNT(LLOOP)) THEN
RHC = RHC + 30
LHC = LHC + 30
IPG = IPG + 1
IF(RHC .GE. AZCNT(LLOOP)) RHC = AZCNT(LLOOP)
GO TO 550
ENDIF
700 CONTINUE
800 CONTINUE
IF(KVOL .NE. IVOL) GO TO 40
STOP
END
SUBROUTINE AVG(IBEG,IEND,IAZ,V,VN,NUMNYQ,VAVG)
DIMENSION V(300,90)
INTEGER VAVG(300,90)
INTEGER IBEG,IEND
IF((VN.GT.24.) .AND. (VN.LT.27)) NUMNYQ=5
IF((VN.GT.27.) .AND. (VN.LT.32)) NUMNYQ=6
IF(VN.GT.32.) NUMNYQ=7
VAVG(IBEG,IAZ)=(V(IBEG,IAZ)+V(IBEG+1,IAZ)+V(IBEG+2,IAZ))/3.
VAVG(IBEG+1,IAZ)=(V(IBEG,IAZ)+V(IBEG+1,IAZ)+V(IBEG+2,IAZ)
+ V(IBEG+3,IAZ))/4.
DO 200 IGT= IBEG+2,IEND-2
VAVG(IGT,IAZ)=(V(IGT-2,IAZ)+V(IGT-1,IAZ) + V(IGT,IAZ)
+ V(IGT+1,IAZ) + V(IGT+2,IAZ) ) /NUMNYQ
200 CONTINUE
VAVG(IEND-1,IAZ)= (V(IEND-3,IAZ)+V(IEND-2,IAZ)+V(IEND-1,IAZ)
+ V(IEND,IAZ))/4.
VAVG(IEND,IAZ)= (V(IEND-2,IAZ) + V(IEND-1,IAZ)
+ V(IEND,IAZ))/3.
RETURN
END
SUBROUTINE AREALR(RBEG,REND,RSPACE,RAREA)
RADFAC=3.14159/180.
IF(RBEG.EQ.REND) THEN
RAREA=RBEG*RADFAC*RSPACE
RETURN

```

```

ENDIF
CG = (RBEG+REND)/2.
DR = (REND-RBEG+RSPACE)
RAREA= CG*RA DFAC*DR
RETURN
END

```

```

1      *** NO. OF VOLUMES TO EVALUATE (I1)      ***
1  10.0 *** FILTER (YES:1 NO:0), THRESHOLD VALUE (I1,1X,F5.1) ***
      00.00 *** LRNG(1X,F6.2) Default=0.00      ***
999.99 *** HRNG(1X,F6.2) Default=999.99      ***
000.0  *** LOAZ(1X,F5.2) Default=0.00      ***
999.9  *** HIAZ(1X,F5.2) Default=999.9      ***
0      *** TRANSVERSE=0, INBOUND=1, OUTBOUND=2 ***

```

APPENDIX G

ERROR IN DIVERGENCE AND FLUX ESTIMATES

Studies have shown that several sources of error in Doppler divergence fields are due to limitations of single-Doppler velocity measurements (Snapp, 1979; Witt, 1984). These are due primarily to viewing and elevation angle dependence. One major source of error is the viewing angle when determining the effect of asymmetry of a storm to calculate areal divergence patterns. Witt (1984) showed that large underestimates of divergence and flux may occur for highly elliptical divergence patterns. For example, Eyster (1985) noted that if a Doppler radar samples along the major axis of a particular storm outflow, the maximum divergence and flux detectable in the storm outflow would be approximately $2 \times 10^{-3} \text{ s}^{-1}$ and $800 \text{ m s}^{-1} \text{ km}$ respectively. If sampling were along the minor axis of storm outflow, the maximum divergence and flux detectable would be approximately $5 \times 10^{-3} \text{ s}^{-1}$ and $1125 \text{ m s}^{-1} \text{ km}$ respectively. Consequently, the position of the radar with respect to the storm outflow may result in large under or overestimates of divergence and flux of an areal divergence pattern.

Another major source of error is the elevation angle at which a storm is sampled. Snapp (1979) showed that continued sampling of a storm top approaching the radar, which necessitates increasing the elevation angle, degrades the quality of the measurements due to the

differences in height of the beginning and ending radial velocities of a data sample. Consequently, application of the divergence algorithm to a storm summit near the radar should be approached cautiously.

Of note, in this investigation, all storms except one were beyond 50 km (one was at 32 km). The storms were selected carefully to minimize the introduction of these potential sources of error due to viewing and elevation angles.

VITA

Gary Leon Sickler [REDACTED]

After graduating from West Canada Valley High School in Middleville, New York in June 1963, he enlisted in the United States Air Force. In February 1964, he completed the Air Weather Service Observer School and served as a weather observer through 1971. During 1969, while in Okinawa, he began college coursework, attending the University of Maryland, Far East Division. During the summer of 1971, while serving as Chief Weather Observer at Hancock Field, Syracuse, New York, he was selected for the Airman Education and Commissioning Program by the Air Force Institute of Technology (AFIT). In May 1974, he received a Bachelor of Science degree in Meteorology from Texas A&M University and then attended Officer's Training School. He was commissioned on 16 August 1974. He was then assigned as Wing Weather Officer at McConnell Air Force Base (AFB), Wichita, Kansas. Returning to Texas A&M University in August 1977, via the AFIT, he earned a Masters of Science in Meteorology degree in May 1979. Following this he was assigned to the Scientific Services Division, Headquarters Fifth Weather Wing, Langley AFB, Virginia. During this period, he also served as a member of the Rapid Deployment Joint Task Force. The author entered Texas A&M University in August 1982, to pursue the degree of Doctor of Philosophy under AFIT sponsorship. [REDACTED]

[REDACTED]